
**Search for high energy neutrinos
from our Galaxy
with IceCube**

Yolanda Sestayo de la Cerra
Max-Planck-Institut für Kernphysik

Heidelberg 2010

Dissertation in Physics
submitted to the
Combined Faculties for the Natural Sciences and for Mathematics
of the Ruperto-Carola University of Heidelberg, Germany.
for the degree of
Doctor of Natural Sciences

presented by
Dipl.-Physik. *Yolanda Sestayo de la Cerra*
born in Gijón, Spain
Oral examination: 26.05.2010

**Search for high energy neutrinos
from our Galaxy
with IceCube**

**Referees: Prof. Dr. Konrad Bernlöhr
Prof. Dr. Wolfgang Krätschmer**

Abstract

High energy neutrino telescopes are expected to play a major role in the discovery of the first unambiguous sources of cosmic-rays. With completion in 2011, the IceCube neutrino detector constitutes the most sensitive instrument to sources of high energy neutrinos. Its performance and discovery potential are usually given in the energy range above a few TeV, in order to achieve the best signal to noise for sources following an E^{-2} spectrum without an energy cutoff up to at least 1 PeV. However, given the present understanding and multiwavelength picture of our galaxy, we can expect that galactic sources of high energy neutrinos show significant deviations from the E^{-2} , no cutoff approximation. The common data analysis are therefore not optimal for such galactic scenarios, requiring exposure times of the order of several years, even a decade, to reach a level of sensitivity at which a possible detection starts to be plausible. The main goal of this thesis is to improve the discovery potential of IceCube to galactic sources of high energy neutrinos, aiming to a better understanding of the high energy processes taking place in our galaxy. In order to fulfill this goal, I follow two lines of action: (1) to increase the detection capabilities of IceCube for neutrinos in the energy range between $100 \text{ GeV} < E < 1 \text{ TeV}$; and (2) to develop a search method which is able to reduce the minimum detectable flux per point source. The improvement of the IceCube performance at energies below 1 TeV is achieved with the use of the combined detector configuration IceCube 22 strings plus AMANDA (Antarctic Muon And Neutrino Detector Array). The data processing scheme is designed in order to keep as many good low energy events as possible. As a result, this analysis achieved the best sensitivity for sources with neutrino spectra steeper than E^{-2} and/or an energy cutoff below 1 PeV. The second goal of this thesis is motivated in order to search efficiently for high energy neutrinos from the Cygnus star forming region of the Galaxy. In order to extend the search beyond a single point source, I developed a method based on two-point analysis to detect, within an extended region, event patterns which might go undetected in conventional point source analysis. The results obtained with this method indicate that the minimum detectable flux per point source is reduced by $\sim 26\%$ - 59% with respect to standard point source analysis, provided there is more than one point source within the region under study. This method was applied on the Cygnus region of the Galaxy using the data sample obtained with the combined detector IceCube 22 strings plus AMANDA, yielding a significance of 2.3σ .

Zusammenfassung

Von Hochenergie-Neutrinooteleskopen wird erwartet, dass sie eine entscheidende Rolle bei der Entdeckung der ersten eindeutigen Quellen kosmischer Strahlung spielen werden. Nach der Fertigstellung 2011 wird der IceCube Neutrino-detektor das sensitivste Instrument für Quellen hochenergetischer Neutrinos sein. Die Leistung und das Entdeckungspotential (*discovery potential*) des Detektors werden üblicherweise im Energiebereich oberhalb einiger TeV untersucht, um das beste Signal-zu-Rausch-Verhältnis für Quellen mit einem E^{-2} Spektrum ohne Cutoff unterhalb 1 PeV oder mehr zu erzielen. Das derzeitige Verständnis der Galaxis und das Bild, das sich unter Einbeziehung verschiedener Wellenlängenbereiche ergibt, legen jedoch signifikante Abweichungen von der Annahme eines E^{-2} Spektrums ohne Cutoff nahe. Herkömmliche Datenanalysen sind also für solche galaktische Szenarien nicht optimal und erfordern Detektorlaufzeiten von mehreren Jahren, wenn nicht sogar einem Jahrzehnt, um eine Sensitivität zu erreichen, bei der eine mögliche Entdeckung in greifbare Nähe rückt. Das Hauptanliegen dieser Arbeit besteht in der Verbesserung des *discovery potential* von IceCube für galaktische Quellen hochenergetischer Neutrinos mit der Zielsetzung eines besseren Verständnisses der Hochenergieprozesse in unserer Galaxie. Zwei Punkte sind für das Erreichen dieses Ziels von Bedeutung: (1) die Nachweisfähigkeit von IceCube im Energiebereich von $100 \text{ GeV} < E < 1 \text{ TeV}$ zu verbessern und (2) eine Methode zu entwickeln, die den minimal nachweisbaren Fluss pro Punktquelle herabsetzt. Die Verbesserung der Detektorleistung bei Energien unterhalb 1 TeV wird erreicht, indem der IceCube Detektor mit 22 Strings sowie der AMANDA (Antarctic Muon And Neutrino Detector Array) Detektor zu einer Detektorkonfiguration kombiniert werden. Die Datenverarbeitung wurde konzipiert, um so viele gute niederenergetische Ereignisse wie möglich im Datensatz zu belassen. Dadurch erreicht diese Analyse die beste Sensitivität für Quellen mit Neutrinospektren steiler als E^{-2} und/oder einem Cutoff unterhalb 1 PeV. Das zweite Ziel dieser Arbeit ist die effiziente Suche nach hochenergetischen Neutrinos aus der Sternbildungsregion im Sternbild Cygnus in der Galaxis. Um die Suche auf mehr als eine Punktquelle auszuweiten, entwickelte ich eine Methode — basierend auf einer Zwei-Punkt Analyse — um Ereignismuster in einer ausgedehnten Region nachzuweisen, welche in konventionellen Punktquellen-Analysen unentdeckt bleiben könnten. Die Ergebnisse dieser Methode zeigen, dass der minimale nachweisbare Fluss pro Punktquelle um $\sim 26\%$ - 59% bezüglich einer Standard-Punktquellen-Analyse reduziert wird, vorausgesetzt es ist mehr als eine Punktquelle in der untersuchten Region vorhanden. Diese Methode wurde auf die Cygnus-Region der Galaxis angewandt, unter Verwendung des Datensatzes, der sich aus dem vereinten Detektor IceCube 22 Strings plus AMANDA ergibt, und liefert eine Signifikanz von $2,3\sigma$.

Contents

1	Introduction	1
1.1	Gamma-ray and neutrino production	3
1.1.1	Leptonic mechanisms	3
1.1.2	Hadronic mechanisms	6
1.1.3	HE Photon Interaction	11
1.2	High energy particles in the Galaxy	13
1.2.1	Galactic accelerators and environment	15
1.2.2	Supernova remnants and pulsar wind nebulae	24
1.2.3	High Mass X-ray Binaries and Microquasars	28
2	The IceCube neutrino observatory	33
2.1	Detection principle	34
2.1.1	Neutrino interactions	34
2.1.2	Cherenkov radiation	35

2.1.3	Signal and background in IceCube	35
2.2	The detection medium: the ice at the South Pole	36
2.3	The IceCube detector	37
2.4	Data Acquisition	41
2.4.1	The Digital Optical Module (DOM)	41
2.4.2	Filters	44
2.5	Data analysis in IceCube	44
2.5.1	Event reconstruction	45
2.5.2	Event Simulation	48
3	Analysis of the data obtained with IC22+AMANDA	51
3.1	Strategy	52
3.2	Datasets	53
3.3	PART 1: Elimination of atmospheric muons	54
3.3.1	Level 1: event filtering with first guess algorithms	56
3.3.2	Level 2: likelihood reconstruction	56
3.3.3	Level 3: S/N discrimination	57
3.3.4	Level 4: neutrino level	62
3.4	PART 2: search for neutrinos from the Galaxy	67
3.4.1	Galactic plane scan	67
3.4.2	Discovery Potential	68
4	Multi Point Source analysis for extended regions	71
4.1	Concepts and methods in the analysis of event patterns	73
4.1.1	Hot spot analysis	74
4.1.2	Two-point analysis	76

<i>Contents</i>	v
4.2 Multi Point Source (MPS) analysis	76
4.3 Performance and discovery potential of the MPS	81
4.3.1 PDF of the null hypothesis	82
4.3.2 Comparison with current search methods	84
4.4 Application to the Cygnus region	86
4.4.1 Discovery potential to clustered and diffuse emission	87
5 Results and Conclusions	91
5.1 Galactic Plane Scan	91
5.1.1 Results and discussion	91
5.2 The Cygnus Region in IC22+AMANDA	92
5.2.1 Results	93
5.2.2 Neutrino upper limits	96
5.3 Summary and conclusions	97
Acknowledgements	99

Chapter 1

Introduction

The Universe is filled with high energy particles; we can observe them through the interactions which take place directly on Earth or on their way towards us. In the first case, we are talking about cosmic-ray detection; in the latter case we have indirect evidence through the observation of gamma-rays and eventually neutrinos.

Particles of extraterrestrial origin with energies ranging between 10^9 - 10^{14} eV have been registered in photographic plates already since 1929 (1). At the very highest energies, they are detected by large air shower arrays, reaching $\sim 3 \times 10^{20}$ eV for the highest energetic particles observed (2), (3). These high energy particles can interact close to their sources of origin, or in the intergalactic or interstellar medium on their way towards us, generating gamma-rays and neutrinos in the process. This motivated the development of gamma-ray and neutrino astronomy. Cosmic-rays, gamma-rays and neutrinos are intimately related by the underlying processes of particle acceleration, giving rise to the so-called particle astronomy. Cosmic-ray astronomy has provided the energy spectrum and composition of cosmic-rays, and the challenge to explain the acceleration mechanisms which produce the highest energies observed. Gamma-rays have provided the first evidence of particle acceleration up to TeV energies from a number of sources; however, the hadronic or leptonic nature of the observed emission remains unknown, and the initial spectra of the primary particles is difficult to compute due to the fact that the observed emission may be partially absorbed, or even due to secondary products of the interactions of the relativistic particles with the surrounding media. The young field of neutrino astronomy is expected to complement these observations. High energy neutrinos are mostly produced in decays of unstable particles produced in hadronic interactions; they can freely penetrate through radiation, matter and magnetic fields, providing unambiguous evidence of hadronic acceleration from the sources detected.

The observations of extraterrestrial neutrinos require huge detector volumes and large integration times in order to have a significant signal in the detector. In the energy range $100 \text{ GeV} \lesssim E_\nu \lesssim 10 \text{ TeV}$, the final data sample in a neutrino telescope is dominated by the background of atmospheric neutrinos (4). Motivated by the search of pevatrons, high

energy neutrino telescopes reduce the background component by restricting the energy range of the analysis above a few TeV (5), (6), (7). The performance and sensitivity of the analysis are then optimized for neutrino signals following an E^{-2} spectrum (based on the theory of Fermi shock acceleration). and assuming that there is no energy cutoff up to at least 1 PeV. In this scenario, the latest studies of the IceCube performance (5) indicate a sensitivity after 1 year of operation of the full detector to point sources of high energy neutrinos at the level of $\sim 3 \times 10^{-12}$ TeVcm $^{-2}$ s $^{-1}$ (see Fig. 2 in (5)). However, the knee in the cosmic-ray spectrum at a few PeV suggests a break in the neutrino spectrum from galactic sources below 100 TeV. In addition, measurements of the gamma-ray spectrum from a number of sources in our galaxy, indicate that the high energy emission from potential neutrino sources can deviate significantly from the scenario of constant E^{-2} emission up to 1 PeV. In some of the cases observed, the spectrum of the gamma-ray sources presents an energy cutoff around a few TeV (8), (9) and/or a spectrum steeper than E^{-2} (10). For an E^{-2} with a cutoff at 100 TeV, the signal present in the final sample is already 42% less with respect to the one obtained assuming no cutoff up to 1 PeV, because of the rise of the neutrino cross section with energy. Even though these scenarios do not prevent the arrival of neutrinos of energies $100 \text{ TeV} \lesssim E_\nu \lesssim 1 \text{ PeV}$ to the detector, the total number of those is significantly reduced with respect to the E^{-2} , not cutoff approximation. As a consequence, the minimum detectable flux per point source can rise significantly for these galactic scenarios.

Given the limited sensitivity of neutrino telescopes, it is desirable to count with analysis strategies which help to identify a weak extraterrestrial component in the data. At this point, the source phenomenology comes into play in order to (1) select the most promising candidates, and (2) develop analysis strategies according to the nature of the source(s) under observation.

Establishing the connection between neutrinos and gamma-rays (or the lack of them) is an important step towards the selection of candidates to neutrino emission. The interactions of high energy particles which give rise to neutrino emission also produce gamma-rays of the same energy. Therefore, TeV gamma-ray sources are natural targets for neutrino telescopes. It is important to understand the mechanisms of gamma-ray production in order to select the most promising scenarios, since gamma-rays can also be efficiently produced by leptonic mechanisms. Absorption of gamma-rays also plays a role in analysis of neutrino data, in order to select potential sources of neutrinos which are weak in gamma-rays and be able to explain a possible discrepancy between neutrinos and gamma-rays.

In our galaxy, observations with the VERITAS and MAGIC telescopes (11), (12), and the H.E.S.S. (13) and Milagro (14) surveys of the galactic plane, have revealed a population of TeV sources plus diffuse emission (15), (16), (17), (18), (19). The high energy gamma-rays observed are attributed to the interaction of high energy particles produced by galactic accelerators in the interstellar medium. A neutrino signal from the Galaxy is also expected

from the interaction of nuclei with the ambient matter and radiation fields. Neutrino telescopes investigate in their data the spatial event pattern of the candidate neutrino events, searching for astrophysical sources of high energy neutrinos. The study of the most promising sites for neutrino production in the Galaxy is a key point in this work. This chapter is intended to present the most relevant aspects concerning the phenomenology of possible neutrino emitters, place them under the context of present neutrino telescopes, and discuss the reliability of a neutrino detection in the next years.

1.1 Gamma-ray and neutrino production

This section presents an overview of the main mechanisms of interactions of high energy particles with matter and radiation fields in an astrophysical context, as part of the theoretical background required to establish the link between gamma-rays and neutrinos. Detailed modeling of the particle interaction processes is beyond the needs of this work. Thus, I will restrict the discussion to the most relevant aspects for this work, that is, the production of high energy gamma-rays and neutrinos and its relation with the primary particle spectrum and the environment. For a detailed description about the interactions of high energy particles see (20), (21).

The models describing astrophysical phenomena which give rise to gamma-rays of energies above 100 GeV can be divided into two groups. The first group involves interactions of high energy leptons, namely electron bremsstrahlung and inverse Compton effect. The second group involves the acceleration and interaction of hadrons, establishing the link between gamma-rays and neutrinos.

1.1.1 Leptonic mechanisms

This section covers those processes which generate high energy gamma-rays through the interaction of relativistic electrons with matter and radiation.

Electron bremsstrahlung

This type of emission is generated by charged particles when deflected in the electric field of other charges. In a high energy astrophysical context, this process is the main responsible for the energy losses of relativistic electrons in the presence of atomic or molecular material. The main force acting by the atom on the incident electron is due to the Coulomb field of the nuclear charge. The electrons in the atom play two roles: on one hand, they screen

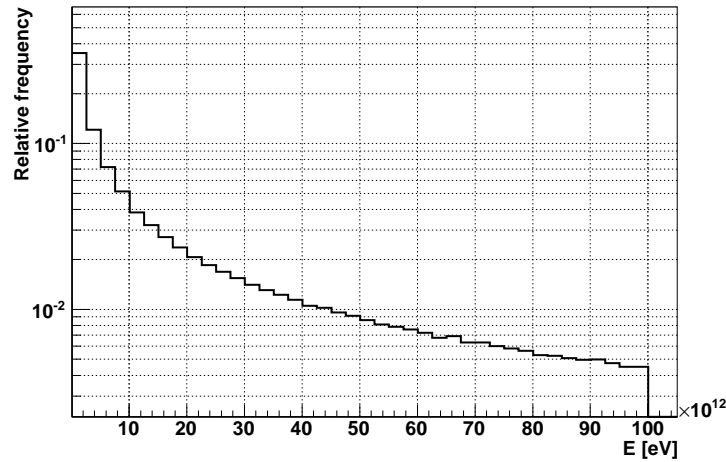


Figure 1.1: *Relative frequency of bremsstrahlung gamma-ray photons of energy E produced by an ultrarelativistic electron of energy 100 TeV moving in an hydrogen gas ($Z = 1$).*

the Coulomb field of the nucleus and reduce the cross section for bremsstrahlung emission. On the other hand, they act as individual particles and the bremsstrahlung process may also take place in the collision with an atomic electron. Therefore, both electron-nucleus and electron-electron relativistic bremsstrahlung can contribute to the emitted gamma-ray spectrum, and they have to be summed in order to give the total bremsstrahlung cross section, σ_{bremss} .

The average cross section for electron-atom bremsstrahlung interaction from the full relativistic quantum treatment of Bethe and Heitler can be approximated by (20):

$$\sigma_{bremss} = \frac{Z(Z + 1.3)e^6}{16\pi^3\epsilon_0^3 m_e^2 c^5 \hbar} \left[\ln \left(\frac{183}{Z^{1/3}} + \frac{1}{8} \right) \right] = \sigma_0 Z (Z + 1.3) \left[\ln \left(\frac{183}{Z^{1/3}} + \frac{1}{8} \right) \right] \quad (1.1)$$

where $\sigma_0 = 2.31 \times 10^{-27} \text{ cm}^2$. The term that goes with $\propto Z^2$ in equation 1.1 represents the contribution from electron-nucleus bremsstrahlung, whereas the term that scales with $\propto Z$ represents the contribution from electron-electron bremsstrahlung with the bound electrons in the atom.

Fig. 1.1 shows the relative frequency of gamma-ray photons with energy E produced by an electron of 100 TeV moving in an hydrogen gas ($Z = 1$). The probability of the emission of a photon of energy E by a relativistic electron goes with E^{-1} up to the maximum energy allowed $E_{max} = (\gamma_e - 1)m_e c^2$. Given electrons of energy ~ 100 TeV, the probability that they produce photons with energies above 10 TeV is very small, and the electron will lose its energy progressively through successive scatterings which will give rise to a number of

lower energetic photons. However, there is a non-negligible probability that electrons with energies in the range $100 \text{ TeV} < E_e < 1000 \text{ TeV}$ lose a significant fraction of their energy in creating a TeV photon. For this reason, although this process is more important at low gamma-ray energies, in galactic accelerators surrounded by a high density environment the bremsstrahlung process has to be taken into account as a possible mechanism of gamma-ray production.

The photon spectrum measured at Earth produced by bremsstrahlung from relativistic electrons can be calculated with the total cross section and summing over all the electrons which can contribute to the emission:

$$\frac{d\Phi(E)}{dEdAdt} = \frac{\rho V}{4\pi d^2} \int_E^{E_e^{max}} J_e(E_e) \sigma_{bremss} \frac{dE_e}{E} \quad (\text{at Earth}) \quad (1.2)$$

where $J_e(E_e)$ is the energy distribution of the gas of relativistic electrons ($\frac{dN_e}{dEdAdt}$ at source); ρ is the mean target density within the volume V , and d is the distance to the source of the gamma-rays.

Adopting a power-law distribution for the electron energies: $J_e(E_e) = K E_e^{-p}$, equation 1.2 yields:

$$\frac{d\Phi(E)}{dEdAdt} = \frac{\rho V}{4\pi d^2} \int_E^{\infty} \sigma_{bremss} K E_e^{-p} \frac{dE_e}{E} = \frac{\rho V}{4\pi d^2} \frac{\sigma_{bremss} K E^{-p}}{p-1} = \frac{\rho V \sigma_{bremss}}{4\pi d^2 (p-1)} J_e(E) \quad (1.3)$$

Therefore, gamma-ray production by bremsstrahlung is proportional to the electron energy distribution and the density of the ambient gas, ρ . If E_e^{max} is the maximum electron energy, the photon energy must be $\hbar\omega < E_e^{max}$; and the emission spectrum will show a cut-off at this energy.

Inverse Compton scattering

The inverse Compton effect is the increase in the energy of a photon after scattering off an electron. In the gamma-ray regime, the Klein-Nishina formulism describes the scattering of low energy photons by relativistic electrons (22). In this case the scattered photon carries away a large fraction of the electron energy, $E \approx \gamma_e mc^2$, which makes the inverse Compton process one of the main gamma-ray production mechanisms in astrophysical environments.

To obtain the total spectrum of the upscattered photons at Earth, one has to integrate over all the electrons which can contribute to the spectrum above an energy E . That is,

$$\frac{d\Phi(E)_{IC}}{dEdAdt} = \frac{1}{4\pi d^2} \int_E^{E_e^{max}} \Phi(E)_{single} J_e(E_e) dE_e \quad (at\ Earth) \quad (1.4)$$

where $\Phi(E)_{single}$ is the spectrum of the scattered radiation ($\frac{dN}{dEdt}$ at source) produced by a single electron of energy E_e ; $J_e(E_e)$ is the electron energy distribution ($\frac{dN_e}{dE}$ at source), and d is the distance to the source.

The term $\Phi(E)_{single}$ has to be determined using the Klein-Nishina cross section and the density of target photons at each point on the electron path. The electron suffers collisions with photons moving at various angles with respect to its path, and therefore the geometry of the scattering enters in the calculation of the spectrum. A common approximation is that the electron moves in an isotropic radiation field with differential density $dn = n(E_\star)dE_\star$ (circumstance that is usually met in astrophysical sources), where E_\star is the energy of the target photons. Within this approximation, and using the average Klein-Nishina cross section, the photon spectrum corresponding to a single scattering can be written as (21):

$$\frac{d\Phi(E)_{single}}{dEdt} = \int_{E_\star^{min}}^{E_\star^{max}} \frac{2\pi r_0^2 m_e c^3 n(E_\star)}{E_e E_\star} \Psi(E_\star, E_e, E) dE_\star \quad (at\ source) \quad (1.5)$$

where

$$\Gamma_E = \frac{4E_\star E_e}{m_e^2 c^4} \quad q = \frac{E}{\Gamma_E(E_e - E)} \quad (1.6)$$

$$\Psi(E_\star, E_e, E) = \left(2q \ln q + (1 + 2q)(1 - q) + \frac{1}{2} \frac{(\Gamma_E q)^2}{1 + \Gamma_E q} (1 - q) \right) \quad (1.7)$$

Figure 1.2 shows an example of inverse compton radiation of electrons in the environment of a massive OB-type star. The radiation spectrum of such stars can be well approximated by a blackbody spectrum at a temperature $T = 28000$ K (peak in the UV). The plot shows the relative frequency of photons produced after scattering of stellar photons off a 100 TeV electron obtained making use of equation 1.5. At these energies, the electron loses practically all its energy in a single scattering, transferring it to the photon.

The availability of low energy radiation in astrophysical environments and the efficient process of transfer of energy from the electron to the target photon makes the inverse Compton effect one of the dominant processes in the production of gamma-rays in the range of Cherenkov telescopes.

1.1.2 Hadronic mechanisms

The interactions of high energy protons or ions with matter and radiation in astrophysical environments produce unstable secondary particles which generate gamma-rays and

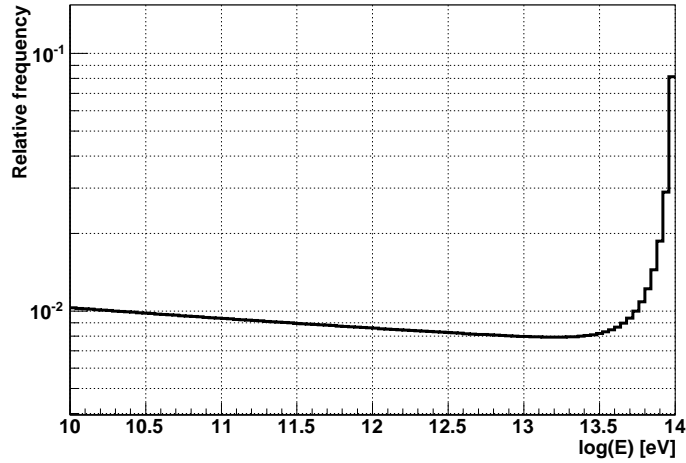


Figure 1.2: *Relative frequency of gamma-ray photons with energy E produced by an electron of energy 100 TeV upscattering blackbody radiation at temperature $T = 28000$ K (UV photons). The distribution has a peak at the highest energies, meaning that the electron preferably losses all its energy in creating a gamma-ray photon.*

neutrinos from their decay, establishing a deep link between cosmic-rays, neutrinos and gamma-rays. Accurate calculations of the spectra of gamma-rays and neutrinos from these processes require to perform simulations of pp , $p\gamma$ interactions in order to deal with complicated cross sections and characteristics of particle production. Kelner et al. (2006, 2008) (23), (24) provided analytical parametrizations for the spectra of secondary gamma-rays and leptons from the energy distributions of mesons obtained in the simulation of all the relevant channels in pp and $p\gamma$ interactions. Their calculations constitute an accessible way to relate the predictions from hadronic models on the gamma-ray spectra with current observations, as well as to establish the link between gamma-rays and neutrinos in hadronic scenarios in absence of gamma-ray absorption.

This section summarizes the main steps presented in (23) to relate the primary proton spectrum with the spectrum of secondary gamma-rays and neutrinos in pp interactions, since this procedure was used several times along this thesis. Details on the calculation of the gamma-ray and neutrino spectrum from $p\gamma$ interaction, are reported in (24). The reason why the pp process is favored with respect to the $p\gamma$ relies on energetic considerations about galactic sources. The cross section for pp interactions is two orders of magnitude higher than the one for $p\gamma$, requiring less energy in relativistic protons for the same luminosity in neutrinos, providing the matter density is sufficient to allow the interaction of the high energy protons. Therefore, given our current understanding about the energy budget of galactic accelerators, I consider more favorable the production of high energy neutrinos through pp interactions.

pp interactions

The collision between a relativistic primary proton and a target proton leads to the generation of mesons through different reaction channels. The main production of gamma-rays takes place from the decay of π^0 and η mesons, whereas neutrinos are produced from the decay of π^\pm and K mesons:

$$\pi^0 \longrightarrow 2\gamma \text{ (98.7\%)}$$

$$\pi^+ \longrightarrow \mu^+ \nu_\mu \text{ (99.9\%)}$$

$$\pi^- \longrightarrow \mu^- \nu_\mu \text{ (99.9\%)}$$

$$\eta \longrightarrow 2\gamma \text{ (39.5\%)}$$

$$\eta \longrightarrow 3\pi^0 \text{ (32.24\%)}$$

$$\eta \longrightarrow \pi^+ \pi^- \pi^0 \text{ (22.6\%)}$$

$$\eta \longrightarrow \pi^+ \pi^- \gamma \text{ (5\%)}$$

$$K \longrightarrow \mu^+ \nu_\mu \text{ (63.43\%)}$$

$$K \longrightarrow \pi^+ \pi^- \text{ (21.13\%)}$$

$$K \longrightarrow \pi^+ \pi^+ \pi^- \text{ (5.57\%)}$$

$$K \longrightarrow \pi^0 e^+ \nu_e \text{ (4.87\%)}$$

$$K \longrightarrow \pi^+ \pi^0 \pi^0 \text{ (1.73\%)}$$

The calculations of the energy spectra of the secondary products of pp interactions are usually carried out with the use of hadronic Monte Carlo generators, which are based on theoretical models and data from accelerators of the inclusive cross sections. From the energy distribution of the mesons produced in the process, $J(E)$, it is possible to obtain the energy distribution of gamma-rays and neutrinos produced in their decay. In the case of pions, it is possible to obtain directly the energy distribution of gamma-rays from the decay of π^0

$$Q_\gamma(E_\gamma) = 2 \int_{E_\gamma}^{\infty} J_{\pi^0}(E_{\pi^0}) \frac{dE_{\pi^0}}{E_{\pi^0}} \quad (1.8)$$

where the factor 2 indicates that two gamma-ray photons are produced at the decay of π^0 .

The calculation of the energy spectra of muon neutrinos requires the treatment of the particle decay modes $\pi \longrightarrow \mu \nu_\mu$ and $\mu \longrightarrow e \nu_\mu \nu_e$, resulting in energy distribution functions

$f_{\nu_\mu}^{(1)}(E_{\nu_\mu}, E_\pi)$ for muon neutrinos from the direct decay $\pi \rightarrow \mu\nu_\mu$; and $f_{\nu_\mu}^{(2)}(E_{\nu_\mu}, E_\mu)$ for muon neutrinos from the decay $\mu \rightarrow e\nu_\mu\nu_e$.

$$Q_{\nu_\mu}(E_{\nu_\mu}) = 2 \int_{E_{\nu_\mu}}^{\infty} (f_{\nu_\mu}^{(1)}(E_{\nu_\mu}, E_\pi) + f_{\nu_\mu}^{(2)}(E_{\nu_\mu}, E_\mu)) J_\pi(E_\pi) \frac{dE_\pi}{E_\pi} \quad (1.9)$$

where the factor 2 represents the contribution from both π^+ and π^- . For derivations of the functions $f_{\nu_\mu}^{(1)}(E_{\nu_\mu}, E_\pi)$ and $f_{\nu_\mu}^{(2)}(E_{\nu_\mu}, E_\pi)$ see (23).

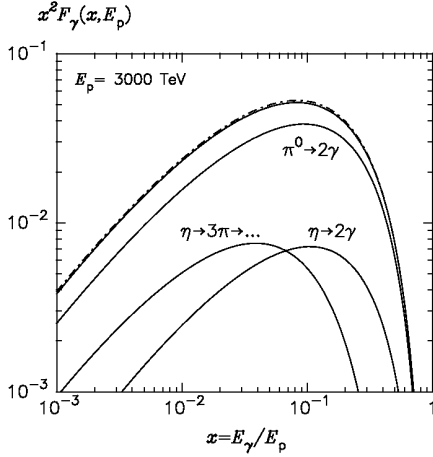


Figure 1.3: Energy spectra of gamma-rays from pp interactions showing the contributions from π^0 and η meson decay assuming an energy of 3000 TeV for the incident proton. Figure from (23).

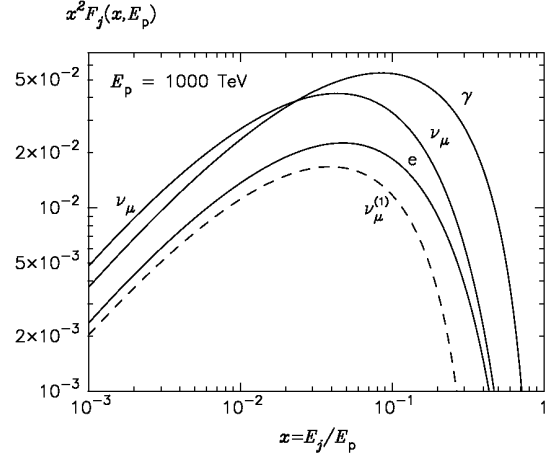


Figure 1.4: Energy spectra of all the decay products produced at pp interactions assuming an energy of 1000 TeV for the incident proton. Figure from (23).

Fig. 1.3 shows the contribution of π^0 and η decay to the spectrum of gamma-rays produced in a single interaction with an energy of the incident proton of 3000 TeV (23). Fig. 1.4 shows the spectra of secondaries: gamma-rays, neutrinos and electrons produced after interaction of a proton of energy 1000 TeV. The parametrizations of the gamma-ray and lepton spectrum from pp interactions given in (23) achieve an accuracy of better than a several percent in the energy range of primary protons $0.1 \text{ TeV} \leq E_p \leq 10^5 \text{ TeV}$. In particular, the authors find the following analytical expressions for the spectrum of gamma-rays and neutrinos produced in a single collision:

$$\begin{aligned} F_\gamma(x, E_p) &= B_\gamma \frac{d}{dx} \left[\ln(x) \left(\frac{1 - x^{\beta_\gamma}}{1 + k_\gamma x^{\beta_\gamma} (1 - x^{\beta_\gamma})} \right)^4 \right] \\ &= B_\gamma \frac{\ln(x)}{x} \left(\frac{1 - x^{\beta_\gamma}}{1 + k_\gamma x^{\beta_\gamma} (1 - x^{\beta_\gamma})} \right)^4 \left[\frac{1}{\ln(x)} - \frac{4\beta_\gamma x^{\beta_\gamma}}{1 - x^{\beta_\gamma}} - \frac{4k_\gamma \beta_\gamma x^{\beta_\gamma} (1 - 2x^{\beta_\gamma})}{1 + k_\gamma x^{\beta_\gamma} (1 - x^{\beta_\gamma})} \right] \end{aligned} \quad (1.10)$$

where $x = E_\gamma/E_p$. Defining $L \equiv \ln(E_p/1TeV)$, the parameters $B_\gamma, \beta_\gamma, k_\gamma$ are given by

$$B_\gamma = 1.30 + 0.14L + 0.011L^2 \quad (1.11)$$

$$\beta_\gamma = \frac{1}{1.79 + 0.11L + 0.008L^2} \quad (1.12)$$

$$k_\gamma = \frac{1}{0.801 + 0.049L + 0.014L^2} \quad (1.13)$$

The spectrum of ν_μ from the decays $\pi \rightarrow \mu\nu_\mu$ has two contributions: $F_{\nu_\mu^{(1)}}(x, E_p)$, from the direct π decay, and $F_{\nu_\mu^{(2)}}(x, E_p)$, from the decay of the muon:

$$\begin{aligned} F_{\nu_\mu^{(1)}}(x, E_p) &= B' \frac{d}{dy} \left[\ln(y) \left(\frac{1 - y^{\beta'}}{1 + k'y^{\beta'}(1 - y^{\beta'})} \right)^4 \right] \\ &= B' \frac{\ln(y)}{y} \left(\frac{1 - y^{\beta'}}{1 + k'y^{\beta'}(1 - y^{\beta'})} \right)^4 \left[\frac{1}{\ln(y)} - \frac{4\beta'y^{\beta'}}{1 - y^{\beta'}} - \frac{4k'\beta'y^{\beta'}(1 - 2y^{\beta'})}{1 + k'y^{\beta'}(1 - y^{\beta'})} \right] \end{aligned} \quad (1.14)$$

where $x = E_{\nu_\mu}/E_p$, $y = x/0.427$,

$$B' = 1.75 + 0.204L + 0.010L^2 \quad (1.15)$$

$$\beta' = \frac{1}{1.67 + 0.111L + 0.0038L^2} \quad (1.16)$$

$$k' = 1.07 - 0.086L + 0.002L^2 \quad (1.17)$$

The spectrum of ν_μ produced from the decay of a muon $\mu \rightarrow e\nu_e\nu_\mu$ is expressed in (23) as

$$F_{\nu_\mu^{(2)}}(x, E_p) = B \frac{(1 + k(\ln x)^2)^3}{x(1 + \frac{0.3}{x^\beta})} (-\ln x)^5 \quad (1.18)$$

$$B = \frac{1}{69.5 + 2.65L + 0.3L^2} \quad (1.19)$$

$$\beta = \frac{1}{(0.201 + 0.062L + 0.00042L^2)^{\frac{1}{4}}} \quad (1.20)$$

$$k = \frac{0.279 + 0.141L + 0.0172L^2}{0.3 + (2.3 + L)^2} \quad (1.21)$$

From an arbitrary energy distribution of protons, $J_p(E_p)$, the spectrum of gamma-rays and neutrinos from pp interactions can be calculated by solving the integrals:

$$\begin{aligned} \Phi_\gamma(E_\gamma) &\equiv \frac{dN_\gamma}{dE_\gamma} \\ &cn_H \int_0^\infty E_\gamma \sigma_{inel}(E_p) J_p(E_p) F_\gamma\left(\frac{E_\gamma}{E_p}, E_p\right) \frac{dE_p}{E_p} \end{aligned} \quad (1.22)$$

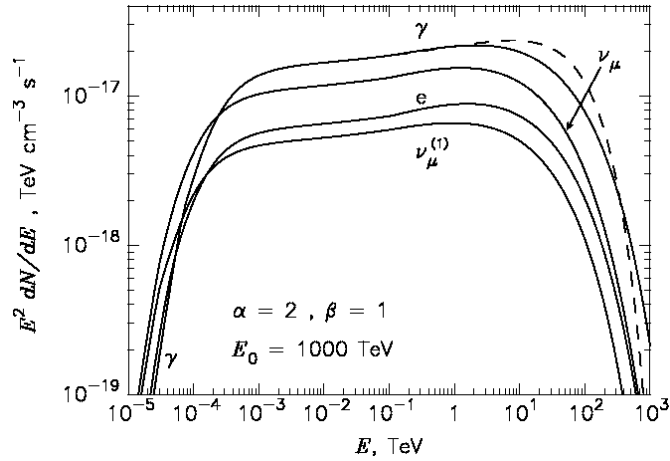


Figure 1.5: *Energy spectra of gamma-rays and leptons from pp interactions. Figure taken from (23).*

and its equivalent for neutrinos. The contribution of the K meson decay to the muon neutrino flux has not been included in these calculations; as a result, the neutrino flux from equations 1.14 and 1.18 is underestimated by a factor of 1.1 (23).

Figure 1.5 shows the spectra of gamma-rays and leptons from pp interactions assuming a proton distribution of the form

$$J_p(E_p) = \frac{A}{E_p^\alpha} \exp \left[- \left(\frac{E_p}{E_0} \right)^\beta \right] \quad (1.23)$$

Relevant aspects concerning the gamma-ray and neutrino spectra from this process are symbolized in these plots. The relative scale between the energy cutoff in the spectra of protons, gamma-rays and neutrinos is nearly independent of the energy of the primary protons, and corresponds approximately to 1: 0.1: 0.05, respectively. Therefore, the energy cutoff in the proton spectrum, E_0 , has an impact on the gamma-ray and neutrino spectrum at much lower energies.

1.1.3 HE Photon Interaction

At the energies considered in this work, $\gamma\gamma$ pair production is the dominant process for interactions of high energy photons in astrophysical environments. In the proximity of very dense radiation fields, the cross section for pair production from interactions of gamma-rays with the ambient photons exceeds the cross section of interactions of protons and electrons with the same target photons. As a result, cosmic-rays and gamma-rays can

not leave the region of their production, and they initiate electromagnetic cascades in the surrounding radiation fields, eventually emerging as radiation at lower energies. Neutrinos produced in hadronic interactions on the contrary can freely escape the source. This situation may take place in the environments of very massive stars, in which the cross section for $\gamma\gamma$ pair production peaks at photon energies above 100 GeV (see Fig. 1.17). This section investigates the absorption of gamma-rays, in which the link between gamma-rays, neutrinos and cosmic-rays will not be evident from the observations.

Pair Production

The intensity of gamma-rays of energy E can be reduced by the effect of absorption in a media of opacity $\tau(E)$ according to $I_{observed} = Ie^{-\tau(E)}$.

The opacity seen by a gamma-ray of energy E travelling in the direction $\hat{\mathbf{e}}_\gamma$ due to photons of energy ϵ_\star emitted along the direction $\hat{\mathbf{e}}_\star$ is (25):

$$\tau_{\gamma\gamma} = \int (1 - \hat{\mathbf{e}}_\gamma \hat{\mathbf{e}}_\star) n_{\epsilon_\star} \sigma_{\gamma\gamma} d\epsilon_\star d\Omega dl \quad (1.24)$$

where n_{ϵ_\star} is the density of the target radiation field, $\sigma_{\gamma\gamma}$ is the cross section for pair production, and l is the path of the gamma-ray photon. The term $(1 - \hat{\mathbf{e}}_\gamma \hat{\mathbf{e}}_\star)$ can be written as $(1 - \cos\psi)$, where ψ is the angle between the gamma-ray photon and the target photon.

The cross section for the process $\gamma\gamma \rightarrow e^\pm$ is

$$\sigma_{\gamma\gamma} = \frac{1}{2} \pi r_0^2 (1 - \beta^2) [(3 - \beta^4) \ln \frac{1 + \beta}{1 - \beta} - 2\beta(2 - \beta^2)] \quad (1.25)$$

where r_0 is the classical electron radius, and βc is the electron velocity in the center of mass system.

Following (25), after the transformation $\beta = (1 - 1/s)^{1/2}$, $\sigma_{\gamma\gamma}$ depends only on the variable s , defined as

$$s = \frac{\epsilon_\star E_\gamma}{2m_e^2 c^4} (1 - \cos\psi) \quad (1.26)$$

where the γ -ray is absorbed only if $s > 1$.

As a result, the dependencies on the calculation of the γ -ray absorption are the target radiation fields, the location of the γ -ray production and the angle of interaction between the target photon and the γ -ray photon at every point in the path of the γ -ray photon. The geometry of the problem is therefore very important, making the calculations of possible absorption in the spectra of gamma-rays strongly model dependent.

1.2 High energy particles in the Galaxy

The current measurements of the cosmic radiation from the Galaxy are helping to construct a comprehensive picture about the sources of cosmic-rays, the mechanisms of propagation, and the interaction of cosmic-rays with the gas and the radiation fields of the Galaxy. With completion in 2011, the IceCube neutrino observatory is expected to play a decisive role towards the understanding of the high energy processes in the Galaxy through the unambiguous detection of hadronic cosmic-ray sources. A major advance in the field took place during the last years from the observations of gamma-ray telescopes, both space and ground based, since they provided indirect evidence of the interaction of both nuclei and electrons.

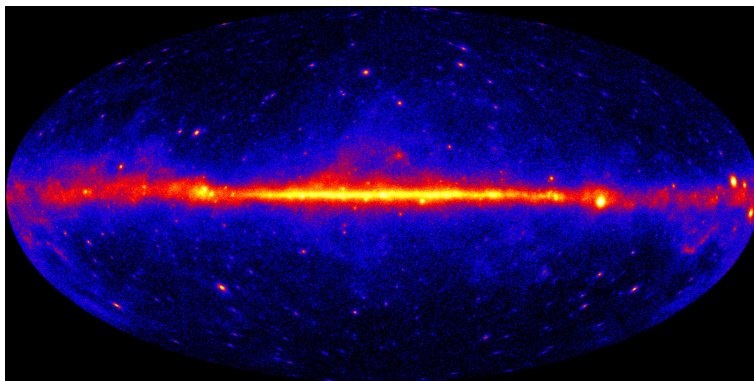


Figure 1.6: *FERMI LAT skymap at $E > 300$ GeV.*

Gamma-rays with energies above 100 MeV are observed throughout the Galaxy, produced by interactions of CR protons and electrons with gas and radiation from the interstellar medium (ISM). At large scales, the Galaxy emits a diffuse flux of gamma-rays attributed to the interaction of cosmic-rays after their diffusion in the galactic magnetic fields (see Fig. 1.6). Models of the high energy emission from the Galaxy rely on assumptions about the distribution of cosmic-ray sources and on calculations of the cosmic-ray propagation to reproduce both the cosmic-ray and gamma-ray data. The propagation and interaction of cosmic-rays is affected by the galactic structure and galactic magnetic fields. The most important aspects for the interaction of cosmic-rays are the gas content and the interstellar radiation field. Surveys of atomic and molecular gas (26) have provided large scale maps of the Milky Way gas distribution (see Fig. 1.7) which are used to predict gamma-ray fluxes from the interaction of diffuse cosmic-rays within the galactic disk (28).

Localized excesses of high energy gamma-rays with respect to models of cosmic-ray propagation can be interpreted as the result of cosmic-ray interactions in regions of enhanced

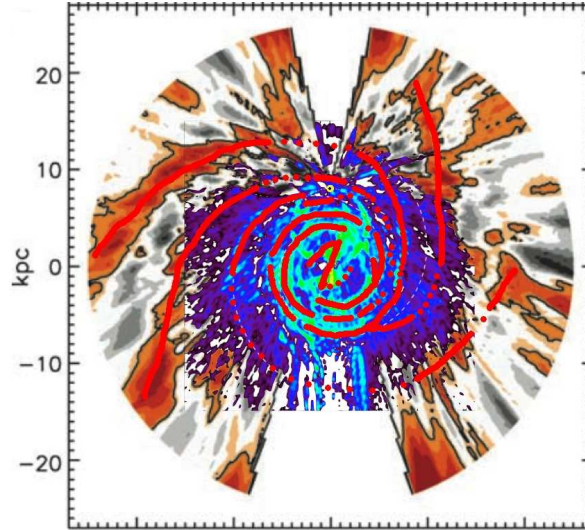


Figure 1.7: *Map of the distribution of molecular (CO) gas in the galaxy and thickness HI layer in the outer disk. The spiral arms of the Galaxy are drawn with red lines. The Sun is represented by a yellow dot. Figure taken from (27).*

matter density¹, or due to the presence of galactic accelerators injecting high energy particles which interact close to their sources of origin.

Observed excesses in TeV gamma-rays are of interest for neutrino telescopes due to the connection between gamma-rays and neutrinos. One should note however that the morphology and strength of a possible neutrino source can be indeed quite different from its gamma-ray counterpart, due to leptonic contributions to the TeV emission and/or possible absorption of gamma-rays. Therefore, the link between TeV gamma-rays and neutrinos has to be done cautiously. When investigating the gamma-neutrino connection, the environment of the potential sources of cosmic-rays is of crucial importance in order to determine to what extent neutrino production is an efficient process and/or whether gamma-ray absorption has to be considered.

There is an extensive discussion in the literature about possible sources of high energy neutrinos, based on modelling of the source spectral energy distribution and taking into account considerations about particle acceleration and source characteristics. Detailed source modelling is beyond the scope of this work, thus in this section I intend to give a general perspective of the most promising sites for neutrino production and discuss the peculiarities that can be considered as information for neutrino data analysis in order to optimize the discovery potential.

¹Cosmic-ray propagation models such as GALPROP (28) are limited to scales >10 pc; therefore small-scale variations in the matter density are not considered in these models.

1.2.1 Galactic accelerators and environment

The production of high energy neutrinos in our galaxy is intimately related with the efficient acceleration of hadrons in galactic sources. Proposed sources of energy for cosmic-ray acceleration are the remnants of supernovas (both shell-type and pulsar wind nebula), the jets of microquasars, and the collective winds of massive stars. All these phenomena are associated with massive star formation.

The progenitors of potential galactic accelerators

The death of stars with initial mass above $\sim 8M_{\odot}$ takes place in the form of a core-collapse supernovae (Sn), leaving behind a compact remnant [a neutron star (NS) or a black hole (BH)] as well as great amounts of mass and energy injected into the interstellar medium.

The lifespan and the fate of a star is determined by its initial mass. Massive stars consume rapidly the hydrogen in their cores, reaching an average age of only a few Myr, compared to low mass stars which burn their fuel very slowly and last tens to hundreds of billions of years. The type of the progenitor star influences the remnant properties and the supernova explosion characteristics, like the amount of heavy elements synthesized and the total energy of the explosion. At their final stage of evolution the most massive OB stars enter the Wolf-Rayet (WR) phase, where most of their outer layers are ejected through strong stellar winds ($\sim 10^{-4}$ - $10^{-5}M_{\odot}$ /year from individual WR, ten times higher than the mass loss rate of single OB stars, with terminal wind speeds as high as 5000 km/s). This phase is maintained until the core collapses producing the explosion of the star.

Stellar evolutionary models estimate the mass and energy injected to the ISM by a starburst population using observational results and theoretical considerations (30). The overall contribution of a stellar population relies on its initial mass function (IMF), the metallicity (Z), and the star formation rate (SFR) history (i.e., instantaneous burst or continuous formation of stars). The models explore a wide parameter space by varying Z as well as the shape and mass limits of the IMF within acceptable ranges, which are based on observations from our Galaxy and other star forming galaxies. These calculations yield a range of values for the evolution of the mechanical luminosities from both stellar winds and Sn for a given SFR (31). In general, for an instantaneous burst, the winds of OB stars and WR dominate the injection of energy to the ISM over the first ~ 10 Myr, with kinetic luminosities ranging between $\sim 10^{38}$ - 10^{41} erg/s. In populations older than ~ 10 Myr core-collapse Sn dominates the energetics of the ISM injecting $\sim 10^{41}$ - $10^{41.8}$ erg/s during the next ~ 40 Myr, when the least massive star ($\sim 8M_{\odot}$) explodes. Therefore, the early-type OB stars dominate the injection of mass and energy to the interstellar medium through the overall contribution of their individual stellar winds and supernova explosions. The

Table 1.1: Properties of Dark Clouds, Clumps, and Cores from (34)

	Clouds	Clumps	Cores
Mass (M_{\odot})	10^3 – 10^4	50–500	0.5–5
Size (pc)	2–15	0.3–3	0.03–0.2
Mean density (cm^{-3})	50–500	10^3 – 10^4	10^4 – 10^5

most energetic star clusters would be represented by very massive clusters in which the WR phase starts to dominate over the main-sequence phase. Depending on the mass of the most massive stars in the cluster, this phase can start in clusters of ages between ~ 1 – 2 Myr for the most massive clusters, or ~ 3 Myr, for less massive clusters. The result being a region of the sky with a number of dead or dying massive stars with a great deal of energy available for particle acceleration (32).

Star forming regions are dominated by either massive stars or by low and intermediate mass stars. Massive stars are born in clusters and associations embedded within giant molecular clouds (GMCs), following a trend in which the most massive clusters harbor the most massive stars (33). Molecular clouds show a hierarchical structure: small dense cores are part of small clumps of gas which are themselves part of larger gas clumps, covering a wide spatial range of observations (34). Clumps are regions of enhanced density in which stellar clusters are typically formed, with sizes on the order of 0.3–3 pc. Cores are density condensations smaller than a clump which do not contain any smaller structure already bound, representing the earliest stages of formation of a star (35), (36). Table 1.1 shows the typical properties of clouds, clumps and cores from (34). The stars are formed more or less simultaneously in clusters or associations which are held together by the mutual gravitational attraction of its individual members. The difference between star cluster and association relies on the stellar space density; associations represent loose groups of physically related stars with $\rho_{\star} < 1 M_{\odot} \text{pc}^{-3}$, whereas in stellar clusters $\rho_{\star} > 1 M_{\odot} \text{pc}^{-3}$ (37), (38). Most of the known OB associations have sizes between several tens of pc in diameter up to < 300 pc (39), (37). Therefore, clustering of potential cosmic-ray sources may take place at spatial scales ranging between 0.3 pc - 300 pc, from the smallest massive stellar clusters observed to the largest OB associations. Assuming a distance of 3 kpc, this range corresponds to $\sim 20.6^{\hat{n}}$ up to 5.7° on the sky. This implies that, if gamma-rays and neutrino are actually produced by young, massive star clusters, the range of observation of clustering of gamma-ray and neutrino sources would span from point-like up to extended regions of several degrees with a number of sources inside (in the case of associations).

Some of the known remnants of Sn, in particular the population of single PSR in the Galactic disk, do not appear to be associated with any stellar cluster, or sometimes they are found moving away from their parent clusters (40), (41). Observations of these "runaway stars" are more linked to NS than to BH (42), (43). The most likely explanation is that,

during the Sn explosion, the recently created NS receive a higher velocity kick than BH, leaving the cluster in which they were born. As a consequence, the majority of NS are likely ejected from their natal clusters, whereas most black holes are retained, although this conclusion may be also the result of an observational bias. The discussion about isolated, potential sources of high energy neutrinos will be presented in sections 1.2.2 and 1.2.3. This section focuses on those sources which cluster due to their potential for neutrino telescopes.

Particle acceleration in massive star forming regions

There is a considerable literature concerning the production of cosmic-rays in clusters of OB stars due to stellar-winds/supernova blast wave shocks (44), (45), (46), (47), (48), (49), (50). Observational support to the theory of cosmic-rays accelerated in the environment of massive stars comes from measurements of primary cosmic-ray composition and cosmic-ray interaction products.

The measurements of the composition and the abundances of galactic cosmic-ray nuclei (52), (53) provide hints about the site of their acceleration (54). At low energies ($E < 10^{10}$ eV) measurements of the cosmic-ray isotopic and elemental abundances have shown that they are consistent with a mix of approximately 20% WR ejecta and 80% normal matter with solar system composition (55), (53). These results provide evidence of production of low energy cosmic-rays in the environment of massive star forming regions. At higher energies (10^{10} eV $< E < 10^{15}$ eV), although no significant changes in composition are observed (56), only the abundances of elemental species, without isotopic detail, are available and therefore the above mentioned results can not be extrapolated to higher energies.

The primary evidence of multi-TeV particle acceleration in young, massive star clusters comes from observations of TeV gamma-rays. So far, two open clusters have been confirmed as TeV gamma-ray emitters by the H.E.S.S. collaboration: Westerlund 1 (57), and Westerlund 2 (58). There is also tentative association of a number of massive clusters with unidentified sources in TeV gamma-rays (59), (60). However, it is still to determine whether the observed gamma-rays are the interaction products of cosmic-rays or if they are generated through inverse Compton by a population of relativistic electrons.

In an hadronic scenario, the energies of the gamma-rays and neutrinos produced in regions of massive star formation depend on the maximum energy at which protons are accelerated. Therefore, the chances of detecting TeV neutrinos from this type of regions depends in the first place on how much of the kinetic energy of the system is transferred into high energy protons, as well as the maximum energy to which they can be accelerated. This, however, represents one of the current open questions in high energy astrophysics, which neutrino telescopes are expected to answer in the next years.

Table 1.2: Properties of HII regions

	Classical	Ultracompact	Giant
Size (pc)	1–10	<0.1	~100
Mean density (cm^{-3})	10^2	10^4	30

From the theoretical point of view, early models predicted low energy gamma-rays from clusters of OB stars; however, it has been proven theoretically, (51), (46) that, under certain conditions, diffusive shock acceleration of energetic particles in these systems could account for the production of the PeV protons required to produce neutrinos in the energy range of the 1km^3 neutrino detectors.

Environment

Stellar clusters and associations are born in molecular clouds, and during their formation and early evolution they are completely embedded in molecular gas and dust. Through the lifetime of massive stars, the surrounding environment is strongly influenced by the stellar winds, ionizing radiation and heating of dust. Massive stars emit extreme UV radiation, which ionizes the surrounding media creating a HII region around the massive stars and their clusters. Classical HII regions have sizes of several parsecs and particle densities of the order of 10^2 cm^{-3} . However, there are also ultracompact HII regions (with sizes less than 0.1 pc and densities $> 10^4 \text{ cm}^{-3}$) and giant HII regions (sizes of the order of 100 pc, densities $< 30 \text{ cm}^{-3}$).

The combined effect of the strong stellar winds of massive stars and supernova explosions displaces the gas in the HII region and creates cavities of low density plasma around the stellar cluster which can reach a diameter of a few pc. Fig. 1.8 shows an example of this, observed with the Spitzer Space Telescope during the GLIMPSE project² (61) that is also a TeV gamma-ray source (58).

As the system evolves, HII regions can travel far away from their natal molecular clouds, and in some cases the association between the HII with its progenitor molecular cloud is not straightforward. In the case of OB associations, after the removal of gas and dust, the association is left unbound and expands, covering a wide range of spatial observations.

In a simplified picture, clusters of potential galactic cosmic ray sources may be therefore surrounded by low density plasma within the inner few pc from the core of the cluster, followed by an HII region. If cosmic-rays are generated inside the cavities created by the

²The GLIMPSE project is a mid-IR survey of the Galactic plane within the coordinates $-1^\circ < b < 1^\circ$, $-65^\circ < l < 65^\circ$

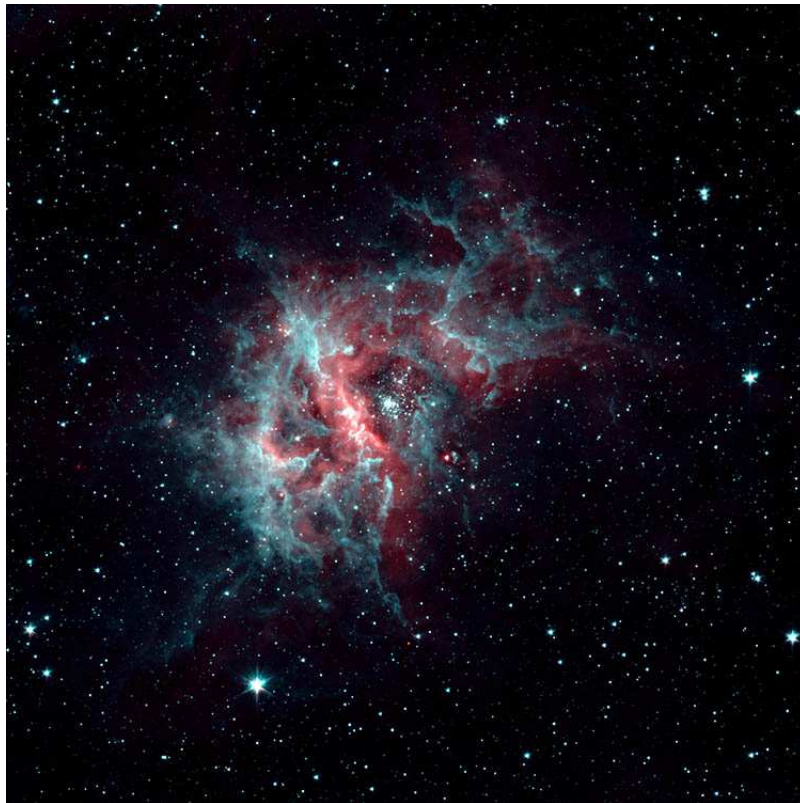


Figure 1.8: *The image shows the HII region RCW 49 with its ionizing cluster Westerlund 2 from the Spitzer Space Telescope. The color represent 3.6 Micron (Cyan), 4.5 Micron (Red). The stellar winds and radiation from Westerlund 2 have created a cavity in the dust inside a radius of $\sim 60''$ from the core of the stellar cluster (62). This source has been observed in HE gamma-rays by H.E.S.S. (58)*

strong stellar winds, protons can easily reach the gas in the HII region and interact with the free protons in that region (see table 1.2 for typical target particle densities). For young clusters, still embedded in their natal molecular clouds, the probability of interactions and hence the probability of neutrino production is even more favorable, due to the presence of additional target material. In our galaxy, the embedded-cluster phase last only $\sim 2-4$ Myr. Clusters with ages >5 Myr are rarely associated with molecular clouds (63), and the most of the embedded clusters which form in molecular clouds dissolve within ~ 10 Myr or less of their birth, when the injection of energy in the ISM from Sn explosion starts to dominate³.

³This is known as "infant mortality" of young and embedded star clusters.

Large-scale spatial distribution

Clustering of potential HE neutrino sources in massive star forming regions is particularly appealing for a neutrino telescope due to two main reasons:

- The possibility to integrate the emission from multiple sources increases significantly the minimum signal to noise required for a detection with respect to a single point source case (see chapter 4).
- Gamma-ray absorption in the environment of massive stars is very likely. If, on their way towards us, gamma-rays travel through the intense UV radiation field from OB and WR stars, they are very likely absorbed, whereas neutrinos can pass through. This leaves open the possibility of an enhanced neutrino emission with respect to the predictions from a simple gamma-neutrino connection without accounting for absorption.

In terms of source selection the discussion of the previous section favors:

- 1) The most massive stellar clusters or associations ($M_{clus} > 10^4 M_{\odot}$) with ages above ~ 1 Myr. These clusters harbor the most massive stars ($\sim 100 M_{\odot}$) (33), which evolve rapidly into WR.
- 2) Massive stellar clusters or associations ($M_{clus} > 10^3 M_{\odot}$) with ages above ~ 3 Myr. Clusters with a total mass $M_{clus} > 10^3 M_{\odot}$ can still contain very massive stars which evolve into WR, although their evolution takes place more slowly than for the most massive stars.

Note that due to the likely dissolution of most of the massive clusters their ages will be $\ll 40$ Myr, implying that most of them are in a powerful phase in which the energetics of the system is dominated by WR and core-collapse Sn.

The most massive clusters known ($M_{tot} > 10^4 M_{\odot}$) are listed in table 1.3 (see (64) and references therein). TeV gamma-ray emission has been detected in three out of four of the closest most massive clusters: Westerlund 1 (57), Westerlund 2 (58), and Cyg OB2 (125), providing evidence of particle acceleration up to TeV energies in these objects.

Given the limited sensitivity of the current neutrino telescopes, to restrict to a single cluster/association may not improve significantly the situation in terms of discovery with respect to the single point source case. In order to improve the chances of discovery, to study the large-scale distribution of potential sources and extend the search for clustering of events to even larger angular scales, can be an interesting alternative to search for extraterrestrial neutrinos.

Table 1.3. Galactic massive clusters ($> 10^4 M_\odot$).

Cluster	Lon [deg]	Lat [deg]	Distance [kpc]	Age [Myr]	Mass [$10^3 M_\odot$]
RSGC2	26.2	0.0	$5.8_{-0.8}^{+1.9}$	17 ± 3	40 ± 10
Westerlund1	339.5	-0.4	3.6 ± 0.2	3.6 ± 0.7	36 ± 22
RSGC1	25.3	-0.2	6.6 ± 0.9	12.0 ± 2.0	30 ± 10
RSGC3	29.2	-0.2	6 ± 1	18.0 ± 2.0	30 ± 10
Arches	0.1	0.0	7.62 ± 0.32	2.5 ± 0.5	~ 20
Quintuplet	0.2	-0.1	7.62 ± 0.32	4 ± 1	~ 20
GC central	0.0	0.0	7.62 ± 0.32	6.0 ± 2.0	~ 20
					$1,000 \pm 500$
NGC3603	291.6	-0.5	6.0 ± 0.8	< 2.5	13 ± 3
Trumpler14	287.4	-0.6	~ 2.8	3.25 ± 2.75	10 ± 1
Cyg OB2	80.2	0.8	~ 1.5	~ 2.5	~ 10
W49A	43.2	0.0	11.4 ± 1.2	1.2 ± 1.2	~ 10
Westerlund2	284.3	-0.3	~ 2.8	2.0 ± 0.3	> 7

The spatial distribution of young open clusters has traced the recent star formation in the Galaxy following the spiral structure of the galactic disk (66). From the perspective of an observer on Earth, the galactic disk is viewed edge-on. To the above mentioned clustering of potential cosmic ray sources due to the natural tendency of massive stars to form in associations, it is worth mentioning the agglomeration of potential sources in a relatively small patch of the sky due to

- 1) star-forming complexes associated to large segments of spiral arms which cover several degrees in the sky due to projection effects
- 2) our line of sight crossing several spiral arms

Whereas item (2) is more important towards the inner galaxy, item (1) can take place at any galactic longitude at which we are seeing a portion of one or more spiral arms. There are evidences of young open clusters complexes in the solar neighborhood associated to the underlying local spiral structure of the Galaxy (65). These are, in order of increasing distance: Orion, Scutum-Sagittarius, Cygnus, Scorpius and Cassiopeia-Perseus. These "clusters of clusters" of potential sources of high energy neutrinos may constitute an interesting way to look at the sky during the first years of performance of neutrino telescopes, when the sensitivities are still too low to expect a detection from single point sources. Of particular relevance for this work is the Cygnus complex, which appears in the

very high energy gamma-ray sky as a strong region of both diffuse emission and emission from sources (125).

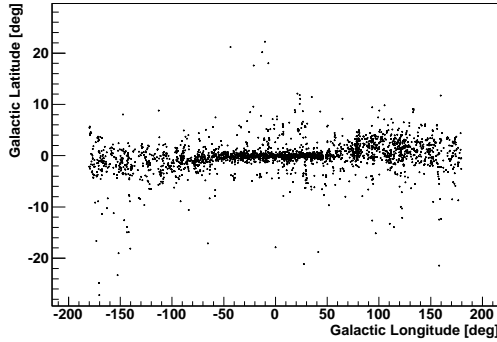


Figure 1.9: *Distribution of star forming regions in the galactic plane from the catalogue of Avedisova (67).*

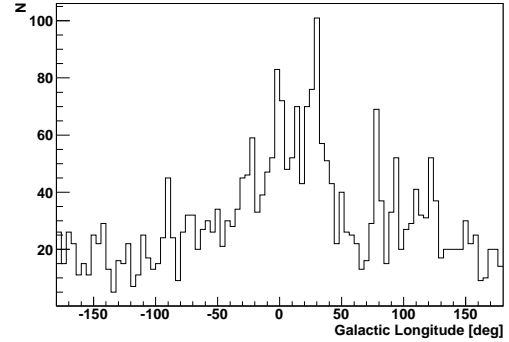


Figure 1.10: *Histogram of the distribution of star forming regions in galactic longitude from the catalogue of Avedisova (67).*

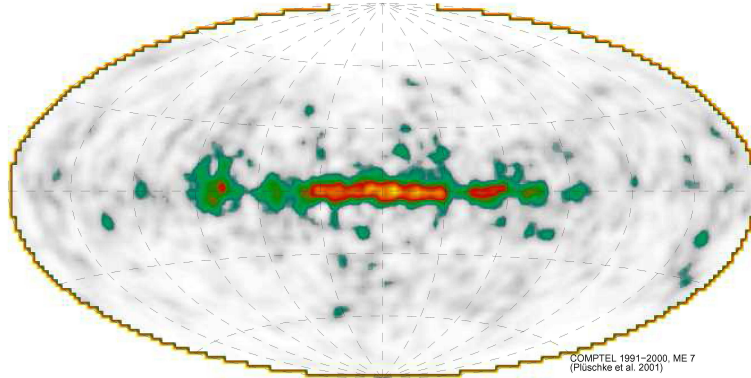


Figure 1.11: *COMPTEL skymap in the 1.809 MeV emission line from the decay of ^{26}Al (69).*

Figs. 1.9 and 1.10 show the distribution of star forming regions in the galactic plane and in galactic longitude, respectively, from the catalogue of Avedisova⁴ (2002) (67). There is a dense distribution of sources within the inner 50° in galactic longitudes, as well as a strong maximum towards $l \sim 80^\circ$, which is the direction along the Local spiral arm and points to the Cygnus region.

Regions of massive stars can be identified through the presence of elements synthesized by massive stars at their final stages of evolution (68). Up to now five isotopes have been

⁴The Avedisova catalogue includes observational data from ~ 3200 star forming regions between galactic latitudes $-5^\circ < b < 5^\circ$

detected by observations of the gamma-ray lines emitted from their disintegration. The long-lived ^{26}Al and ^{60}Fe (lifetime = 1.04×10^6 and 2.2×10^6 years, respectively) accumulate in the interstellar medium from successive supernova explosions. They are detected as diffuse emission in the galactic disk, its projection onto the galactic plane appearing as an excess towards the inner Galaxy as well as the Cygnus and Vela regions (see figure 1.11), (69), (70). The gamma-ray lines associated to the decay of ^{44}Ti , ^{56}Co , ^{57}Co (lifetime = 89, 0.31, 1.1 years, respectively) are associated with young SNRs, but so far only Cas A and SN1987A have shown the presence of these isotopes (71), (72).

A systematic survey of the inner galactic plane in VHE gamma-rays ($E > 100$ GeV) was conducted with HESS as a promising way to search for galactic VHE emitters. Fig. 1.12 shows the results of the H.E.S.S. galactic plane scan within galactic longitudes $0^\circ < l < 60^\circ$, $275^\circ < l < 360^\circ$ (17). Some of the gamma-ray sources have been associated with supernova remnants, some of them with pulsar wind nebulae, and the majority remain unidentified. The flat distribution of the galactic latitudes of the H.E.S.S. sources within 1° from the galactic plane indicates that they must be far away, typically a few kpc. At longitudes $30^\circ \lesssim l \lesssim 220^\circ$ the galactic plane has been surveyed with the Milagro detector, resulting in the discovery of a number of unidentified sources of TeV photons (see figure 1.13), three of which are located in the Cygnus region. In the Cygnus region the distribution of galactic latitudes of the Milagro sources is broader, which may suggest the presence of local TeV sources.

Some of the unidentified HESS sources have several positional counterparts and hence several different possible scenarios for the origin of the VHE gamma-ray emission. Concerning the hadronic or leptonic nature of the TeV gamma-rays, both scenarios are able to provide an adequate explanation of the data, leaving the origin of VHE gamma-rays still ambiguous. The morphology of the TeV emission observed from galactic sources is consistent with both point-like and extended. The morphology of a possible neutrino counterpart would follow exactly the gamma-ray profile only if all the gamma-rays are emitted through hadronic mechanisms and/or there is no significant gamma-ray absorption. In reality, where the observed gamma-ray pattern is likely to be a combination from both hadronic and leptonic processes, the morphology of a possible neutrino source may be very different from that of gamma-rays.

From the perspective of a neutrino telescope, the HESS and Milagro maps of the galactic plane provides fundamental input for an optimized search for clusters of high energy particles, either around a single point source (point-like clustering) or hot spot (showing some extension), or around a number of locations inside the same patch of the sky, due to either the natural tendency of particle accelerators to form in associations or due to projection effects, or both.

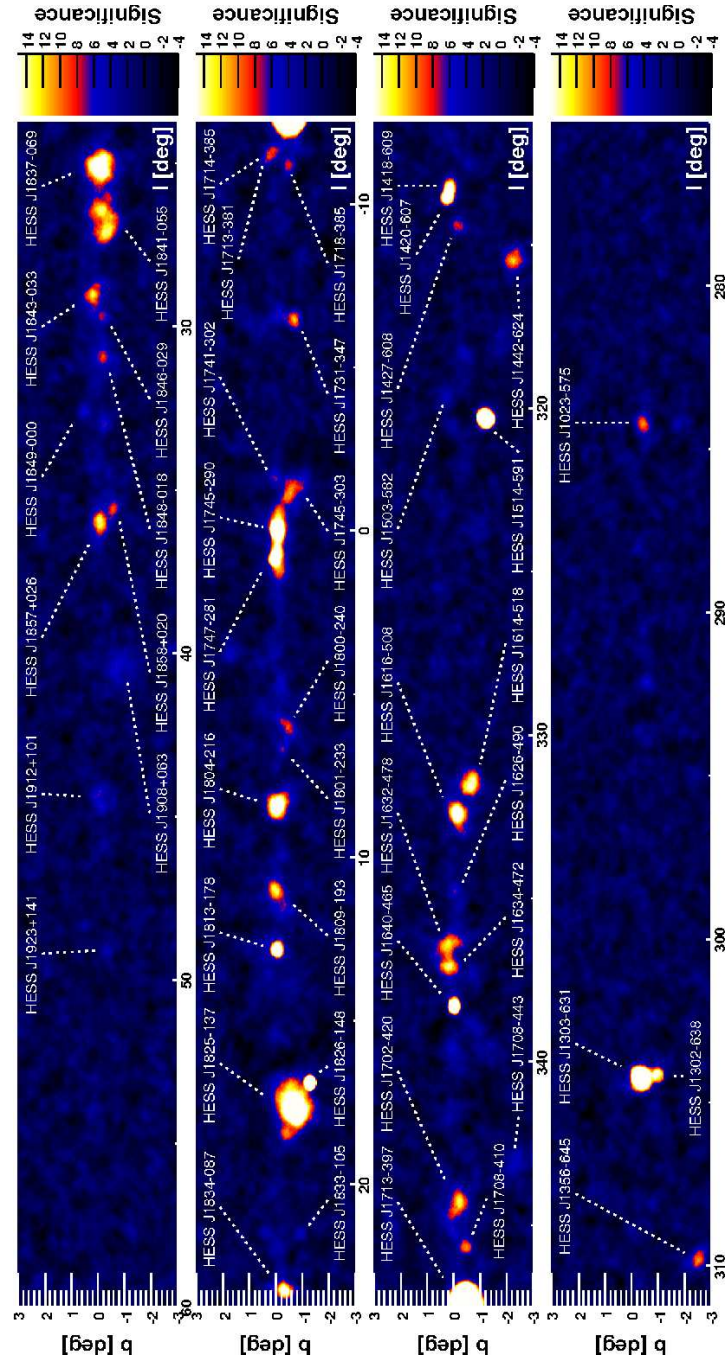


Figure 1.12: Image showing the pre-trials statistical significance in the HESS Galactic Plane Survey region. Image taken from (17).

1.2.2 Supernova remnants and pulsar wind nebulae

Supernovae play a critical role in high energy astrophysics. On the stellar scale they are the most energetic objects known, with emission detected in a wide range of wavelengths.

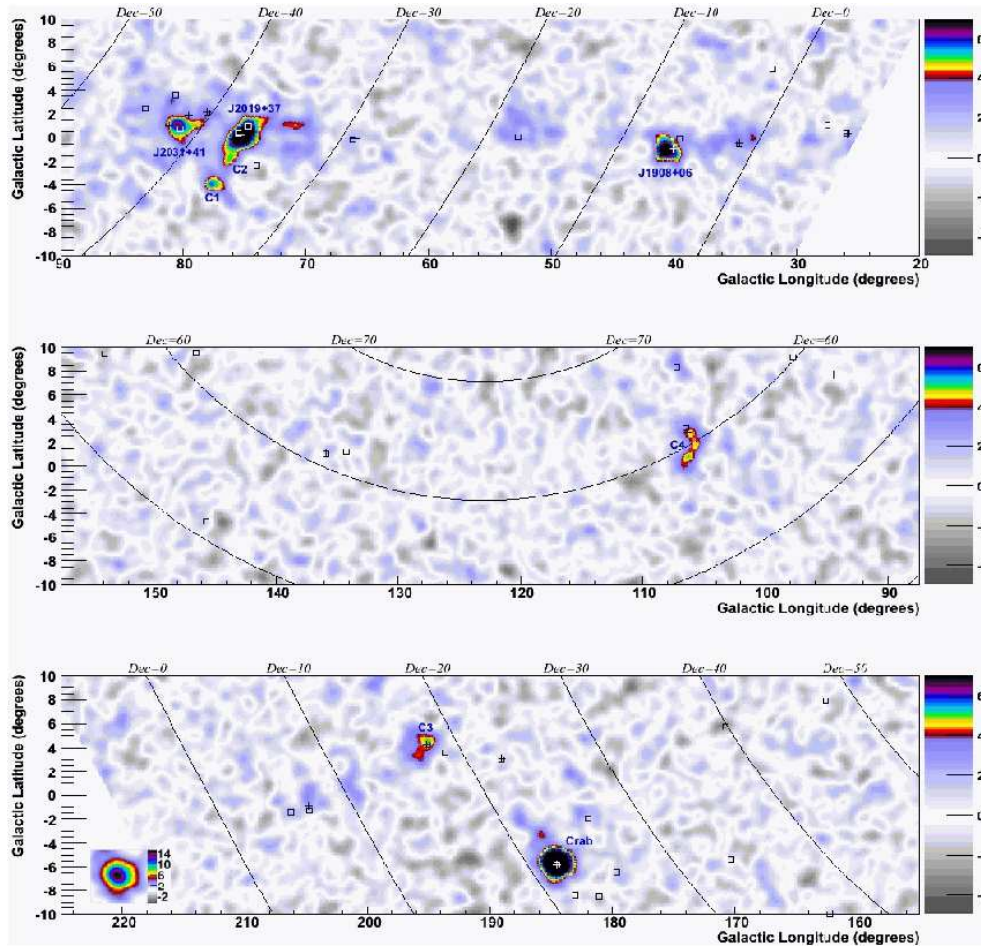


Figure 1.13: *Pre-trial statistical significance map of the Galactic plane surveyed by Milagro (18).*

Gamma-rays resulting from supernova explosions may be detectable either in the first few seconds of the explosion as a gamma-ray burst (assuming a GRB-Sn connection), or as the steady and periodic emission from the pulsar (PSR), the rotating core of the exploded star, or as the expanding outer shell known as the supernova remnant (SNR).

The most common type of SNR is characterized by the shell of interstellar material swept up by the expanding shock wave which is visible in X-rays. These are Shell-type SNRs, like Cassiopeia A.

A SNR with a PSR in its center which fills the remnant with relativistic particles is called a plerion or a pulsar wind nebula (PWN), due to the nebulosity formed because of the synchrotron emission of the relativistic electrons or the interaction of the relativistic PSR wind with its surroundings. The emission spectrum around the PSR can range from radio to X-rays and gamma-ray wavelengths. The most famous object of this type is the Crab

nebula, one of the brightest gamma-ray sources in our galaxy.

There are SNRs which have both shells and plerions and are called composite SNRs. In these objects, there is a small plerion centered in the PSR left behind the expanding shock wave as well as a detectable shell. The Vela SNR is an example of this.

The believed mechanism responsible for particle acceleration in SNR is in the shock waves caused by the outburst that may persist for thousands of years after the Sn explosion, losing progressively its power. The shock waves produced by the initial explosion propagate into the ISM and they can be observed as the expanding shells of SNRs, giving rise to a variety of observational effects seen in old remnants: hot plasma, radiating in X-rays; wisps of optical nebulosity, representing cooling regions heated by the passage of shock waves through dense clouds; infrared emission due to shock heated dust; synchrotron emission from radio to X-rays due to relativistic electrons in a magnetic field; and in some cases gamma-ray emission due to either inverse Compton of relativistic electrons on the ambient photon field or to the decay of neutral pions produced in hadronic interactions, or a contribution of both processes.

Of all the parameters of the supernova explosion, two are particularly important: the initial kinetic energy of the ejecta, and the presence or absence of a pulsar (PSR), which will inject relativistic particles and a magnetic field. A PSR, if present, will exert a significant influence around the first $10^3 - 10^4$ years providing an additional source of energy. The fraction of kinetic energy from the shock or the spin down luminosity of a PSR that is efficiently converted into high energy protons or ions is a matter of debate and probably depends on the system.

The recent detections of TeV gamma-rays from several SNRs have contributed to the picture of galactic cosmic rays accelerated in these objects. However, the proof that the gamma-rays observed are indeed produced by cosmic rays is still missing, since both leptonic and hadronic models can be adapted in order to fit the observed spectrum. Confirmation that SNRs are efficient cosmic rays accelerators can come from the detection of high energy neutrinos.

The properties of the observed remnant are determined by the dynamics of the relativistic plasma cloud; i.e., by its interaction with the ISM. The environment of a supernova is therefore of critical importance for the contribution of the different processes which give rise to the observed emission at multiple wavelengths in SNR and PWN. In what concerns the VHE emission, an hadronic nature of this will be more likely in objects within or near molecular clouds or embedded in dense HII regions (see tables 1.1. Molecular clouds are traced with CO and H₂ emission and their typical molecular densities are in the range $10^2 - 10^3 \text{ cm}^{-3}$ with the densest molecular cores being able to reach $\sim 10^4 - 10^5 \text{ cm}^{-3}$, 1.2), while typical densities of the ISM are $\sim 1 \text{ cm}^{-3}$. Such dense environments require less proton

luminosity for an efficient production of neutrinos with respect to the one needed in low density environments.

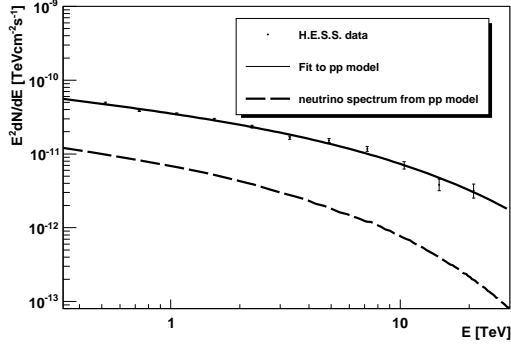


Figure 1.14: *Spectrum of the Crab measured by H.E.S.S. fitted to a model of pp interactions and associated neutrino spectrum.*

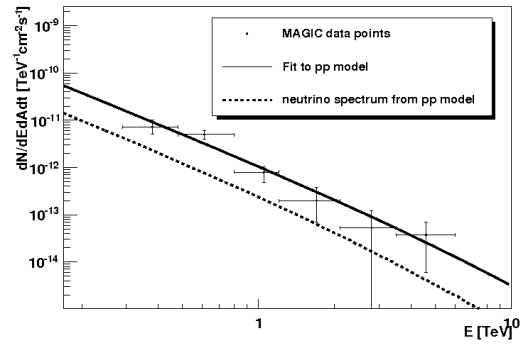


Figure 1.15: *Spectrum of Cas A measured by MAGIC fitted to a model of pp interactions and associated neutrino spectrum.*

Although the origin of the gamma-rays detected from SNRs is ambiguous, they provide an upper limit to the neutrino production. Under the assumption of a hadronic origin of gamma-rays, it is possible to find an estimation of the maximum number of neutrinos expected from the same process, provided that the medium is transparent to gamma-rays. Fig. 1.14 and Fig. 1.15 show the gamma-ray spectrum of the Crab PWN, and Cas A, a shell-type SNR. The gamma-ray spectrum is fitted to a model of pp interactions following the parametrizations of (23) (see section 1.1.2), and the associated neutrino spectra is extracted from this fit. The sources selected are considered as representative of different type of spectra:

- Crab: very bright in gamma-rays, but with a steep gamma-ray spectrum $\propto E^{-2.4}$ and an energy cutoff at 14.3 TeV (9). An alternative scenario for this source comes from the measurements of the High Energy Gamma-Ray Astronomy (HEGRA) experiment, which seem to indicate a steeper spectrum up to 80 TeV, following $\propto E^{-2.6}$.
- Cas A: relatively faint and with a steep spectra following $\propto E^{-2.4}$, but with no cutoff observed up to 5 TeV (10).

The obtained neutrino fluxes under the hadronic interpretation of the gamma-ray spectrum are well below the expected range of detection of IceCube after one year of operation, and several years of data taking will be required in order to put some constraints to the hadronic or leptonic nature of the observed gamma-rays. Fig. 1.16 shows the obtained upper limits to the neutrino spectrum for the Crab and Cas A together with the expected sensitivity to E^{-2} and E^{-3} spectra of the full IceCube detector IC80 after one year of operation (5). The sensitivity to an E^{-3} spectrum is obtained assuming that the improvement achieved

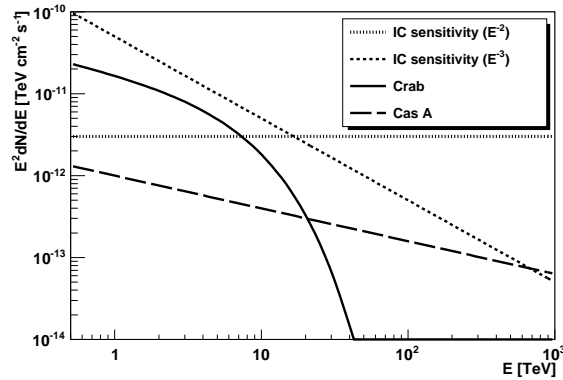


Figure 1.16: *Upper limit on the neutrino emission from the Crab and CasA from gamma-ray observations. The sensitivity of IceCube after one year of operation is shown for two different source spectra, E^{-2} and E^{-3} .*

with IC80 with respect to IC22 is the same for an E^{-2} than for an E^{-3} , which is a reasonable approach. Fig. 1.16 illustrates perfectly why the E^{-2} , no cutoff up to 1 PeV, is not a convenient approach to optimize data analysis which desire to observe these sources. These analysis are sensitive for energies above a few TeV, a range at which the emission of Crab-like sources starts to drop significantly. The contribution in the detector of events with energies above the source energy cutoff is minimal. As a consequence, even for bright sources, as the case of the Crab, the bulk of the emission is lost and the sensitivity and hence the exposure time required to see these type of sources increases considerably with respect to the one calculated under the E^{-2} , no cutoff approach. It is important to note that, even when the spectrum of Cas A extends up to 1 PeV without a cutoff in Fig. 1.16, only measurements up to 5 TeV are available, thus the source can show an energy cutoff well below 1 PeV. Once neutrino telescopes reach a level of sensitivity comparable to the upper limits in the neutrino emission from gamma-rays, either a neutrino detection or a non-detection could give some clues about the contribution of the hadronic component to the observed gamma-rays, providing significant constraints on the theory of cosmic ray production in SNRs and on the physics of SNRs.

1.2.3 High Mass X-ray Binaries and Microquasars

X-ray binaries (XRBs) are binary systems composed by a compact object (CO), either a neutron star or a black hole, and a non-degenerate star. According to the stellar companion they can be classified in:

- High Mass X-ray Binaries (HMXBs): the companion star is a type O, B star, which present strong stellar winds and intense UV radiation.

- Low Mass X-ray Binaries (LMXBs): the companion star is a low or intermediate mass star, with less mass than the CO.

I consider HMXBs a more promising candidates for neutrino emission, provided that protons are accelerated in the system, since they present a more suitable environment for pp interactions than LMXBs, due to the high densities expected in the surroundings of OB stars from the stellar winds. Even though LMXBs can be in some cases as powerful as HMXBs in terms of mechanical energy injected into the ISM, and thus they might be also sources of cosmic-rays, I consider that in LMXBs the companion star does not provide enough target for an efficient production of gamma-rays and neutrinos. As a result, neutrino emission at the binary system scales is unlikely to be detected and LMXBs are not included in the following discussion.

Two are the mechanism that can power HMXBs (76):

- 1) **Rotation.** A young spinning-down pulsar is losing its rotational energy in the form of a relativistic wind. The shocks between the PSR wind and the wind of the companion star can accelerate both electrons and protons giving rise to non-thermal emission from radio to TeV gamma-rays from their interactions with the matter, radiation and magnetic field of the system.
- 2) **Accretion.** The compact object is accreting matter from its companion star through strong stellar winds. Some of these sources present non-thermal radio emission thought to be synchrotron radiation produced by relativistic electrons in a jet that is somehow ejected from the surroundings of the compact object (77), (78). Once the existence of a jet has been established the XRB is called a microquasar (79). Microquasars (μ QSOs) show a high variety of X-ray spectral states associated with different accretion states, and at the same time associated with the presence or absence of the radio jets (80), (81). In microquasars, particle acceleration may take place directly inside and along the jet, out to parsec-scale distances (binary system scale), or additionally at the jet termination regions due to interaction with ambient matter⁵ (82), (83).

Population

In our galaxy, there are 114 HMXBs catalogued based on their X-ray properties (84) as well as 16 additional Compton thick HMXBs discovered by the INTEGRAL observatory (85). Most of the HMXB population consist of a highly magnetized neutron star in orbit around a Be type star. The neutrons star is accreting matter from the stellar wind of its companion

⁵In this last case, also LMXBs could be responsible for the emission of gamma-rays and neutrinos from pp interactions if the ambient matter is sufficiently dense.

star. The high magnetized neutron stars are believed to be incapable of generating jets. Even though very high energy gamma-rays and neutrinos have been suggested (86) as a result of the interactions of particles accelerated in the magnetosphere gaps of the NS with thermal particles from the accretion disk, I do not consider these type of sources as good candidate sources of neutrino emission.

Only HMXBs which have associated radio synchrotron emission have evidence of the presence of accelerated particles in the system. These are shown in table 1.4.

Table 1.4: Microquasars and rotation-powered HMXBs detected in the Galaxy with associated radion synchrotron emission.

Source	Type	Star	Compact object	P_{orb} (d)	D (kpc)
LS I+61 303	μ QSO?	BVe	NS?	26.5	2
Cygnus X-1	μ QSO	O9.7Iab	BH	5.6	2.5
Cygnus X-3	μ QSO	WNe	BH?	0.2	7
SS 433	μ QSO	evolved A?	BH?	13.1	4.8
LS 5039	μ QSO?	O6.5V	?	4.1	2.9
V4641 Sgr	μ QSO	B9III	BH	2.8	10
PSR B1259-63	binary pulsar	Be	NS	1241	1.5

Gamma-rays and neutrinos in HMXBs

The MAGIC and H.E.S.S. detections of four HMXBs have provided evidence of the existence of multi-TeV particles either in the jets of microquasars or in the colliding wind region between the PSR and the companion star. There are five gamma-ray binaries known so far, two of them are still to be confirmed as rotation-powered or accretion-powered (87):

- **PSR B1259 – 63.** A rotation-powered binary system consisting of a 48ms pulsar, with a spin-down luminosity of $L = 8.3 \times 10^{35}$ erg/s, in orbit around a Be star. The system has a highly eccentric orbit and an orbital period of 3.4 years. H.E.S.S. detected TeV emission around periastron, when the pulsar is $\sim 10^{13}$ cm from the companion star (88). The time-averaged gamma-ray spectrum observed follows $F(E > 380 \text{ GeV}) \approx 1.3 \times 10^{-12} E^{-2.7} \text{ TeV}^{-1} \text{ cm}^{-2} \text{ s}^{-1}$.
- **LS 5039.** HMXB composed by a compact object in an eccentric 3.9 days orbit around a O6.5V star. The nature of the compact object is not clearly established and both, a microquasar model and a model based on acceleration in shocks produced by the interaction of a pulsar wind with the wind of the companion star have been suggested.

H.E.S.S. detected VHE gamma-rays from this source modulated with the orbital period, suggesting gamma-ray production at binary system scales accompanied to gamma-ray absorption via pair production with the stellar photons (89), (74).

- **LS I + 61 303.** HMXB in a eccentric orbit around a Be star. The nature of the compact object is not known and both pulsar wind model and microquasar model have been suggested for this source as well. MAGIC detected VHE emission from this source modulated with the orbital period (90). The highest significant detection is obtained around apastron, at orbital phases 0.6-0.7, with a flux described by $F(E>300 \text{ GeV}) \approx 2.6 \times 10^{-12} E^{-2.6} \text{ TeV}^{-1} \text{ cm}^{-2} \text{ s}^{-1}$. No TeV emission is observed at periastron. Significant gamma-ray absorption is also expected in this case (91), especially near periastron, where the two stars are closer.
- **Cygnus X – 1.** High mass microquasar in a 3.9 days orbit around a O type star. MAGIC detected VHE gamma-rays in coincidence with a hardening of the X-ray flux (92). No modulation with the orbital period has been found and it is likely that the gamma-ray radiation comes from the interaction of the jet out of the binary system scales.
- **Cygnus X – 3.** A microquasar formed by a Wolf Rayet star and a compact object which is thought to be a BH. After numerous attempts to observe this source in TeV gamma-rays, it remains undetected at these energies. It was detected by Fermi LAT (93) showing a very steep spectrum.

Both hadronic (94), (95), (96) and leptonic (97), (98) models have been proposed to describe the multiwavelength behaviour of these systems, either in the microquasar scenario or in the rotation-powered scenario. In the hadronic models hadrons dominate the radiative output at GeV-TeV gamma-rays, producing neutrinos in the process, and leaving electrons as possible significant emitters only at lower energies. Leptonic models extends the energy of leptons from synchrotron radio emission to VHE gamma-rays produced by inverse Compton.

Possible neutrino emission from gamma-ray binaries has been discussed in the literature (102), (99), (100), (101), (102), covering a large range of possible fluxes and scenarios, due to the multiple uncertainties present in the calculations. The link between TeV gamma-rays and neutrinos in HMXBs can not be established in such a simple way as presented in the previous section. In this case, significant absorption of TeV gamma-rays is expected in the strong radiation field of the companion star, but not of neutrinos (74), (75). As a consequence, gamma-ray observations do not constraint a possible flux in neutrinos, and considerations about gamma-ray opacity have to be included in the discussion. The calculations of the optical depth for gamma-rays above 100 GeV in the environment of a massive star found in the literature yield values large enough for developing the e^\pm pair cascade in the radiation field of the massive star (74), (75), (103). Computation of the

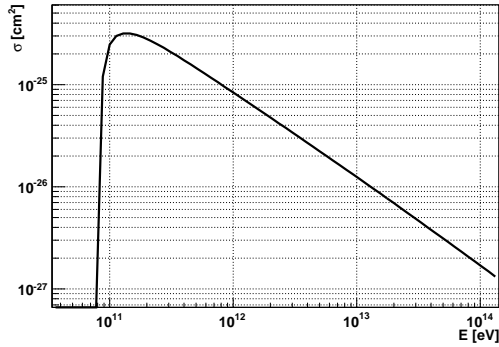


Figure 1.17: *Cross section for pair production of a gamma-ray photon of energy E with photons of energy 3 eV (UV).*

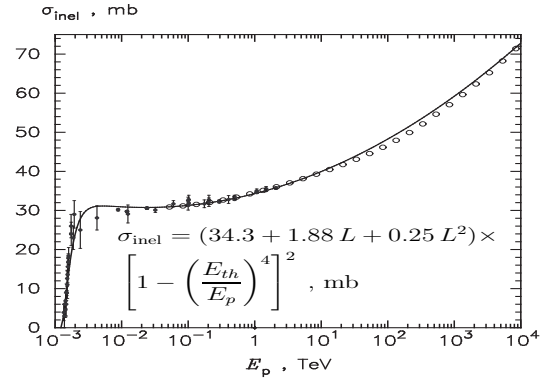


Figure 1.18: *Cross section for pp interactions from (23). $1 \text{ mb} = 10^{-27} \text{ cm}^2$*

de-absorbed gamma-ray spectrum above 100 GeV would require detailed treatment of the cascade that develops, since the interactions of secondary e^\pm pairs may also give rise to gamma-rays.

Fig. 1.17 shows the cross section for pair production of a gamma-ray photon of energy E with an UV photon of energy 3 eV from equation 1.25. Fig. 1.18 shows the cross section for pp interactions from (23) for comparison. The two processes have similar probabilities, meaning that if neutrinos and gamma-rays are produced via pp interactions, it is very likely that gamma-rays are absorbed, provided that they travel through a dense UV radiation field.

Chapter 2

The IceCube neutrino observatory

During the decade of the 80s, the neutrino detection based on the Cherenkov technique was already implemented in instruments such as Super-Kamiokande, and efforts to develop instrumentation for a most sensitive neutrino detector at higher energies were already underway. However, there was not yet an efficient way for the creation of the neutrino telescopes with the effective area required for astrophysical observations.

The exceptionally large size of the instrumented volume needed in a high energy neutrino observatory requires to use large natural reservoirs of water or clear ice. By the late 80's the Deep Underwater Muon and Neutrino Detection Project (DUMAND) was the first to construct a prototype string of photodetectors at 4800 m depth in the Pacific Ocean (104); however, out of the nine strings planned, only one was ever deployed and the project was finally cancelled. By the same time, the possibility of using the thick Antarctic ice sheet as deep underground detector of high energy neutrinos was being explored (105), (106). Experiments began at South Pole in 1991-92, which resulted in the first detector using ice as the medium for a Cherenkov telescope: the Antarctic Muon and Neutrino Detector Array (AMANDA), in 1997 (107).

In 1993, the Baikal group proved successful the Cherenkov technique for the detection of high energy neutrinos with a detector array deployed in the lake Baikal in Siberia (108). In 1999, the Antares detector started operations in the Mediterranean sea (109). Although both water and ice have been proved as suitable media for the construction of neutrino telescopes, there are several advantages when working in the extraordinarily clear ice of the South Pole, like the long photon absorption length, the installation over solid surface, and the availability of the South Pole station support. It was precisely the success of the AMANDA detector that allowed the construction of its successor, the IceCube neutrino observatory, the first, eagerly awaited 1 km^3 neutrino telescope.

2.1 Detection principle

The physics of the high energy neutrino detection are based on the physics of their interaction. Neutrinos only interact weakly, and large detector volumes and exposure times are required to observe a significant number of neutrino interactions. This section summarizes the basic physical aspects involved in the detection of neutrinos.

2.1.1 Neutrino interactions

Neutrinos can interact with nucleons through two types of processes:

- The charged-current (CC) interaction: $\nu_\ell (\bar{\nu}_\ell) + N \longrightarrow \ell^- (\ell^+) + X$, involving the exchange of a charged W boson.
- The neutral-current (NC) interaction: $\nu_\ell (\bar{\nu}_\ell) + N \longrightarrow \nu'_\ell (\bar{\nu}'_\ell) + X$, through the exchange of a neutral Z boson.

where ℓ is the lepton flavour (muon, electron or tau), N is a nucleon, and X represents an hadronic shower.

The muon neutrino, ν_μ , is the easiest to detect and also the most suitable for neutrino astronomy. The produced muons carry half of the energy of the parent neutrino, and hence they have great penetrating power. As a consequence, they travel several kilometers through matter, leaving clear signatures of its track through the detector. The long muon range enlarges the effective volume of a neutrino telescope for muon neutrinos, observing also muons produced far outside the detector volume. Muon neutrinos can also pinpoint the neutrino sources since they preserve the direction of the parent neutrino. The mean angular deviation of the muon with respect to its parent neutrino is $\Phi = 0.7 (E_\nu / TeV)^{-0.7}$ deg. Therefore, in the energy range in which 1 km³ neutrino telescopes operate, the muon direction is a very good approximation of the neutrino direction.

CC interactions of ν_e and ν_τ produce electrons and taus, respectively. In the case of ν_e interactions, the process is accompanied of an electromagnetic shower with a typical length of only a few meters. This limits the detection of electron neutrinos to interactions inside or close to the detector. In the case of ν_τ an hadronic shower is produced. The generated τ has a lifetime of only 2.91×10^{-13} s; the main modes its decay are (110): $\tau \rightarrow \nu_\tau + X$ (64.8%), $\tau \rightarrow \nu_\tau \bar{\nu}_e e^-$ (17.85%), $\tau \rightarrow \nu_\tau \bar{\nu}_\mu \mu^-$ (17.36%). The first channel, with a branching ratio of 64.8% involves the creation of an hadronic shower. This effect has been predicted to leave a "double-bang" signature in the detector, caused by the first hadronic shower from the initial ν_τ interaction, followed by the track of the τ , and then a second cascade from the

τ decay (111). At energies greater than 1 PeV, the cascade and the neutrino interaction vertex are separated by several tens of meters connected by the τ track.

The observation of ν_e and ν_τ requires the reconstruction of cascade events in the detector, and there is no possibility to pinpoint the location of their sources of origin. Since this work focuses on the discovery of astrophysical sources of high energy neutrinos, I will only consider the detection of ν_μ based on the reconstruction of the secondary muon track when propagating through the detector.

2.1.2 Cherenkov radiation

A charged particle moving through a medium faster than the speed of light in that medium emits Cherenkov radiation along its path. Since the Cherenkov photons move slower than the charged particle, they propagate under a characteristic angle with respect to the direction of motion of the charged particle, resulting in a cone of light called the Cherenkov cone. The angle of the Cherenkov cone is related to the velocity of the particle, $\beta = v/c$, and to the refractive index of the medium, n , according to

$$\cos \theta_c = \frac{1}{n\beta} \quad (2.1)$$

The spectrum of Cherenkov photons emitted by a particle with unit charge per unit track length is

$$\frac{d^2 N_\gamma}{dx d\lambda} = \frac{2\pi\alpha}{\lambda^2} \left(1 - \frac{1}{\beta^2 n^2} \right) \quad (2.2)$$

where α is the fine-structure constant and λ the wavelength of the emitted photon. The threshold for Cherenkov radiation, corresponding to the minimum velocity of the charged particle at which it can emit Cherenkov radiation is

$$\beta = \frac{1}{n} \quad (2.3)$$

For muons moving through ice, for which $n_{ice} \approx 1.33$, only those with $v > 0.75c$ emit Cherenkov radiation. The emission occurs predominately in the UV part of the electromagnetic spectrum, which is detected by the array of phototubes which form the IceCube detector.

2.1.3 Signal and background in IceCube

Two different types of muon-like events trigger the IceCube detector:

- **Events produced by muon neutrinos.** As explained in section 2.1.1, the interaction of a high energy muon neutrino produces a muon which travels through the detector emitting cherenkov radiation which can be recorded by optical sensors. The neutrino signal in the detector has at the same time two different contributions: neutrinos generated by the decay of charged pions produced in interactions of cosmic-rays in the atmosphere (see Fig. 2.1), and neutrinos from astrophysical sources.
- **Events produced by atmospheric muons.** High energy muons are also generated in the interactions of cosmic-rays with the nuclei in the atmosphere (see Fig. 2.1). They represent 10^6 times more events than neutrino induced events, and constitute the main source of background in IceCube.

The IceCube detector is located 1km below the ice sheet of the South Pole. Muons produced by cosmic-rays in the atmosphere are able to travel only a few km through the Earth; as a consequence they can only reach the detector from above, travelling through the detector from the top to the bottom, i.e., in a downwards direction. In order to get rid of this background, IceCube uses the fact that only neutrinos can travel through the Earth and reach the detector from below. Neutrino induced events are therefore characterized by an upwards direction. All the events reconstructed as down-going are eliminated from the sample, whereas the events reconstructed as up-going are kept as candidate neutrino events. As a consequence, the field of view of the IceCube detector is restricted to the northern hemisphere¹.

Data analyses based on astrophysical purposes have to deal with the background of atmospheric neutrinos after the suppression of the atmospheric muon background. In the atmosphere, only low energy pions decay and produce neutrinos, whereas at high energies pions mainly scatter. As a consequence, the neutrino flux produced by cosmic-rays in the atmosphere has a steep energy spectrum, following $E^{-3.7}$ (see Fig. 2.2 from (4)). The neutrino flux from astrophysical sources is expected to be a much harder function of energy than the atmospheric neutrino flux, extending to energies well above a few TeV and therefore opening the possibility to perform high energy neutrino astronomy.

2.2 The detection medium: the ice at the South Pole

An accurate reconstruction of the muon tracks requires detailed description of the propagation of the Cherenkov photons through the detector until they reach the optical sensors. The glacial ice is the most transparent solid medium known at the considered wavelengths

¹IceCube analysis which extends to the southern hemisphere correspond to neutrino energies above a few PeV and are not considered in this work. For more information about these type of analysis see (114).

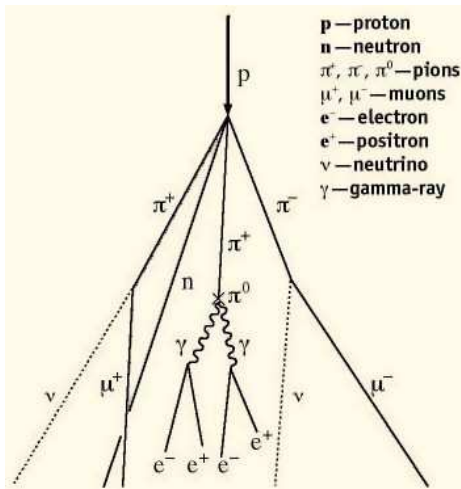


Figure 2.1: *Cosmic-ray interaction in the atmosphere and development of the cosmic-ray shower.*

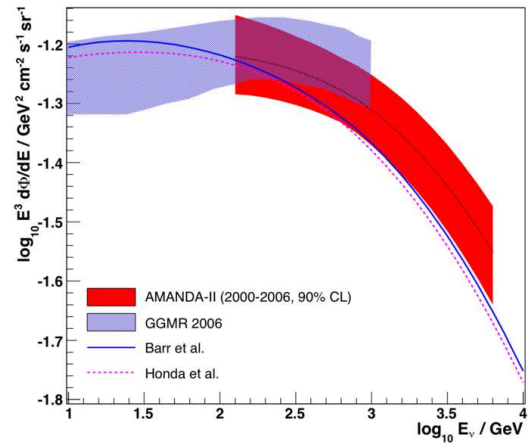


Figure 2.2: *Atmospheric neutrino flux (4)*

(200-400 nm), making it ideal for the detection of Cherenkov photons. However, even under such favorable conditions, it is very likely that the photosensors record light that has been scattered several times. The scattering and absorption of light in the ice has to be quantified in order to include such information into the simulations and the reconstructions algorithms.

The different geological and atmospheric conditions at the South Pole over the history resulted in different layers of dust generated at the surface. Nowadays, these layers are buried deep inside the glacial ice, and manifest themselves as an increase in optical scattering and absorption of photons. The optical properties of the ice have been measured with the AMANDA detector using artificial light sources. Four dust layers have been identified in South Pole ice studying AMANDA scattering data and ice core data (112). The dust layers are labeled A,B,C and D in Fig. 2.3.

Fig. 2.4 shows the optical properties of the South Pole from (112). More detailed measurements of the optical properties of the ice at the South Pole are ongoing during IceCube installation, allowing to refine the ice model

2.3 The IceCube detector

The IceCube detector is in construction at the South Pole since 2004. When completed, in 2011, it will consist of 86 total strings of optical sensors. Different subdetectors make up

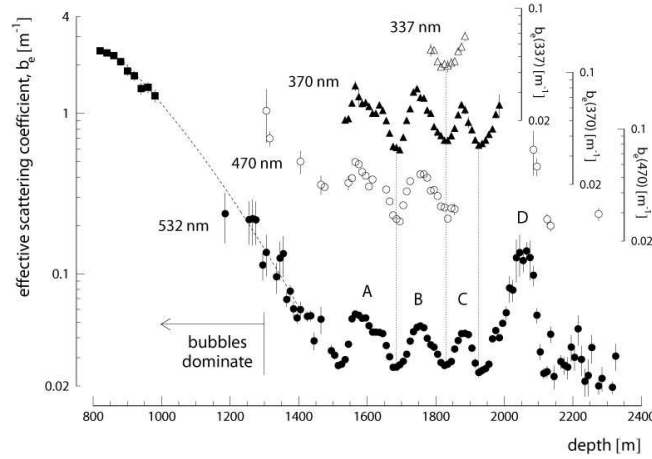


Figure 2.3: *Depth dependency of the effective scattering coefficient of photons of three different wavelengths: $\lambda = 337, 370$ and 470 nm. Taken from (112)*

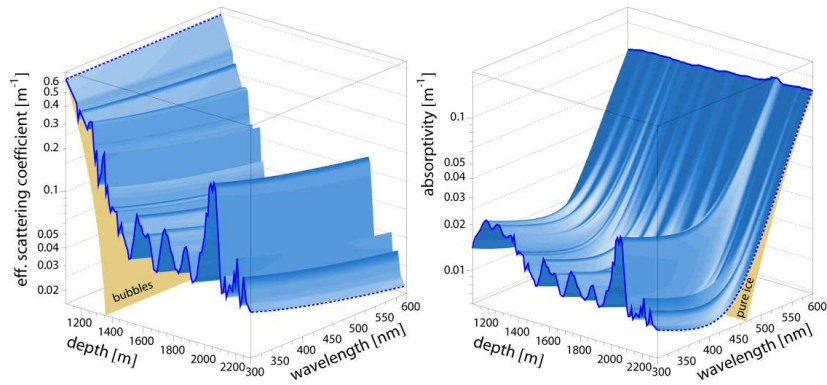


Figure 2.4: **Left** : *Depth and wavelength dependence of the scattering. Scattering traces dust concentration below ~ 1350 m and becomes increasingly dominated by bubbles at shallower depths. Bubbles dominate ($\sim 90\%$) scattering at 1100 m and rapidly falls with depth. Scattering due to bubbles has no wavelength dependence. Below ~ 1350 m scattering is dominated by dust. At these depths, the bubbles have been reduced to a minimum size of a few tens of microns before converting to non-scattering air hydrates.* **Right** : *Absorption traces dust concentration below 500 nm and becomes dominated by the ice at longer wavelengths. Figures taken from (112)*

the IceCube system: the InIce array, the AMANDA detector, DeepCore and IceTop. The main properties and operation of each of these detectors are explained below.

Figure 2.6 shows a schematic view of the IceCube array. Embedded in the IceCube instrumented volume is the subdetector AMANDA, which was taking data from 1997 up to 2009. In the center of the array is the counting house, the IceCube laboratory which holds

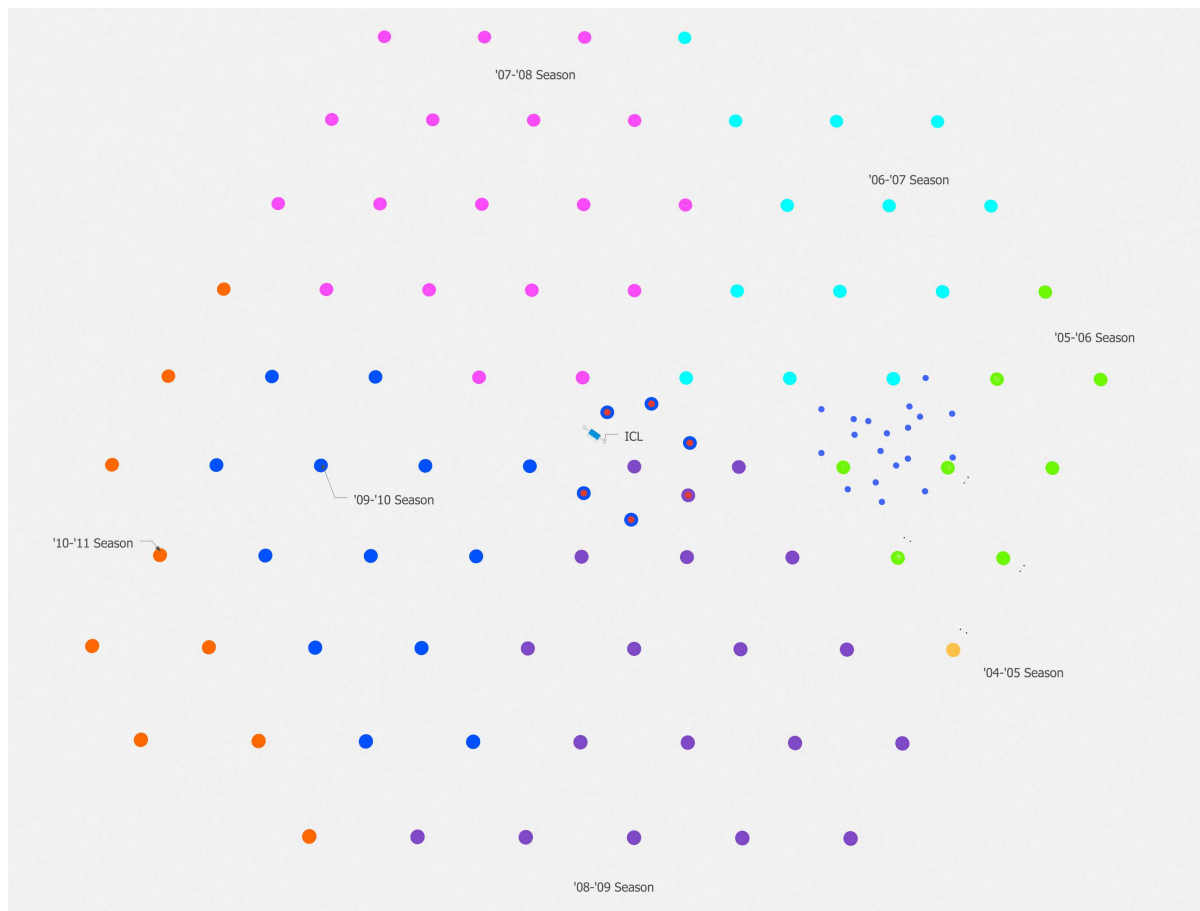


Figure 2.5: *Map of the locations of IceCube strings at each season.*

the surface electronics.

The in-ice array

This is the main, 80 strings detector. The strings are spaced by 125 m over an area of approximately 1 km², in a hexagonal array configuration with the optical sensors placed at depths between 1.4 km and 2.4 km from the surface.

AMANDA

The AMANDA detector, the predecessor of IceCube, consists of 677 optical modules (OMs) deployed in 19 strings during the years 1995-2000. The array has 200 m diameter and 500 m height and is located at depths between 1500 m and 2000 m from the surface.

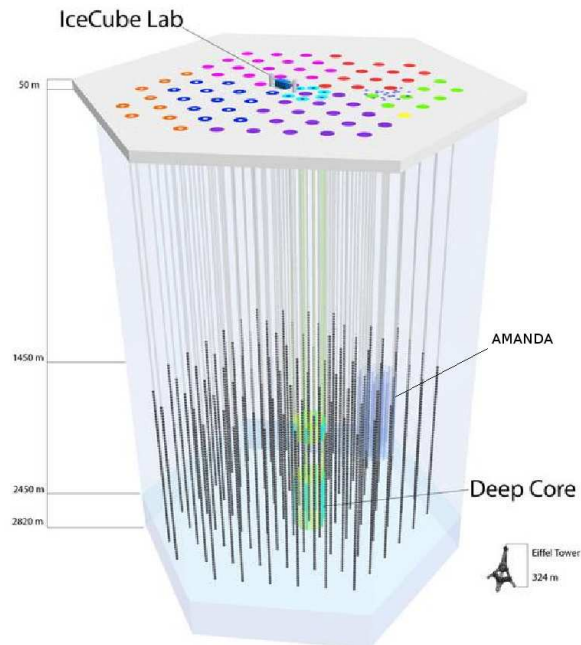


Figure 2.6: *Schematic picture of the IceCube detector.*

Its location inside IceCube is illustrated in figure 2.6. During the 2006-2007 deployment season, AMANDA was fully integrated into IceCube and joint IceCube/AMANDA events have been acquired since then.

IceTop

The IceTop surface array is located in the surface, above the IceCube strings. When completed, it will consist in a complex with 160 ice Cherenkov tanks which provides a detector for cosmic rays, and is also used for calibration.

DeepCore

DeepCore is an array of 5 extra strings that will be deployed in the center of the InIce array. The main role of DeepCore is to provide a better performance of IceCube at energies below 1 TeV.

2.4 Data Acquisition

The goal of the data acquisition (DAQ) in IceCube is to produce a list of events and their characteristics. This process has two different parts: one refers to the physical components which capture the information from the Cherenkov photons, and how that information is processed and transmitted to the surface. The other part deals with the construction of the events as single entities from a list of optical sensor readouts.

2.4.1 The Digital Optical Module (DOM)

The main task of the IceCube DAQ is to capture and timestamp with high accuracy the signals induced by physical processes. The fundamental element in this process is the Digital Optical Module (DOM), the IceCube optical sensor which contains a downward-facing Hamamatsu R7081-02 photomultiplier tube (PMT) and associated electronics in a 35 cm diameter pressure sphere (113). To avoid attenuation and dispersion of the PMT signal during the transmission and preserve the quality of the recorded PMT pulses, an immediate conversion to a digital format is done individually inside each DOM. A scheme of an IceCube DOM is shown in Fig. 2.7

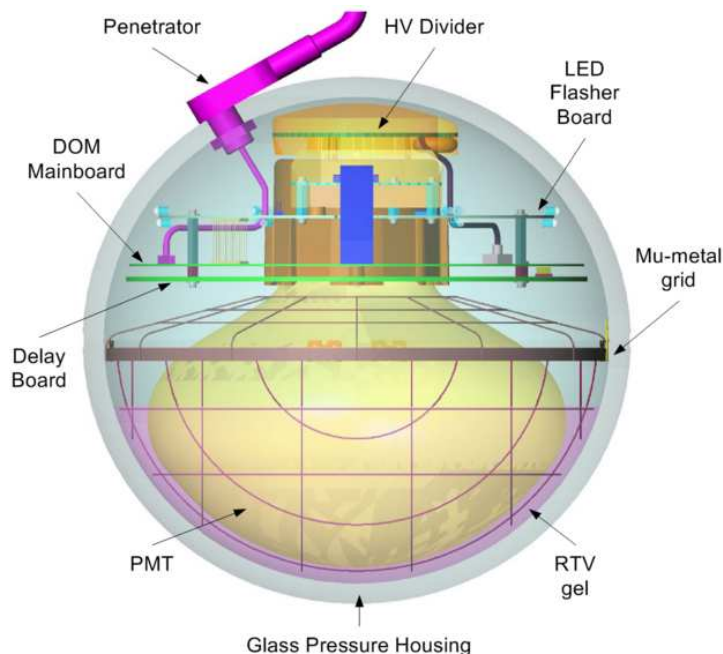


Figure 2.7: *Schematics of the DOM with the locations of the different components.*

When observing the output signal of a PMT, output pulses like those shown in Fig. 2.8 are

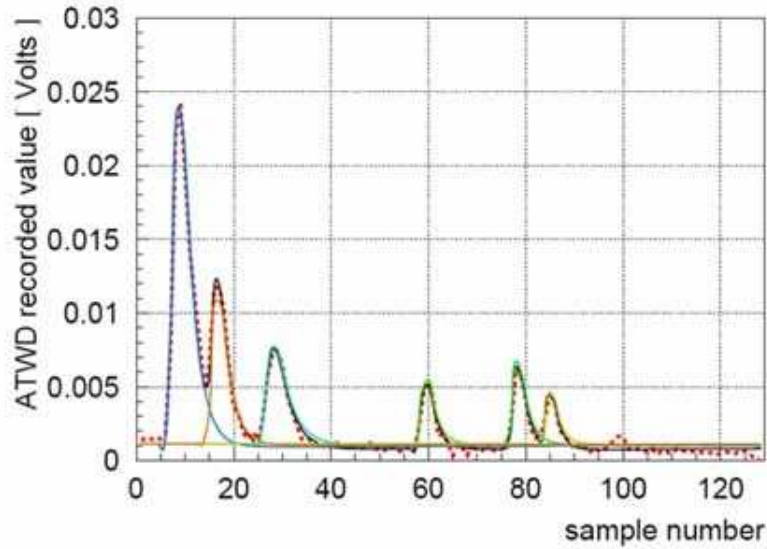


Figure 2.8: *ATWD output from a typical event showing multiple pulses and fit to a model result of a combination of single photoelectron responses. An average single photoelectron produces pulses of about 10 mV in amplitude and 5 ns width.*

seen. The output signal is composed of discrete pulses due to the low light level. For each detected photon, the PMT produces single photon electron (SPE) pulses. The capture of these waveforms is realized with a custom Application Specific Integrated Circuit (ASIC), the Analog Transient Waveform Digitizer (ATWD). Whenever one or more photons are detected, the DOM digitizes the pulse(s) and creates a "hit", the digital output unit, which contains a timestamp generated locally within the DOM, a measure of the charge, amplitude and width of each of the pulses, as well as information about the Hit origin. The waveform is decomposed into a list with the features of each of the associated pulses, which will be used for event reconstruction. The waveform in Fig. 2.8 presents multiple pulses associated to the multiple photons produced by a typical event. In the figure it is shown the data from the ATWD and the fit to a model based in a combination of single photoelectron responses. A few samples are digitized before the primary pulse and many afterwards, comprising a time interval of $6.4\mu\text{s}$, which is more than the maximum time interval over which the most energetic events are expected to contribute detectable light to any of the DOMs. The baseline can be used to determine the normal operating level. For detailed information about the technical design of the DOMs and the DAQ system in general see (113).

Local coincidence

When a hit occurs, a DOM opens a flexible time window (usually less than $1\mu\text{s}$). If during this window, a signal is received from a neighbor DOM, then we say that the local coincidence (LC) requirement is satisfied. If a DOM which is not receiving any hit, receives a signal from a neighbor, it will also establish an identical time window to accommodate the possibility that it may also receive a hit. Therefore, hit information includes the presence or absence of signals from neighbor DOMs, allowing to distinguish between particle induced hits (which will produce hits in adjacent DOMs) and PMT noise (which produces isolated hits).

Trigger

At this step, we need to determine which PMT readouts can be attributed to the same physical muon. In order to distinguish between noise induced and particle induced events, a trigger algorithm looks for PMT pulses correlated in time and space, which will be associated with particle induced events. Two trigger criteria are used mainly: Once the information from the Icecube strings is digitized and sent to

- Multiplicity trigger: requires eight hit DOMs (with local coincidence) within $5\mu\text{s}$ (running during 2007)
- String trigger: requires that five out of seven adjacent DOMs fired within $1.5\mu\text{s}$ (running during 2008)

AMANDA and IceCube are connected to two separate DAQ systems, TWR-DAQ and IceCube-DAQ, respectively. Each of them has its own trigger system. The trigger in the AMANDA subdetector requires events with either more than 18 hit DOMs or those which have 13 hit DOMs in $2.5\mu\text{s}$ with 9 of them at least not isolated, are kept.

Events observed simultaneously in the IceCube and the AMANDA arrays will be identified through comparing the GPS times of the events in each array. The joint event builder algorithm then combines the hits from AMANDA and IceCube to construct the events. If an event has triggered AMANDA then the trigger is also used as an IceCube trigger even if the triggering condition of Icecube is not fulfilled. This means that all the events which trigger AMANDA trigger IceCube as well. The opposite is not true. The logic behind this is that AMANDA as nested array is more sensitive to lower energy tracks that alone will not trigger IceCube.

2.4.2 Filters

The vast majority of events which trigger the detector are muons produced by cosmic rays in the atmosphere, resulting in a large data volume which consists mainly in events not produced by neutrinos. A full raw data transfer to the Northern hemisphere is not possible, since the satellite bandwidth for sending the data to the northern hemisphere is too small for that. Raw data is saved in tapes and carried to the North at the end of each winter season (in November) where it will be processed and analyzed. These are the so-called offline analyses. The need of having also an online data flow which allows us to analyse the data as it is being taken, demands the filtering of the data in order to match the satellite bandwidth requirements.

During the 2007 the IceCube trigger rate was about 525Hz, whereas the satellite bandwidth was about 36 GB/day. Various physics filters were proposed by the collaboration in order to reduce the data volume. The one relevant to this work is the so-called *Muon filter*, which selects events produced by muon neutrinos by their characteristic up-wards direction. This is done by performing fast, low CPU consuming, reconstruction algorithms which will separate the bulk of downgoing atmospheric muons from the upgoing neutrino induced muon tracks (see section 2.1.3).

2.5 Data analysis in IceCube

As introduced in section 2.1.3, the main steps in the data analysis of neutrino telescopes can be summarized as

- 1- Reduction of the event sample down to the neutrino level: elimination of cosmic-ray induced muons.
- 2- Identification of significant deviation from the atmospheric neutrino background: source(s) recognition techniques.

The reconstruction of muons tracks plays the main role in the data analysis in order to: a) get rid of the background of down-going atmospheric muons, and b) pinpoint the possible sources of muon neutrinos (above the atmospheric neutrino level). The reconstruction methods used in IceCube as well as the simulation chain used to develop signal to background rejection techniques, are common to all the IceCube analysis. Low levels of the data processing deal with the suppression of the bulk of cosmic-ray muons, while maintaining a good signal efficiency and taking into consideration CPU requirements. At this stage the pointing accuracy of the reconstructions is not important, and fast, first-guess reconstructions are performed, which give an approximation of the event direction. After removal of

the events reconstructed as down-going, the remaining events are then subject to successive better reconstruction algorithms, which allow to reduce the number of background muons misreconstructed as up-going, through a more refined selection of events according to their reconstructed direction and their quality reconstruction parameters.

Different optimization strategies, and hence different analyses, start mainly with the development of refined signal-background separation techniques based on the parameters of the reconstructed tracks of the events. The adopted strategy is studied using simulated data, for which the same processing as for experimental data is applied. Once the highest quality reconstruction is applied to the data, and after removal of the last background muons still present in the sample through the chosen combination of cuts in the track parameters, the remaining events constitute the final neutrino sample, mostly composed by atmospheric neutrinos. At this point, we have the best estimation of the muon's direction and energy (optional) obtained in the analysis, which are used in the last steps of the analysis: the strategies for the search for astrophysical neutrinos.

2.5.1 Event reconstruction

The IceCube DOMs record the light of the Cherenkov photons produced by a high energy muon on its way through the detector. The output of the DOMs is a waveform of charge versus time related to space coordinates. In the IceCube reconstructions, waveforms are either used directly or transformed into a list of photoelectron arrival times at a certain position, in order to find the best approximation for the direction of the particle which created the signals recorded in the DOMs (see section 2.4). In AMANDA, the data acquisition system recorded only the leading edge time of the photomultiplier pulse, the total charge in the pulse, and the total time over threshold of the pulse; no full waveform is available for the reconstruction. This section covers the basic aspects of the methods for the event reconstruction in IceCube, in particular those ones which were used in for the analysis of the data of IC22+AMANDA.

First-guess algorithms

First-guess algorithms serve two purposes in the data analyses, they provide a fast way to determine the direction of an event in order to separate between up-going signal neutrino event and down-going background events², and they are used as seeds to the likelihood reconstructions performed at more advanced stages of the analysis. Among the different first-guess reconstructions available, the most important for the standard Muon Filter are

²First-guess algorithms are used at the South Pole for event filtering in order to fulfill CPU and satellite bandwidth requirements

the linefit and JAMS (Just Another Muon Search) reconstructions. They are described in (115).

Likelihood reconstruction

After the first cuts based on the event zenith from the first-guess reconstructions, the remaining events are subject to more sophisticated likelihood reconstructions.

The method of maximum likelihood applied in this context consists of estimating the properties of the muon that caused the measurements in the optical modules; that is, the location, orientation and energy of the muon traveling through the detector. The available information to construct the likelihood function consists in the measured photon arrival times at the location of the optical module, and pulse charge. The reconstruction is done by maximizing the likelihood with respect to the unknown parameters of the muon track, seeded by the values from the first guess reconstructions. Track reconstructions in the IceCube detector also include the possibility of using the waveform directly. The likelihood in this case is formulated as the probability of observing a waveform $f(t)$ given an expected photo-electron distribution $\mu(t)$ (product of Poissonians). Since this work focuses on the combined detector IceCube+AMANDA, this approach for the reconstruction is not taken into account, since AMANDA DAQ does not capture full waveforms. I focus in the reconstruction methods based on the distribution of the photon arrival times. Waveform-based likelihood reconstructions are explained in (116).

The problem in the formulation of the likelihood function in this case is reduced to the choice of the single-hit likelihood function $p(x_i|\mathbf{a})$, where a hit is defined as the arrival time of a single Cherenkov photon at the optical module, giving rise to a photo-electron (see section 2.4). There are two approaches to construct this PDF, (1) an analytic approach, the so-called Pandel PDF (117), and (2) using Photonics tables (118). The IceCube reconstructions using Photonics tables involve the use of waveforms. As mentioned before, these reconstructions are not used in AMANDA due to the lack of full waveforms; therefore this approach is not contemplated in this work.

Pandel PDF

These reconstructions use the arrival times of Cherenkov photons (hits) measured at an optical module to reconstruct the track geometry. It takes into account that photons are deflected due to scattering, which causes a delay in the arrival time compared to the expected travel time from a direct photon; and considers the PDF of time residual of a hit, defined as $t_{res} = t_{measured} - t_{expected}$, instead of the hit time. The likelihood is written as

$$L_{Pandel}(\vec{a}|hits) = \prod_i^{N_{hits}} P(t_{res,i}|\vec{a}) \quad (2.4)$$

which gives the probability of observing a set of hit times given a certain hypothesis. In this case the hypothesis is a muon traveling through the detector with $\vec{a} = (\vec{r}_0, t_0, \Phi, \theta)$. This probability is equal to the product over the probabilities of individual residual times of hits produced by the muon in question.

The processes which determine the photon arrival times are Poisson processes. Waiting time to the k th event in a Poisson process with rate Φ is distributed as Gamma(k, Φ). The PDF of the time residual distribution of Cherenkov photons (Pandel function) is taken as a gamma distribution with parameters $k \equiv \frac{d}{\lambda}$, $\Phi \equiv \frac{1}{\tau}$ and has the form

$$P(t_{res}) \equiv \frac{1}{N(d)} \frac{\tau^{-(d/\lambda)} t_{res}^{(d/\lambda)-1}}{\Gamma(d/\lambda)} e^{-(t_{res}(\frac{1}{\tau} + \frac{c_{medium}}{\lambda_a}) + \frac{d}{\lambda_a})} \quad (2.5)$$

It is assumed a bulk ice (clear ice without dust layers), where λ_a , λ are the effective absorption length, and effective scattering length, respectively; d is the distance between the hitted optical module and the emission point along the muon track, and $\frac{1}{\tau}$ is the rate of observation of photons. The distance d is usually taken to be an effective distance in order to take into account the fact that the light is more scattered when the PMT is oriented away from the light source³. The normalization is given by

$$N(d) = e^{-d/\lambda_a} \left(1 + \frac{\tau c_{medium}}{\lambda_a}\right)^{-d/\lambda} \quad (2.6)$$

The Pandel PDFs of residual time of single photo-electron (SPE) considered in equation 2.5 do not account for uncertainties in the timing due to jitter and noise in the optical modules, which can scatter the hit residual time making the distributions broader. Jitter is taken into account in the PDF by a convolution of the Pandel PDF with a Gaussian of σ corresponding to the jitter in IceCube DOMs or AMANDA OMs.

The Pandel function distributions are determined mainly by the particle location and orientation, thus for the energy reconstruction another likelihood is constructed.

Likelihood reconstruction algorithms used in IceCube

- Bayesian reconstruction. Uses a weighted prior following a predefined probability distribution for the zenith of the track hypothesis. The weighted prior takes into

³PMTs in IceCube are facing downwards

account that most of the events observed in the detector are down-going.

- Paraboloid reconstruction. For a detailed explanation about this reconstruction see (119).

2.5.2 Event Simulation

To what concerns data analysis, event simulation is crucial in order to study the effect of any cut in the data and to develop search strategies. Simulation of events in IceCube takes place in different steps according to the different components involved in the problem. The main parts of this chain are:

- Event Generators: creates primary particles (cosmic-rays, atmospheric neutrinos, astrophysical neutrinos) and their interactions up to the point they produce secondary particles (muons for the cases considered in this work) that might be detected by IceCube.
- Muon Propagation: simulation of secondary particles (muons) from the point of their creation until they loses all its energy.
- Photon Propagation: simulation of the Cherenkov photons emitted by the muon on its way through the detector.
- Detector simulation: simulation of the different detector components and software which intervene in each of the steps from the interaction of the Cherenkov photons with the optical modules up to the creation of the events.

CORSIKA Air-Shower Generator

The simulations of the extensive air showers generated by interactions of high energy cosmic-rays with the nuclei in the atmosphere which give rise to the atmospheric muon flux seen by IceCube is performed using the CORSIKA code (120). In the IceCube frame, a slightly modified version of CORSIKA is adapted for the simulation of muons, which allows to sample individual particles from a primary particle spectrum. It simulates primary particles according to the Hörandel Poly-gonato cosmic-ray spectrum (121).

Neutrino Generator

The simulation of the neutrinos leading to muons is performed with the neutrino event generator program called neutrino-generator (NuG). The physics implemented in this program

is based on the ANIS-All Neutrino Interaction Generator (122) but it has been adapted to work in the IceCube framework.

With NuG we can inject neutrinos at the Earth's surface following a power-law with a user defined spectral index. NuG subsequently calculates the neutrino flux near the detector by simulation of neutrino propagation in the Earth, and calculates the probability of an interaction as well as the probability of the various interaction channels (most of the time either CC or NC) and subsequent child particle distributions. NuG stores the information of the primary neutrino near the detector with two composite particles. The composite is either *a charged-lepton and a hadron* or *a neutrino and a hadron*, depending on the type of interaction. This information is passed to the charged lepton propagator module.

Once the neutrino signal is identified through a detailed data analysis, searches for extraterrestrial neutrinos have to discriminate a possible astrophysical signal against the atmospheric neutrinos (see section 2.1.3). In order to make an optimal use of simulated events, neutrinos are produced following a generic energy spectrum and in a second step proportionally weighted in order to obtain the desired energy distribution and event rate. In order to apply this weighting procedure correctly, we have to use the probability that the generated neutrino flux creates a flux of secondary muons near the detector. This is done from a combination of MC simulation and event probability calculations in NuG, from where we can access the neutrino type, energy and coordinates of each simulated event, as well as the neutrino propagation and interaction probability. With this "probability weight" for each event we can obtain the weight corresponding to a certain theoretical neutrino flux.

Lepton and Photon Propagation

The full MonteCarlo simulation of the propagation and interaction of the generated muons through the Earth and through the detector is performed with the Muon Monte Carlo (MMC) code (123) specifically developed for AMANDA and IceCube. The particle is propagated until the algorithm finds a point where the particle has lost enough energy to be considered stopped. The algorithm takes into account the muon energy losses due to ionization, bremsstrahlung, photo-nuclear interaction, and pair production.

The Cherenkov radiation created by the muon is simulated once the muon reaches the active region of the detector. In addition, all secondary showers with energies above 500 MeV produced in the detector effective volume create their own Cherenkov radiation, which is considered separately for each secondary.

The ice at the South Pole exhibits strong variations of its optical properties, in wavelength as well as in depth. With current CPUs, it is impossible to do a dedicated tracking of

each photon emitted within the range of the detector by a high energy particle, and for a large number of events. The propagation of the Cherenkov photons emitted by the muon and the secondaries is done with the software package PHOTONICS, which instead of propagating each single photon calculates the probability for a given optical module to detect a photon at a certain time. For a detailed description of the light tracking through ice with PHOTONICS see (118).

Detector Response

There are various blocks in the simulation of the detector response, depending on which detector component or which piece of software is involved at each step.

- Compute the number of photo-electrons created by each particle at each optical module.
- For each photo-electron compute the arrival time at an optical module and create a hit
- Simulate the photo-multiplier (PMT) response for each hit
- Simulate the DOM response for PMT pulses
- Apply the same trigger conditions as used for real data.

Chapter 3

Analysis of the data obtained with IC22+AMANDA

In this chapter I focus on the analysis of the data obtained during the 2007-2008 operation period of the combined detector IceCube 22 strings (IC22) plus AMANDA. At the time of this work, analyses with the data taken with AMANDA plus 40 strings of IceCube are already underway¹. The current detector is taking data at present time with 59 strings.

The main topic of this work is to develop strategies for the search of high energy neutrinos from our Galaxy. As explained in chapter 1, the most common approach in high energy neutrino telescopes assumes that signal events follow an E^{-2} spectrum without an energy cutoff up to at least 1 PeV. The data analysis are then optimized to energies above a few TeV in order to get rid of the bulk of atmospheric neutrinos and thus achieve the best signal to noise ratio (S/N). However, as discussed previously, there are strong reasons to believe that the neutrino spectrum from galactic sources may exhibit significant departures from the E^{-2} , no cutoff model. The natural approach to observe such sources is therefore to go to lower energies than the standard IceCube searches, where, despite of the background of atmospheric neutrinos, we would have the bulk of the emission from the source, and therefore, a better S/N.

To lower the energy threshold of the analysis while maintaining good discovery potential with only 22 strings of the IceCube detector is challenging. Low energy events ($E < 1\text{TeV}$) produce few hits in the detector, and reconstruction algorithms have to manage with the information gathered with only 22 strings. In order to achieve good efficiency at lower energies, we have used the fact that, in the 2007-2008 configuration, the IC string arrangement is surrounding the AMANDA detector (see Fig. 2.5). This allowed to combine the data taken with both detectors and feed the reconstruction of event tracks with more information than in the case of IceCube alone.

The first studies about the integration and performance of the AMANDA detector inside

¹The last data from AMANDA, since it was shut down in 2009.

IceCube were carried out by Gross et al. (2008) (124), who pointed out that a combined detector configuration could extend the detection capabilities of IceCube in the energy range between 100 GeV-10 TeV. This analysis represents the first one using the combined detector configuration based on these studies.

The final data sample obtained with IC22+AMANDA constitutes the largest neutrino sample collected by IceCube in the 22 strings configuration, and corresponds to neutrino energies between $100 \text{ GeV} < E < 1 \text{ PeV}$. This analysis achieved the best sensitivity for point sources with neutrino spectra softer than E^{-2} and/or an energy cutoff below 1 PeV. In this sense, it was complementary to the standard IC only analysis reported in (5).

3.1 Strategy

As introduced in section 2.5, the data analysis in IceCube can be divided into two well differentiated parts:

- PART 1: elimination of muons produced by interactions of cosmic-rays in the atmosphere and acquire a clean neutrino sample.
- PART 2: identification of extraterrestrial neutrino events over the background of atmospheric neutrinos.

This chapter starts with the description of the processing chain involved in the part 1 of the analysis of IC22+AMANDA data. At the end of this part, the characteristics of the final neutrino sample will be presented. The main motivation of this work, to search for high energy neutrinos from our galaxy, takes form in the part 2 of the analysis. The search makes use of the neutrino sample obtained in the first part of the analysis in order to perform:

- 1) A scan of the galactic plane, seeking for point sources within the range $31.5^\circ < l < 214.5^\circ$, $-3^\circ < b < 3^\circ$ in galactic coordinates.
- 2) An analysis of the event pattern in the Cygnus star forming region of the Galaxy.

The scan of the galactic plane is carried out using the standard IceCube method for the analysis of point sources (7). The preparation and sensitivity of this scan will be presented at the end of this chapter. The analysis of the Cygnus region makes use of a method developed in this thesis in order to search for high energy neutrinos in extended regions, the Multi Point Source analysis. This method and its application to the Cygnus region with data from IC22+AMANDA will be presented in detail in the next chapter.

3.2 Datasets

Both experimental and simulated datasets are used in order to select the best strategy for an optimal separation between:

- muons produced by neutrinos and cosmic-ray induced muons (during part 1 of the analysis).
- atmospheric neutrinos and extraterrestrial neutrinos (during part 2 of the analysis).

During both, part 1 and part 2 of the analysis, the data sample is dominated by the corresponding background events in each case (atmospheric muons and atmospheric neutrinos, respectively). The data is randomized in azimuth² and the resulted scrambled skymaps are then used as representative of the background. In this way, we account automatically for all the different background components (single muons, double muons, etc). Background MonteCarlo is used only for comparison and understanding. Signal neutrino simulation is also needed to determine the properties of the analysis of IC22+AMANDA data, like the point spread function (PSF) and sensitivities.

Experimental data

The experimental data was collected during the operation period 31 May 2007 - 4 April 2008. The selection of good detector runs gave 274 days of usable data. The sample contains all the events that triggered IC22 or AMANDA or both detectors.

The IceCube detector can operate in three different run modes³:

- Mode 1: IceCube + AMANDA combined running (default)
- Mode 2: IceCube only mode
- Mode 3: AMANDA only mode

Due to a long-off period of the AMANDA detector due to technical issues, during 133 days data was taken in IceCube only mode. For the remaining 141 days IceCube was running in combined mode.

²The randomization is done only in azimuth in order to keep the zenith dependent distribution of background events over the sky.

³Only up to 2009, while AMANDA was still functioning.

Simulated data

The datasets used were generated within the simulation production of the IceCube collaboration (see section 2.5.2).

- **Atmospheric Muon Sample.** The dataset used corresponds to the amount of atmospheric muons recorded in 7.28 hr detector lifetime.
- **Muon Neutrino Sample.** The dataset used corresponds to muon neutrinos following an E^{-2} spectrum in the energy range $10 \text{ GeV} < E < 10^9 \text{ GeV}$. Events are then weighted according to an atmospheric neutrino model. Signal of astrophysical origin is also produced with this dataset; the events in this case are weighted according to different source spectra of the form $\propto E^{-\alpha} \exp(-\frac{E}{E_c})$ in order to study the efficiency of the analysis to different spectra.

3.3 PART 1: Elimination of atmospheric muons

Muons produced by ν_μ and muons produced by interactions of cosmic-rays in the atmosphere trigger the IceCube detector in its 22 string configuration at a rate of $\sim 550 \text{ Hz}$, and they trigger the AMANDA detector at a rate of $\sim 200 \text{ Hz}$. The overall trigger rate of the combined detector IC22+AMANDA after correction for overlaps is $\sim 640 \text{ Hz}$. The number of simulated atmospheric neutrino triggers for IC22+AMANDA is six orders of magnitude below this rate. The overwhelming amount of atmospheric muons imposes an efficient background rejection scheme which get rid of $\sim 10^6$ background events in order to reach the neutrino level. In this analysis, the data processing scheme is designed in order to remove all the background events while maintaining good efficiency for neutrino events with energies below 1 TeV.

High energy events produce more light in the detector and thus more hit DOMs in IC. Low energy events ($E < 1 \text{ TeV}$) produce few hits in the 22 strings of IC, but the reconstruction of the event track can be improved with the additional hits from AMANDA. Therefore, low energy events are expected to be mostly combined events, with hits in both AMANDA and IceCube. In order to cover a wide range of event energies in the final sample, the data is divided into two streams: a *combined* stream and an *IC only* stream, that will follow a different processing scheme and will be merged at final level. Depending on whether AMANDA has a trigger or not, and taking into account the different uptime between AMANDA and IceCube, events can in fact be divided into three streams:

- **Stream 1 : Combined runs with AMANDA trigger.** Events which trigger both AMANDA and IC22 in combined mode are merged and constitute combined events

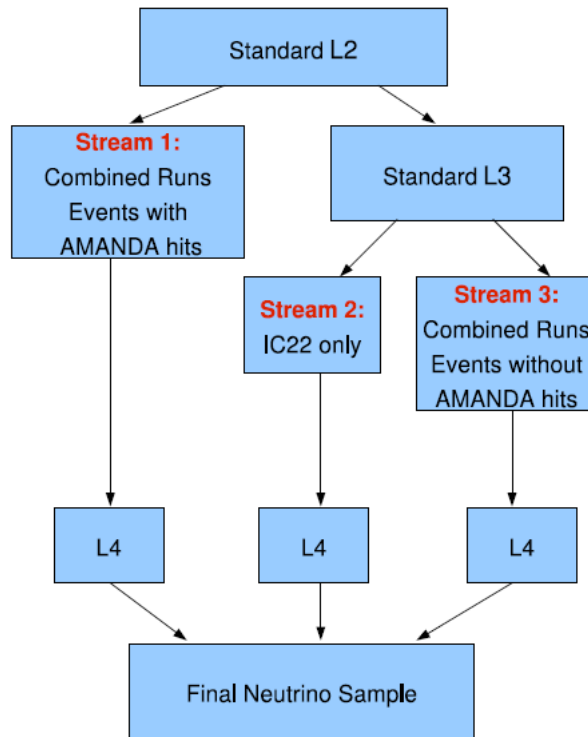


Figure 3.1: *Processing scheme applied in the analysis of IC22+AMANDA data.*

in this analysis.

- **Stream 2 : IC only runs.** AMANDA is off/bad. There is no information from AMANDA.
- **Stream 3 : Combined runs without AMANDA trigger.** AMANDA is on but has no trigger; IC22 has a trigger.

Streams 2 and 3 constitute *IC only events*, and stream 1 constitute *combined events*. In the standard IC22 point source analysis (5), the data sample is composed by IC only events taken by the detector in both standalone mode and in combined mode, but where the information from AMANDA was never incorporated into the reconstruction.

Fig. 3.1 shows a scheme of the processing chain in the analysis of IC22+AMANDA data. IC only events are processed up to level 3 according to the standard processing scheme developed for IC22 in (5). For combined events, a dedicated processing is developed in this work after level 2. At the last stage of the processing chain (level4), strategies for signal and background discrimination are studied for both the combined and the IC only sample separately.

Table 3.1: Muon Filter for 2007

	Zenith angle	Hits
IceCube Muon Filter	$\theta_{linefit} \geq 70^\circ$	$NCh_{IC} \geq 10^\circ$
	$\theta_{linefit} \geq 60^\circ$	$NCh_{IC} \geq 40^\circ$
	$\theta_{linefit} \geq 50^\circ$	$NCh_{IC} \geq 50^\circ$
AMANDA Muon Filter	$\theta_{JAMS} \geq 70^\circ$	$NCh_{IC} \leq 20^\circ, NCh_{AMA} > 0$

3.3.1 Level 1: event filtering with first guess algorithms

The standard *Muon Filter* based on first-guess reconstructions (see section 2.5.1) is applied on the events that trigger the detector in order to screen out a large background of atmospheric muons. The filter for the 2007-2008 detector configuration integrate an *IceCube Muon Filter* and an *AMANDA Muon Filter* in order to work optimally for both combined and IC only events. This was achieved using the JAMS (Just Another Muon Search) and the linefit first-guess reconstructions, which are optimized for low energy and higher energy tracks respectively. The CPU consumption of the JAMS algorithm (~ 155 times more than the linefit algorithm) requires a strict focussing on the most relevant events. For events with a few hits in IceCube, but potentially good with the additional hits from AMANDA, the JAMS reconstruction is applied. The 2007 Muon Filter requires that events pass either the IceCube Muon Filter OR the AMANDA Muon Filter. These filters select events according to their zenith angle, θ , and their channel multiplicity, NCh^4 . The filters are described in table 3.1.

Events which do not fulfill any of the conditions of table 3.1 will be rejected from the sample. This filter gets rid of the bulk of atmospheric muons in the detector with an efficiency of $\sim 95\%$.

3.3.2 Level 2: likelihood reconstruction

The main goal of the level 2 processing is to provide a high level reconstruction of the events that survived the Muon Filter. An iterative likelihood fit seeded with the first-guess from the linefit and JAMS reconstructions is used at this level on each event. At this point we still have a total event rate of ~ 32 Hz, ~ 10.5 Hz in the case of combined events and ~ 21.5 Hz for IC only events. Therefore, computing efficiency is still an issue. Only one iteration per event in the likelihood fit is allowed at this level. This option allows to identify and reject a large number of background events which were misreconstructed as upgoing by the first guess methods, while maintaining an acceptable consumption of CPU

⁴The number of channels is defined as the number of hit DOMs per event

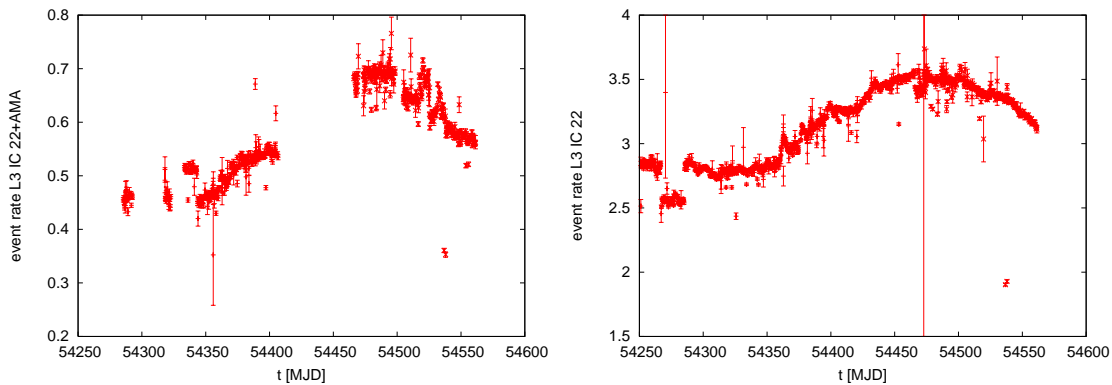


Figure 3.2: *Data rate as function of time for combined events (left) and IC only events (right) at level 3. The rate of IC only events is ~ 5 -6 higher than the rate of combined events.*

resources.

The likelihood uses a SPE gaussian-convoluted Pandel PDF (see section 2.5.1), which is convoluted with a gaussian in order to take into account jitter and noise. At this point, the processing of the data is separated into the combined and IC only streams in order to take into account that, for combined events, the noise rate is higher than for IC only events (due to technical differences between the AMANDA and the IceCube detectors).

Events with reconstructed zenith $\geq 80^\circ$ are kept for further processing. For combined events, this cut on the reconstructed zenith angle brings the data rate down to 1-1.4 Hz. For IC only events (streams 2 and 3) the event rate after the zenith cut is still ~ 6 Hz (see Fig. 3.2), and an additional cut is introduced in the standard processing in order to reduce computational time in the application of more accurate reconstructions on those events. According to the studies carried out in (5), a cut on the value of the reduced likelihood of the best fit track, $rlogl < 13$ reduces the data rate down to ~ 3.7 Hz.

3.3.3 Level 3: S/N discrimination

Up to level 2, the strategy for the data processing is identical for all the ν_μ searches. The rejection of the bulk of background events allowed to reduce the data volume significantly. The data sample composed by the remaining events, although still dominated by misreconstructed background muons, has now a manageable size, which allows to perform more elaborate likelihood reconstructions and studies of the events tracks.

At this level two things are desired: a) to get a good approximation to the true muon's direction, and b) to identify those parameters of the reconstruction which indicate whether

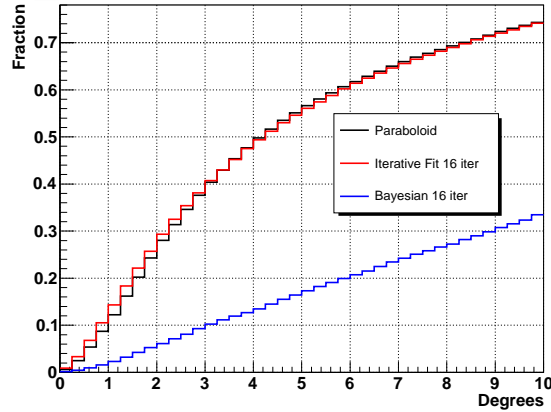


Figure 3.3: *Cumulative angular resolution for signal events following E^{-2} (right) at level 3 (IC only and combined) calculated as the difference between the true and the reconstructed muon direction. Bayesian reconstruction uses the downgoing muon zenith distribution as a Bayesian prior and thus it fails reconstructing signal upgoing neutrinos with the low number of iterations allowed at this level. The iterative likelihood fit is considered therefore the best fit of the event track at level 3, whereas the parameters from the bayesian and paraboloid reconstructions are used for signal/background discrimination.*

a track is well reconstructed or not. These quality parameters of the event track are used to discriminate between background and signal events. In addition, the topology of the hits is also important and can be used to further distinguish between background and signal.

The chosen strategy for the S/N separation, based on a series of cuts on the parameters of the reconstructed event tracks, is what defines different analysis. Some of these parameters are strongly energy dependent; therefore at this point the difference between the combined and IC only event streams becomes more notorious. Even with the additional information from AMANDA, low energy events can be interpreted as misreconstructed events, and a careful selection of cuts must be developed for combined events in order to keep as many low energy events as possible. The processing of IC only events at this level follows the same strategy studied in (5); here I describe in more detail the processing of combined events.

Combined events

An iterative likelihood fit seeded with the result obtained at level 2 is applied. This time 16 iterations are allowed. The results of this fit constitute the best angular resolution at this level (see Fig. 3.3), and events with reconstructed zenith $\geq 80^\circ$ from the iterative

likelihood fit are kept for further processing. The result of Fig. 3.3 indicate that the total event sample at level 3 has many bad reconstructed events, which will be lost at higher levels. The bayesian and paraboloid reconstructions (see section 2.5.1), although provide a worse estimation of the true event direction, are used for information about the quality of the reconstruction.

The parameters used to gather information about the event track are:

- Reduced log-likelihood (rlogl): defined as the likelihood value of the track reconstruction divided by the number of degrees of freedom. It is strongly energy dependent and tends to remove the low energy events.
- Number of direct hits (NDir): number of hits with time residuals between -15 ns and 25 ns⁵. Events with larger number of direct hits are usually reconstructed better.
- Length of the event (LDir): obtained projecting each hit OM onto the reconstructed track and taking the distance between the two outermost of these points. Larger values correspond to a more robust and precise reconstruction of the track direction. This parameter is particularly powerful when calculated for direct hits only, and then is referred to as LDir.
- Bayesian likelihood difference: difference between the zenith-weighted downgoing likelihood fit and the standard likelihood fit. It has a relatively weak dependency on the energy of the event and thus is an optimal parameter for the low energy approach.
- Paraboloid sigma. It provides the uncertainty in the track reconstruction of each event. It is defined in terms of the paraboloid error estimates for the major and minor axes x and y of the event error ellipse. Events with large sigma are considered as bad events and a cut on sigma is recommended in every analysis.

Comparison between the distribution of these parameters in data and simulation at level 3 is shown in figure 3.4 for combined events. At this stage, we are still dominated by misreconstructed muons by three orders of magnitude with respect to atmospheric neutrinos, and the distributions in the data are well represented by background events.

The optimal choice of the selection criteria depends strongly on the different expectations for signal and muon background events. Cuts on the quality parameters offer a solution to remove misreconstructed muons; however, low energetic up-going events leave less amount of hits in the detector giving rise to a low NDir, LDir, as well as few information for the reconstruction algorithms. As a consequence, the above-mentioned parameters have

⁵Time residual is defined as the difference between the observed hit time and the time expected for a "direct photon" (a Cherenkov photon that travels not delayed by scattering)

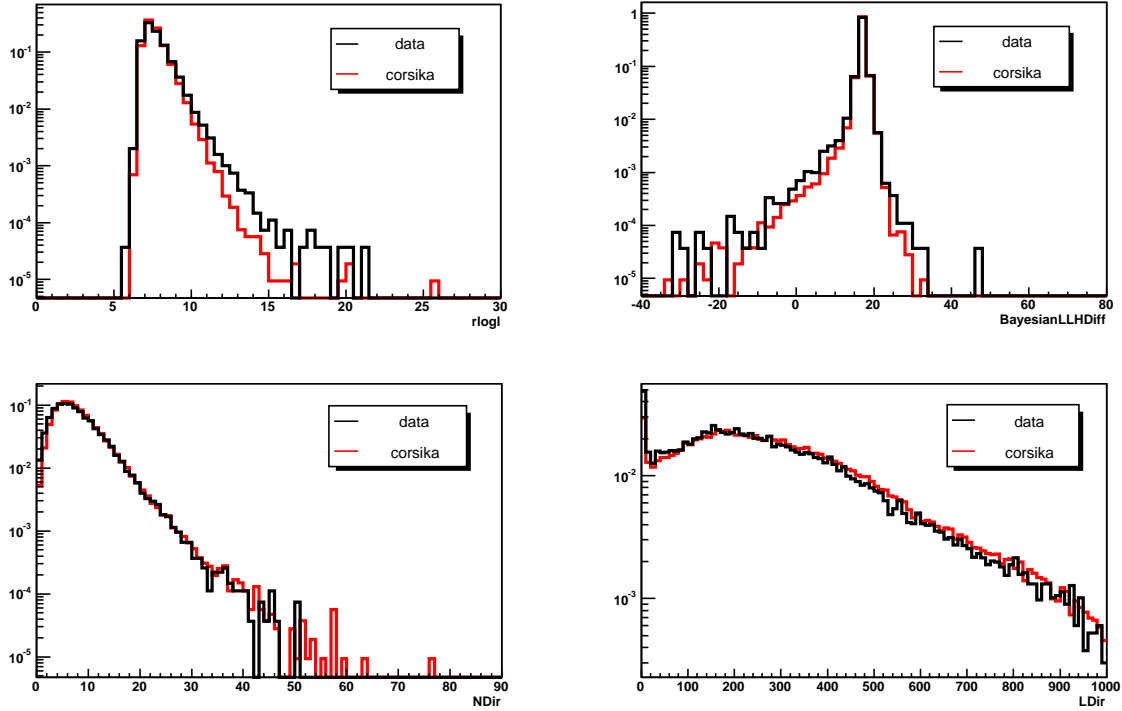


Figure 3.4: Comparison for combined events between the distributions of the quality parameters in the data and in simulation at level 3. From top-left to bottom-right: reduced log-llh, bayesian llh difference, number of direct hits, and length of the event. The black line is data and the red line is background MonteCarlo with CORSIKA. At this level, misreconstructed muons still dominate the sample by three order of magnitude respect to atmospheric neutrinos. The discrepancy between $rlogl$ and Bayesian can be attributed to the missing double muons in the simulated sample. The data corresponds to a single run in order to avoid unblinding of the whole data set.

a different behavior depending on the energy of the event, resulting in low energy events which can be misinterpreted as bad reconstructed events. In the low energy approach pursued in this work, it is preferable to select well-reconstructed tracks without relying in their energy, or at least minimize as much as possible the dependency with the energy of the analysis scheme. To reduce this effect and determine the optimal combination of cuts, the adopted strategy uses the Neyman-Pearson lemma, a likelihood ratio constructed using several parameters for an optimal signal vs. background discrimination. In this approach, for each of the selected parameters of the event track, an individual distribution obtained from the ratio of the normalized distribution for signal (atmospheric neutrino from the MonteCarlo simulations) and background (scrambled data) is constructed. The final likelihood distribution is defined as the product of the individual distributions.

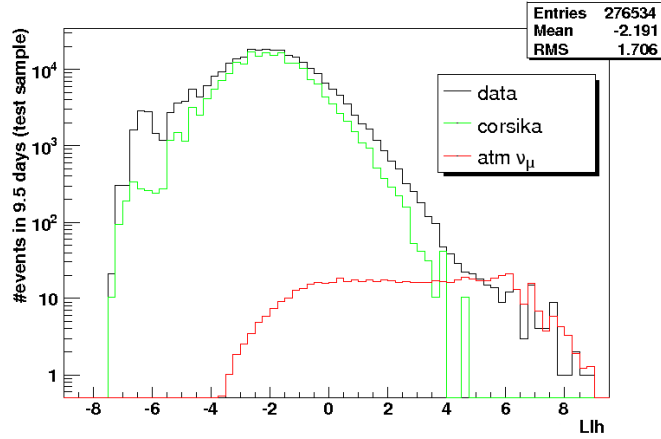


Figure 3.5: Comparison of the likelihood ratio at L3 for data, air shower MonteCarlo (CORSIKA), and atmospheric neutrinos MonteCarlo. The likelihood ratio is determined using a test sample of 9.5 days of data.

	Rate Before	Rate After
L1	180-210 Hz	9.5-11.5 Hz
L2	9.5-11.5 Hz	1.0-1.4 Hz
L3 (zenith cut)	1.0-1.4 Hz	0.5-0.7 Hz
L3 (llh ratio cut)	0.5-0.7 Hz	$8.2 \cdot 10^{-4}$ Hz $3.6 \cdot 10^{-4}$ Hz (Atm ν_{μ}) $1.6 \cdot 10^{-4}$ Hz (Corsika)
L4	$8.2 \cdot 10^{-4}$	$2.7 \cdot 10^{-4}$ Hz $2.8 \cdot 10^{-4}$ Hz (Atm ν_{μ})

Table 3.2: Event rates for combined events before and after the cuts at each level of the processing chain. The range in the event rates is due to the seasonal variations in the atmosphere's density. L1 is realized in the IceCube standard processing. At L2 reconstruction parameters are as in L2 standard processing but the noise rate considered is higher (noise probability = 8×10^{-5}).

Fig. 3.5 shows the distribution of the llh ratio parameter of combined events for data, corsika, and MC atmospheric neutrinos. The llh ratio was constructed with the distributions of the parameters of Fig. 3.4. The cut value on the llh ratio is chosen in order to maximize the S/N. With a cut at llh_ratio > 3.5 we remove 99% of the background while keeping good neutrino efficiency (see table 3.2).

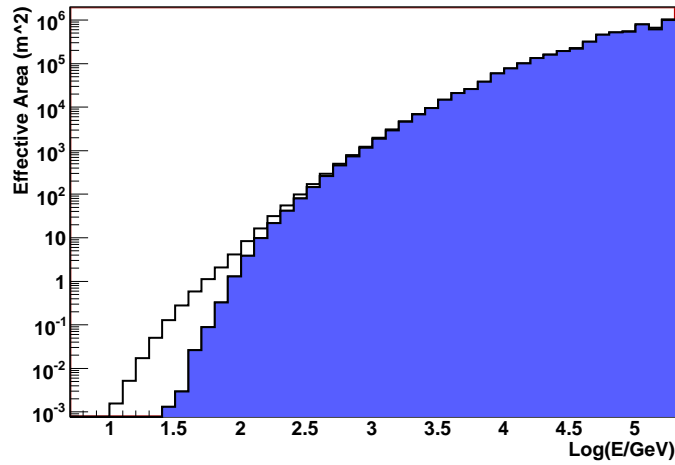


Figure 3.6: Effective area at level 3. Blue corresponds to IC only events and white stands for combined events.

IC only events

IC only events are subject to an iterative likelihood fit with 32 iterations and seeded with the results from level 2, as in (5). Those events with reconstructed zenith angle $< 80^\circ$ are eliminated from the sample.

For IC only events, the cut in the rlogl of the best fit track done at level 2 sacrifices the 9.2% of an E^{-2} signal, mostly the low energy part. However, in the analysis presented here, a fraction of these events belongs to the combined stream, and therefore they are kept in the IC22+AMANDA sample. Note that during the period in which the AMANDA detector was off, those events can not be kept in the sample. Even when the detector was in combined mode only during the $\sim 51\%$ of its total lifetime, the success of the low energy approach is illustrated in Fig. 3.6, which shows the effective area for IC only and combined events at this level.

3.3.4 Level 4: neutrino level

At this level the best likelihood fit is applied on the remaining events. A cut on the llh ratio as explained in level 3 is done also at this level with the improved parameters from the new reconstructions at level 4. A cut in the llh ratio of IC only events is also done in this case. In addition to the likelihood (llh) ratio, an additional cut on σ from the paraboloid reconstruction is added in order to increase the purity of the neutrino sample. Table 3.3 summarizes all the cuts at different processing levels for both combined and IC

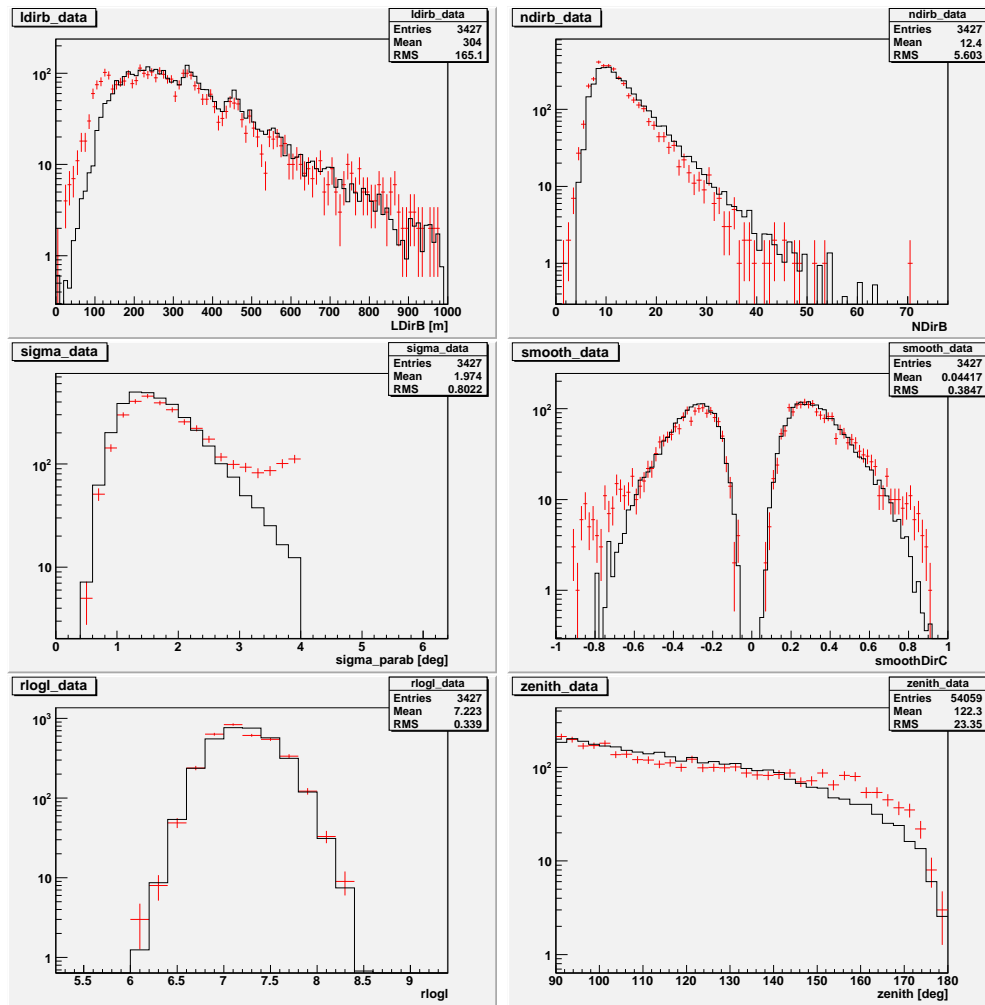


Figure 3.7: Distribution of the parameters of the event track for combined events for data (red) and simulated atmospheric neutrinos (black).

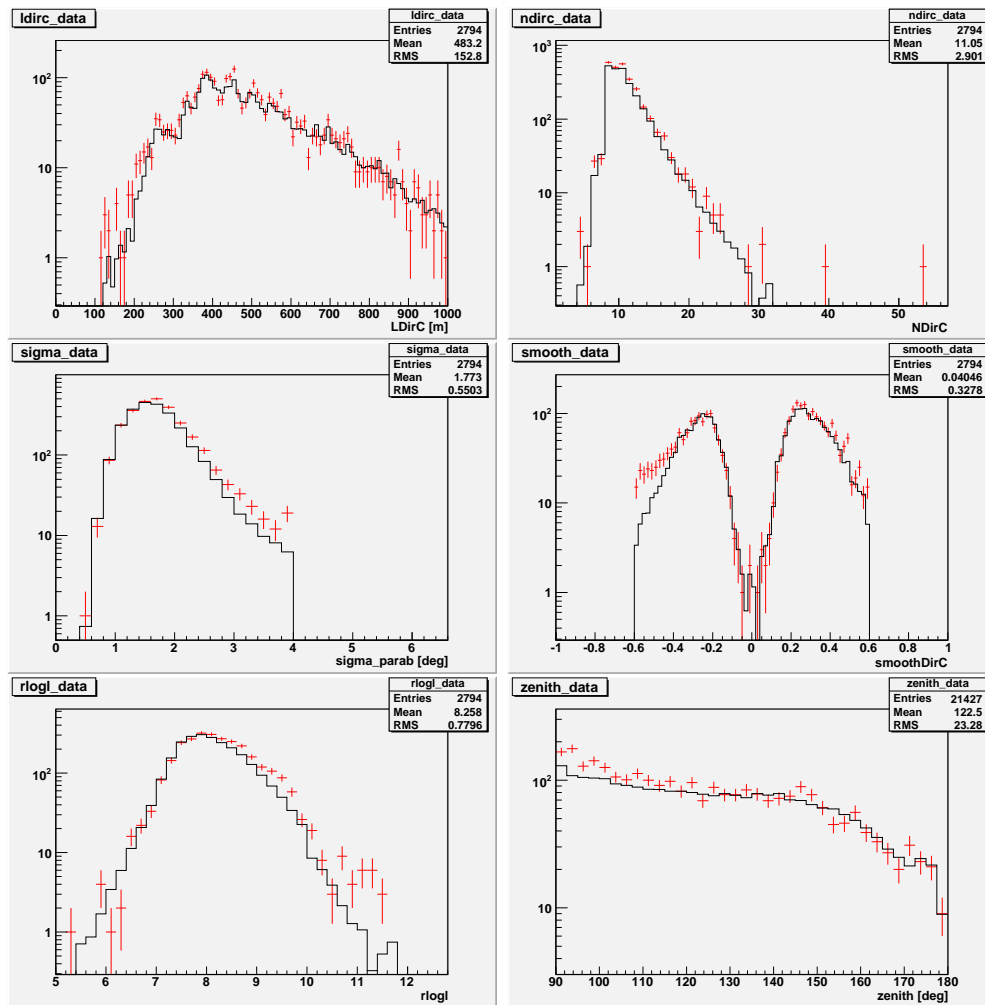


Figure 3.8: *Distribution of the parameters of the event track for events in IceCube only runs for data (red) and simulated atmospheric neutrinos (black).*

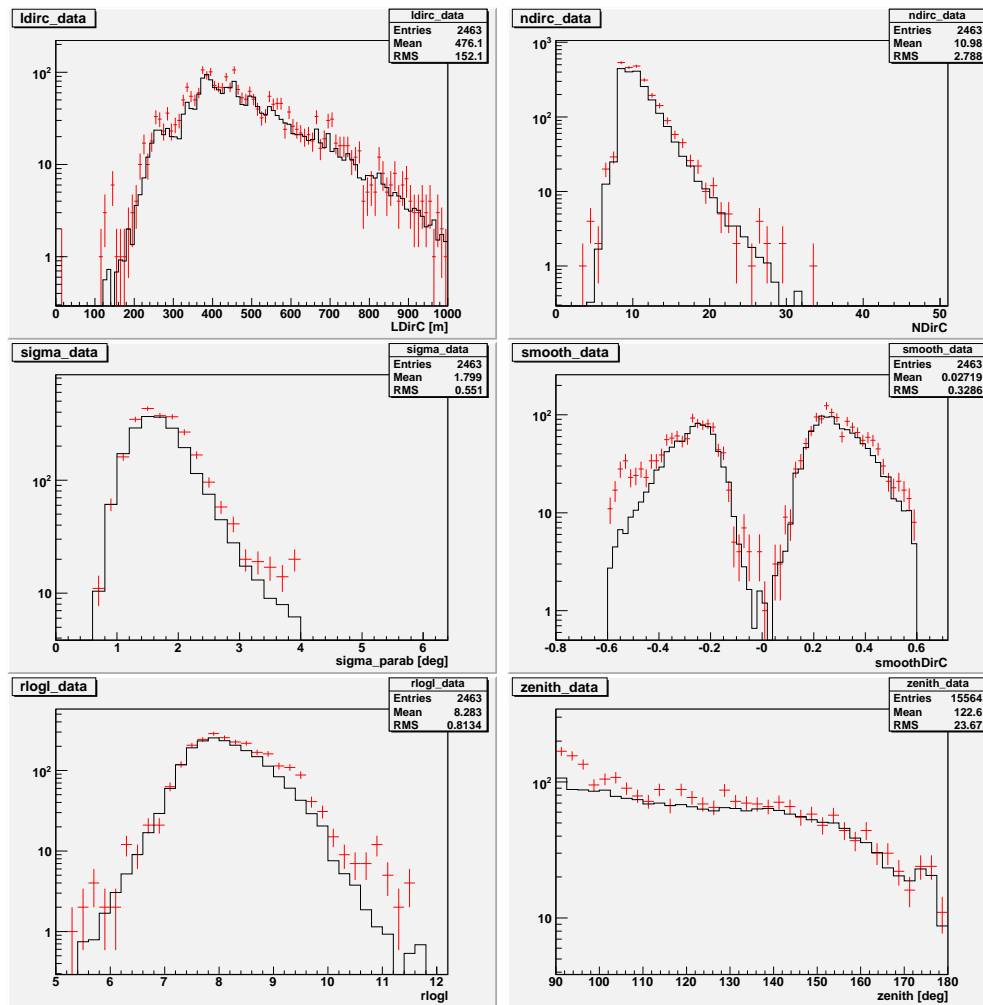


Figure 3.9: *Distribution of the parameters of the event track for events in combined runs with no AMANDA hits for data (red) and simulated atmospheric neutrinos (black).*

	Combined events	IC only events
L2	$\theta_{1iter} \geq 80^\circ$	$\theta_{1iter} \geq 80^\circ$ $rlogl < 13$
L3	$\theta_{16iter} \geq 80^\circ$ llh ratio > 3.5	$\theta_{32iter} \geq 80^\circ$
L4	$\theta_{128iter} \geq 90^\circ$ llh ratio > 4 sigma < 4	$\theta_{32iter} \geq 90^\circ$ llh ratio > 3.6 sigma < 4 smooth < 0.6

Table 3.3: Summary of the processing strategy in IC22+AMANDA.

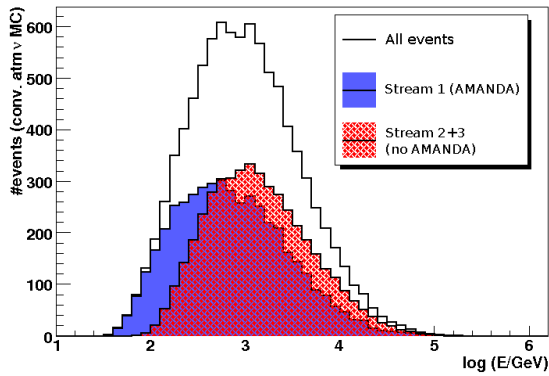


Figure 3.10: Energy spectrum of atmospheric neutrinos in the final sample of IC22+AMANDA. The contribution of the combined analysis is evident at energies below 1 TeV.

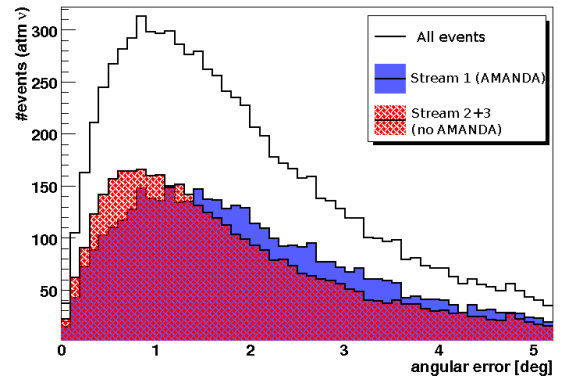


Figure 3.11: Angular resolution for atmospheric neutrinos in the final sample of IC22+AMANDA.

only events. After these cuts we arrive at neutrino level, and the two streams, combined and IC only, are merged.

After the last cuts at level 4, the remaining events constitute the candidate neutrino events, mainly atmospheric neutrinos. Figs. 3.7, 3.8, 3.9 show the distributions of different parameters of the reconstructed event tracks, for both data and simulations of atmospheric neutrinos, for stream 1, 2 and 3, respectively. The energy distribution of atmospheric neutrinos in the final sample is calculated from simulations and is shown in Fig. 3.10, illustrating the contribution of the combined sample at low energies.

The reconstruction of the event track constitutes at this point the best estimation of the true direction of the muon. The angular resolution of the analysis is determined using

simulations of signal neutrinos, and it is calculated from the angular difference between the direction of the primary neutrino and the direction of the reconstructed muon. Fig. 3.11 shows the angular resolution for atmospheric neutrinos at final sample.

3.4 PART 2: search for neutrinos from the Galaxy

This section describes the method used to search for point sources in the galactic plane using the final data sample obtained with IC22+AMANDA. The sensitivities achieved in this analysis will be compared with the ones in (5).

3.4.1 Galactic plane scan

The unbinned search method (7) is used to search for point-like sources. In this method a maximum likelihood fit is applied on the data to infer the number of signal events N_{sig} from the source.

For each event, the probability that it is a signal or a background event is calculated according to a certain signal PDF S_i , and a background PDF B_i , respectively. The likelihood function of a single event is then constructed as a mixture of these two probability distributions. The total likelihood function is written as the product of the individual likelihood functions of all the N events considered.

$$\mathcal{L}(N_{sig}) = \prod_{i=1}^N \left(\frac{N_{sig}}{N} S_i + \left(1 - \frac{N_{sig}}{N} \right) B_i \right) \quad (3.1)$$

In this analysis, all the events in the zenith range $\pm 5^\circ$ around the source location are considered in the likelihood function, The PDF of the spatial distribution of signal events, $S - i$, is assumed here to be a Gaussian

$$S_i = \frac{1}{\pi \sigma_i^2} \exp \left(\frac{-|x_s - x_i|}{2\sigma_i^2} \right) \quad (3.2)$$

where x_s and x_i are the source and event locations, respectively. σ_i is the error from the paraboloid reconstruction. The PDF of the background events is obtained from the zenith distribution of the events in scrambled IC+AMANDA skymaps. The likelihood ratio from the best fit to the background case ($N_{sig} = 0$),

$$\lambda = sig(N_{sig}) \cdot 2 \log_{10} \left(\frac{\mathcal{L}(N_{sig})}{\mathcal{L}(0)} \right) \quad (3.3)$$

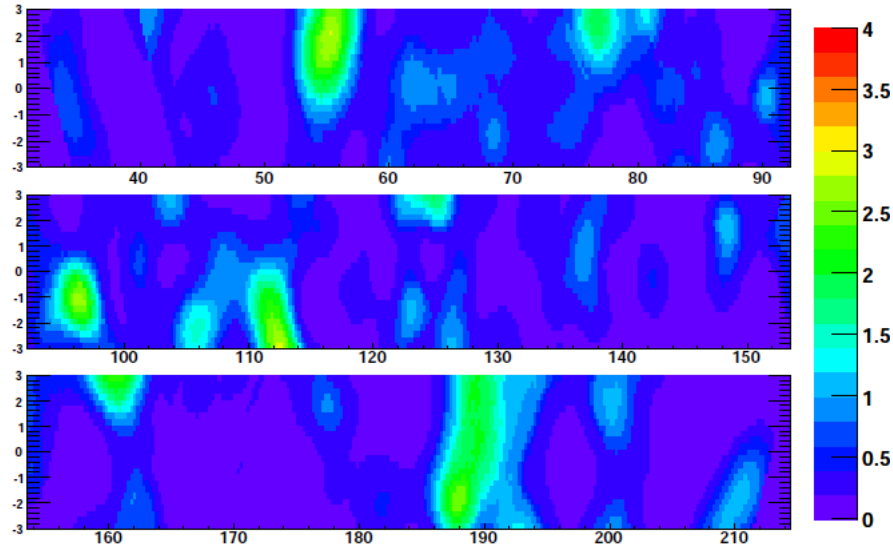


Figure 3.12: *Map of the background probability ($-\log_{10}p$) of the galactic plane scan for a scrambled skymap of IC22+AMANDA. Y-axis represents galactic latitude and X-axis represents galactic longitude.*

serves us as test statistics to define significances. In (7) an additional term in the likelihood which describes the energy distribution of signal events is included. Such an energy term will not be included in the method here due to the lack of an energy estimator for combined events.

The scan will be done superimposing a grid of $0.25^\circ \times 0.25^\circ$ over the selected area, where point sources are assumed to be located at each of the nodes of the grid. Fig. 3.12 shows the probability map obtained in a scan of the galactic plane using a random skymap from IC22+AMANDA.

3.4.2 Discovery Potential

The discovery potential is defined in IceCube as the minimum detectable signal required in order to reach a 5σ detection. This section compares the sensitivities of IC22+AMANDA analysis with the ones in (5) in order to evaluate the performance of the analysis presented in this work.

Figs. 3.13, 3.14 show the discovery potential for a Crab-like spectrum⁶ obtained in the

⁶A Crab unit is defined here in terms of the neutrino spectrum obtained from the gamma-ray spectrum assuming a model of pp interactions. Crab unit = $3.01 \times 10^{-7} E^{-2.4} \exp(-E/7\text{TeV}) \text{ GeV}^{-1} \text{ cm}^{-2} \text{ s}^{-1}$

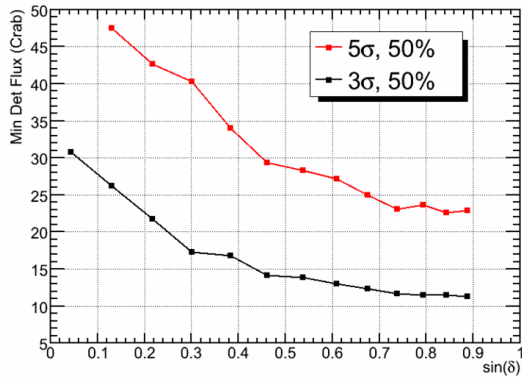


Figure 3.13: *Minimum flux required in this analysis in order to reach a 3σ and 5σ detection in 50% of the simulated cases using a Crab-like spectrum. It is calculated using the unbinned method for point sources without the energy term and it is given as function of the declination.*

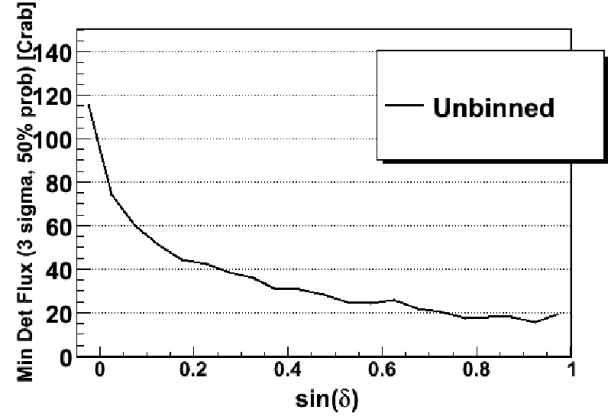


Figure 3.14: *Minimum flux required in the standard IceCube analysis (5) in order to reach a 3σ detection in 50% of the simulated cases for a Crab-like spectrum as function of the declination. It is calculated using the unbinned method with the energy term.*

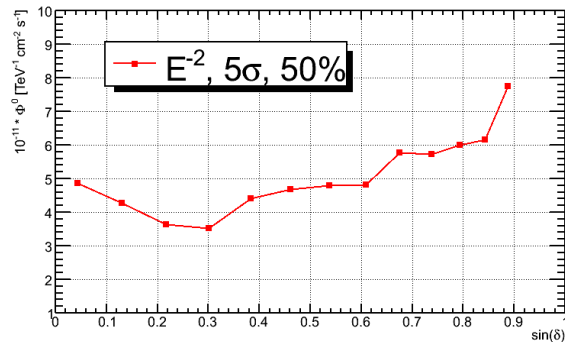


Figure 3.15: *Discovery potential at 5σ achieved in this analysis for an E^{-2} , not cutoff spectrum as function of the declination. It is calculated using the unbinned method for point sources without the energy term.*

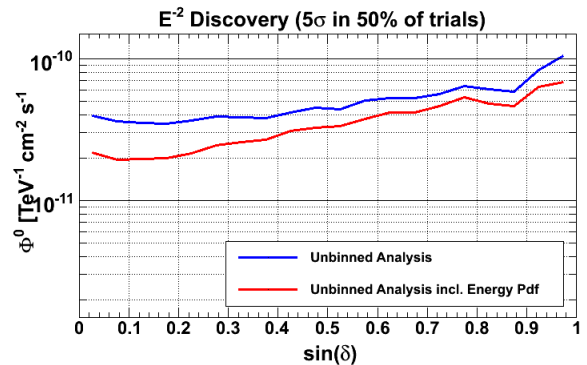


Figure 3.16: *Discovery potential at 5σ achieved in the standard IC analysis (5) for an E^{-2} , not cutoff spectrum as function of the declination. It is shown the discovery potential using the unbinned method with and without the energy term).*

IC22+AMANDA analysis and in the standard IceCube analysis (5), respectively. The analysis presented in this work achieved the best sensitivity, showing a large improvement in performance with respect to the standard IC analysis.

Figs. 3.15, 3.16 show the discovery potential of this analysis and the standard IC analysis for an E^{-2} , no cutoff spectrum. This model is the one commonly used in the standard analysis. The unbinned method weighted with energy becomes powerful under this approach. Without the energy term in the likelihood, the sensitivity of the IC and IC22+AMANDA analysis are comparable.

Due to the rapid loss of efficiency of the unbinned method weighted with energy with changes in the source spectrum (7), and given the fact that the neutrino spectrum from galactic sources has an energy cutoff well below 1 PeV, the obtained data sample represents the most optimal to make detailed searches of high energy neutrino sources in our galaxy.

Chapter 4

Multi Point Source analysis for extended regions

The Galaxy is a clump of stars, gas and dust embedded in a halo of dark matter. Structurally, it is usually defined as a late type, disk galaxy with a relatively small stellar bulge, and with most of the gas and dust located in a narrow band usually referred to as the thin disk. The location of the Solar System in the Local spiral arm within the disk, gives us a particular perspective of the Milky Way. Given the distribution of the cold gas in the Galaxy and the position of our local reference system, most of the star forming regions are observed in a narrow band of the sky, increasing the chances of finding different star forming regions close on the plane of the sky because of projection effects. Massive star forming regions are usually encompassed by large molecular clouds and particle accelerators like supernova remnants, microquasars, binary pulsars, or the winds of extremely massive stars. It is then likely that hadrons are accelerated in such environments, giving rise to neutrinos from their interactions with the dense matter fields present in those regions.

The Cygnus region, located between $65^\circ < l < 85^\circ$ is a good example of superposition of potential neutrino sources which are physically separated by several kpc but appear, from our perspective, together on the sky plane. Our line of sight to Cygnus is almost parallel to the Local spiral arm, which causes that all the star formation regions and potential neutrino sources appear in a projected area of $\sim 20^\circ \times 8^\circ$. The presence of the Cygnus region in the high-energy gamma-ray sky (125) motivates the development of an efficient search method which takes advantage of the overall emission in the region, improving significantly the IceCube discovery potential compared to conventional point-source searches. The development of such a search method for extended regions, its properties and potentials are the topic of this chapter.

The current statistical methods used in the analysis of neutrino data exploit the features which distinguish the signal from a point source from the uniform background of atmospheric neutrinos, like the spatial clustering of events and the energy spectrum. However, so far such a description has not been optimally designed in an extended region radiating

neutrinos (like the Cygnus region). In this case, the location, shape and number of potential neutrino sources is unknown, and a strongly model dependent analysis may not be the desired approach.

This chapter presents the methodology developed for the first analysis of the spatial neutrino event pattern in regions of the sky larger than IceCube angular resolution. It is important to stress here that such extended regions¹ might comprise a number of relatively faint neutrino sources of any morphology, which remain undetected in conventional point source analysis.

In order to extend the search beyond the scale of a single point source, it is desirable to have a method which: (1) is model independent, being able to perform optimally under different scenarios, that is, under different types of emissions, and (2) takes advantage of the full signal content from the region, being able to lower the detection threshold for single point sources.

In order to fulfill these goals, this work examines the spatial event pattern in a certain region of the sky for different scales of observation using a scale dependent clustering function. The implementation of such a function has been fine-tuned to maximize the potential of discovery of extraterrestrial neutrinos. If the events inside the study region are only due to the atmospheric neutrinos generated at those locations, the spatial distribution of events will be that of a random process. However, an extraterrestrial component in the event population would be caused by a spatial dependent process, resulting in a spatial distribution of events which is no longer random, but rather showing variations in the local event density that generate clustering, or in other words, correlations between the events. The analysis presented here, named the Multi-Point-Source (MPS) analysis, aims to detect these correlations in order to discover relatively weak neutrino sources, hidden for standard analysis, which are located within the same patch of the sky.

The performance of the MPS is studied and compared with the current search methods for different values of the event density, starting from the expected value in IC22+AMANDA up to the values corresponding to the large datasets expected after one year of operation of the full IceCube detector. The results obtained in this work using the MPS method indicate that it is more sensitive to event patterns which depart from the single point source case than the standard search methods. In addition, for the large event densities expected in one year of the full IceCube detector, the MPS provides also better sensitivity for single point sources which show an energy cutoff in the neutrino spectrum below 1 PeV than standard point source searches.

The application of MPS has been devoted so far to the search for neutrinos in an area of $11^\circ \times 7^\circ$ around the center of the Cygnus region using the data collected with the combined

¹The expected angular resolution for the complete IceCube detector is $\sim 1^\circ$

detector IC22+AMANDA. This chapter presents a description of the construction, interpretation and performance of the MPS analysis as well as its application to the Cygnus star forming region of the Galaxy with IC22+AMANDA.

4.1 Concepts and methods in the analysis of event patterns

A point pattern consists of a set of event locations (r_i, r_j, \dots, r_N) within a region (R), at which N events have been recorded. In the simplest case, the data set comprises only the event locations. However, in some cases we may have additional information related to the events which might have a bearing with the nature of the analysis. For instance, the arrival time of the events, for analysis of variable sources; or the energy of the events for a higher signal to noise discrimination power. These cases correspond to what is known as marked point pattern. The analysis done in this work deals only with the event locations and does not take into account the use of marks. The possibility to include the energy of the events as additional information in the analysis was not considered here due to the lack of good energy estimators for combined events in IC22+AMANDA.

A spatial point process which gives rise to the observed event pattern can be characterized in terms of its *first-order* and *second-order* properties.

- **First-order properties** describe the way in which the expected value of the process generating the events varies across R. They are described in terms of the intensity of the process, $\lambda(s)$, which is the mean number of events per unit area at the location s.
- **Second-order properties** describe the covariance (or correlation) between values of the process generating events at different regions in space. They arise in spatial dependent point processes and involve the relationship between numbers of event in pairs within R.

The first and second properties of a spatial process which give rise to a certain event pattern are defined by their respective intensities:

$$\lambda(s) = \frac{\langle Y(ds) \rangle}{ds} \quad (\text{first order intensity}) \quad (4.1)$$

$$\gamma(s_i, s_j) = \frac{\langle Y(ds_i)Y(ds_j) \rangle}{ds_i ds_j} \quad (\text{second order intensity}) \quad (4.2)$$

where ds is the area of a region around the point s , $\langle \cdot \rangle$ is the expectation operator, and $Y(s)$ refers to the number of events in this region.

We say that a process is random if the variations of $\lambda(s)$ across R are distributed according to a Poisson process and, in addition, $\gamma(s_i, s_j) = \lambda(s_i)\lambda(s_j)$. The latter condition implies that the second-order intensity of a random process depends only on the first-order intensity at s_i and s_j , and not on their absolute locations, meaning that no correlations exist between events.

In the context of a neutrino detector, event patterns in the data that deviate significantly from any of these two conditions indicate the presence of extraterrestrial signal. Methods for analysing spatial point patterns use different approaches for examining either the first-order or the second-order properties of a point process. Different approaches result from the different choices of the test statistics in each case. Each analysis constructs its own test statistics, in order to quantify the deviation of data from a random distribution of events, using different combinations of the first-order $[\lambda(s)]$ or second-order $[\gamma(s_i, s_j)]$ intensities in the data case and in the random case (126) .

According to the properties of the event pattern which are under examination, we can divide the techniques used so far for the discovery of extraterrestrial neutrinos which cluster (diffuse analysis are not considered here) into two main groups: (1) hot spot analysis and (2) two-point analysis. The former study the first-order properties of the spatial point process, whereas the latter deals with its second-order properties.

4.1.1 Hot spot analysis

Hot spot analysis investigate the first-order intensity of a spatial point pattern in order to identify hot spots, defined as a spatial concentration of events. So far, they have constituted the most common motivation for the data analysis, since they allow to locate the sources of high energy neutrinos. In IceCube, the search of hot spots is done by mapping the sky using two methods: a "classical" method (binned method), and a likelihood-based method (unbinned method).

Binned method

A binned search is the simplest of the hot spot techniques. It counts the number of events within a certain area (bin). The exploration of the sky with this method, seeking for sources of high energy neutrinos, is done by superimposing a grid of N_n nodes (s_1, s_2, \dots, s_{N_n}) over the event distribution and counting the events per bin centered at each grid node. As a result, the method obtains estimates of the intensity at each grid point $\lambda(s_i)$. The grid step

is usually much smaller than the angular resolution achieved in the analysis, and the bin size is usually optimized to achieve the best signal to noise ratio for point sources. In the case of extended sources, the amount of background integrated with this technique makes a possible discovery challenging.

Unbinned method

The unbinned method (7) is a "mixture model", which use a statistical description of the data in order to deal with events which can be in one or several components, but we do not know which. The data is modelled as a mixture of two probability distributions: the background and the signal components. The PDFs of the different components are modelled and the resulting likelihood function is fitted to the data.

This method gives a probabilistic assignment of an event to a component according to its distance to the point at which the intensity is being estimated. The way of mapping the sky in this case uses also a grid, but in this case the scan of the sky can be interpreted as, instead of using bins, using functions centered at the grid nodes which weight events according to their distance from the grid point. If (r_1, r_2, \dots, r_n) are the locations of the n events around a grid point s_i within the radius of influence of the weighting function, the first order intensity at s_i , interpreted in this case as a probability density, is calculated as

$$\lambda(s_i) = \sum_{j=1}^n \frac{1}{\sigma_j^2} f\left(\frac{s_i - r_j}{\sigma_j}\right) \quad (4.3)$$

In the implementation of the unbinned method for point sources, $\lambda(s_i)$ is assumed to be a gaussian centered at the source coordinates and stretched according to the error, σ_j , in the reconstruction of the event at r_j . The use of the energy of the events as a mark in the analysis is also exploited in IceCube within the frame of the unbinned method. This provides an enhanced signal to noise discrimination power for sources with hard spectra and without a cutoff in the relevant energy range $1 \text{ TeV} < E < 1 \text{ PeV}$. For sources with such spectrum, the unbinned weighted with energy yields an improvement of $\sim 50\%$ with respect to the binned method. However, for source spectra that departure from the E^{-2} , no cutoff model, the unbinned with and without energy term have similar performance, achieving only $\sim 10\%$ improvement with respect to the binned method in this case (7). The results of an unbinned search for extraterrestrial neutrinos provide probability density maps according to the model considered.

These hot spot techniques have been applied so far to the search for single point sources, either in an all-sky survey mode or targeting potential neutrino sources.

4.1.2 Two-point analysis

Two-point analysis estimate the second-order properties of the process that gives rise to the observed pattern, like the two-point correlation function of the data (127).

The impact of this method comes back to the late 70's from the work, both analytical and theoretical, by Peebles and co-workers to study the large-scale matter distribution in the Universe (127), (128). In high energy astrophysics, the searches for correlations in the data have been applied mainly to detect anisotropies in the spatial distribution of cosmic-rays (129), (130) and neutrinos (6).

The angular two-point correlation function $\omega(\theta)$ of a given event pattern is defined as the excess, with respect to a random distribution of events, in the probability δP of finding an event of type b in the solid angle $\delta\Omega_b$ at angular distance θ from an object of type a in $\delta\Omega_a$. That is,

$$\delta P_{ab} = n_a n_b (1 + \omega(\theta_{ab})) \delta\Omega_a \delta\Omega_b \quad (4.4)$$

where n_a is the mean density of events of type a and n_b the mean density of events of type b . This probability depends exclusively on the event densities n_a , n_b if the events are distributed randomly throughout the sky; in this case there is no correlation between the objects, $\omega(\theta) = 0$, and the probability is reduced to the random probability

$$\delta P_{ab} = n_a n_b \delta\Omega_a \delta\Omega_b \quad (4.5)$$

However, if the positions of objects of type a and b are correlated at the angular scales θ_c , the probability of finding an event of type b at an angular distance $\theta < \theta_c$ is higher than in the random, uniformly distributed case, yielding $\omega(\theta_c) > 0$.

Essentially, the correlation function describes the extent to which there is spatial dependence in the arrangement of the events.

4.2 Multi Point Source (MPS) analysis

Based on the current methods for the analysis of spatial event patterns in IceCube outlined in the previous section, there are two approaches to detect a possible astrophysical component inside an extended region:

- 1) Make a scan of the region and provide event density maps or alternatively probability

maps, as in the case of the unbinned method. This approach is more favorable for the cases in which the neutrino sources are intense, well defined "blobs" in space.

- 2) Study the correlations between the events, like the inter-event distances, with two-point analysis. These type of methods study the second-order intensity of the spatial point process. This approach has the advantage to sum up the emission of multiple weak signal components, making a possible detection more probable than with a single hot spot search.

MPS bases its search strategy in the study of the second-order properties of the process generating the observed spatial event pattern inside the region under study. The aim of the analysis is to determine whether these properties are compatible with those expected from a distribution of background-only events (atmospheric neutrino events) or if a extraterrestrial component has to be invoked in order to explain the observations, and at which level the background-only hypothesis (null hypothesis) is rejected.

Let R be the region under study, in which a total number of N_{inside} events have been registered in the final data sample at the locations $(r_1, r_2, \dots, r_{N_{inside}})$, defined by the coordinates $r_i = (\theta_i, \phi_i)$ on the sky. MPS makes a two-point sampling of R with circular bins of variable area $A = \pi\Theta^2$ centered at the locations of each of the events inside the region, r_i . That is, MPS does not not correlate events with specific locations, but rather it considers each event inside the region as a point source in order to determine later its degree of correlation with the rest of the events. This peculiarity of the analysis is precisely what names the method as "Multi Point Source". The sampling of R with bins centered at each of the events has the additional advantage that it allows MPS to measure, not only the correlations between events, but also the excess of events in the region as a whole.

In the sampling of the region the distance, Θ_{ij} , from an event i located inside R to an event j (at any location) is measured at each of the N_{inside} events present in R ($i = 1, \dots, N_{inside}$; $j = 1, \dots, N_{total}$). The number of pairs ij is measured as function of the angular separation and the histogram of event pairs as function of the angular distance Θ is constructed from these measurements. The realization of this procedure over a large number of scrambled datasets results in the average histogram of pair distances for the null hypothesis.

The analysis then makes use of a scale dependent clustering function, $\Phi(\Theta)$, defined as the excess, with respect to the null hypothesis, in the number of event pairs within a certain distance:

$$\Phi(\Theta) = \frac{\int_0^\Theta P_{data}(\Theta')d\Theta'}{\int_0^\Theta \langle P_{random}(\Theta') \rangle d\Theta'} \quad (4.6)$$

where $P_{data}(\Theta) = \sum_{ij} P_{data}^{ij}(\Theta)$ is the number of pairs of events at the scale of observation Θ , and $\langle P_{random}(\Theta) \rangle = \langle \sum_{ij} P_{random}^{ij}(\Theta) \rangle$ is the expected number of event pairs randomly distributed in Θ . By definition, in both $P_{data}^{ij}(\Theta)$ and $P_{random}^{ij}(\Theta)$, either the event i or the event j , or both, must be within R .

The use of the clustering function defined above as a test statistics has several advantages:

- 1) It is model independent. No specific assumption about the signal is made in MPS and the analysis is therefore optimal under different types of emission.
- 2) It can accomodate regions of complicated shapes and boundaries, making MPS not dependent on the shape selected for the region.
- 3) It can take advantage of the full signal content of the source, being able to recover signal of various weak sources as well as diffuse emission present in the region.
- 4) Its functional behavior provides a way to scan the region searching for clustering at different angular scales, with an insignificant associated statistical penalty.

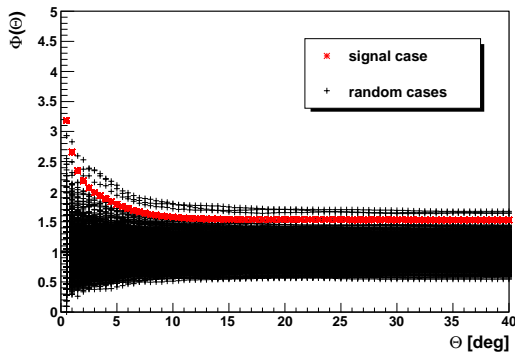


Figure 4.1: Average clustering function obtained after applying MPS over a region R of $8^\circ \times 8^\circ$, where five point sources are simulated with random positions within R . The black crosses represent the fluctuations on the expected value of the clustering function under the hypothesis of randomness, obtained from the realization of MPS over 10^4 random skymaps.

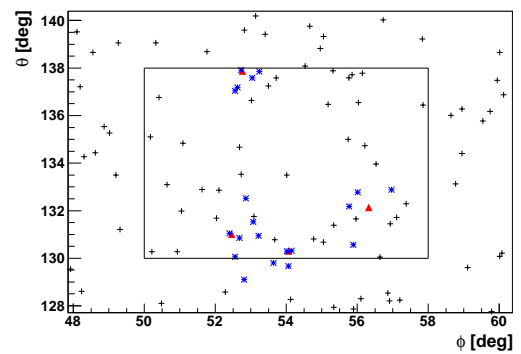


Figure 4.2: Map of event locations from one of the cases of the signal example considered. Black crosses represent the population of background atmospheric neutrino events and the blue stars correspond to neutrino events from astrophysical sources. The location of the point sources is marked with a red triangle. The square represents the region where MPS is applied.

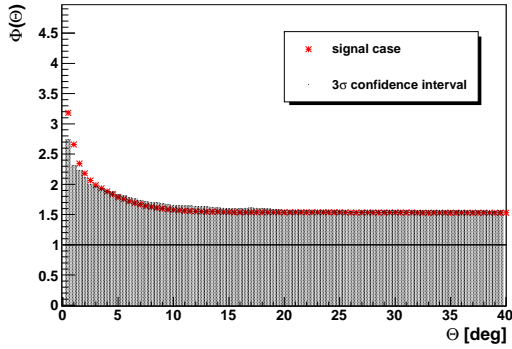


Figure 4.3: *Average clustering function of the example considered overplotted over the 3σ confidence interval. MPS reaches 3.7σ at the smallest scales of observation in 50% of the simulated event patterns.*

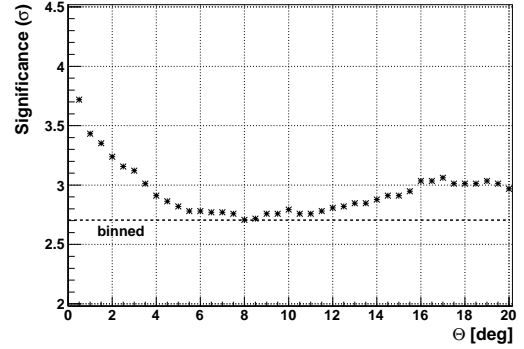


Figure 4.4: *Significance (in units of the standard deviation) obtained with MPS in 50% of the simulated event patterns as function of the scale of observation.*

In order to illustrate the construction and interpretation of MPS, an example using a simulated event pattern is examined. In the example, MPS is applied over a region $R = 8^\circ \times 8^\circ$ which covers the zenith band $130^\circ < \theta < 138^\circ$. A large number of both background-only cases and signal cases are generated in order to count with a statistical description of the outcome of MPS in both cases. Background and signal cases have been created as follows:

- Background events: their spatial distribution is assumed to follow a complete spatial random processes. A number of 15000 background events are injected randomly over the sky ². This value has been chosen arbitrarily in order to show the performance of MPS, and it is representative of a small dataset with respect to the expected IceCube's collection capabilities³
- Signal events: produced by injecting events from point sources within R over the background events. Four point sources are assumed to be existing in the region, each one producing five events in the final data sample. The PDF of the spatial distribution of signal events is taken as a 2D gaussian with $\sigma=1$ centered at each of the locations of the point sources (which is a realistic approximation for the PSF of the full IceCube detector). The PDF of the spatial distribution of the point sources is assumed to be random within R .

²The sky here is assumed to be a semi-sphere, since the IceCube field of view is restricted to the northern hemisphere for the energies considered in this work.

³The current analysis with 40 strings of the IceCube detector already reached more than 20000 events at final sample.

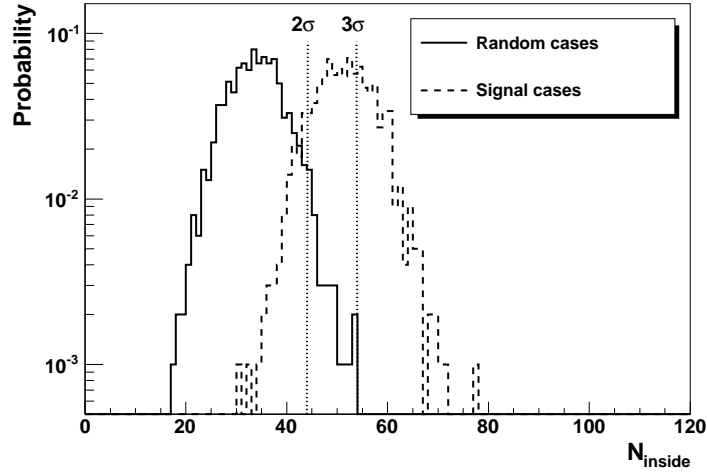


Figure 4.5: *Distribution of the number of events inside R in 10^3 random cases and 10^3 signal cases produced as explained in the text. A binned search reaches 2.7σ in 50% of the cases with the example considered.*

The average clustering function, $\Phi(\Theta)$, obtained from a series of realizations of MPS over the simulated signal-case datasets is displayed in Fig. 4.1. Values corresponding to $\Phi(\Theta) \approx 1$ would indicate absolutely no discrepancy between the expected number of event pairs in a random distribution of events and the measured number of pairs in the actual distribution. Scores higher than 1 indicate that events are more clustered than would be expected in a random distribution, and scores lower than 1 would indicate that events are more dispersed than in a random distribution. The plot also shows the outcome of MPS corresponding to 10^4 background-cases, which represent the random fluctuations of $\Phi(\Theta)$.

The obtained result shows evidence of clustering at any of the scales of observation Θ . At scales larger than the typical size of the region ($\Theta > 15^\circ - 20^\circ$ in the example in order to avoid edge effects), the excess is due to the clustering of events within R , no particular feature about the spatial distribution of events within R can be extracted at these scales. The smallest angular separations ($\Theta < 8^\circ$) combine the information about the small-scale clustering of neutrinos, where small-scale means at scales smaller than the typical size of the region, at the same time that measures the excess of events in R as a whole. In other words, the information stored at small angular scales, not only makes use of the enhancement of the detection rate because of the global emission from the region, but also, in the case of an extended region comprising many sources of neutrinos with some degree of spatial clustering, the fact that is very unlikely to have a distribution of atmospheric neutrinos with such a degree of clustering. Therefore, the small-scale clustering of events will leave an imprint in $\Phi(\Theta)$ that will add to the global enhancement due to the neutrino excess inside R .

The presence of four point sources in the region generates a clustering function which overcomes the null hypothesis at a 3.7σ level for the smallest angular scales observed. This statement is equivalent to affirm that the observed value happens in 0.01% of the simulated background-only cases. Fig. 4.3 shows the 3σ confidence interval for the clustering function under the null hypothesis, defined as the value of $\Phi(\Theta)$ with a $p_value^4=1.3\times 10^{-3}$. The scan over different values of Θ provides results of different significance. This is a consequence of the spatial behavior of both background and signal events and can be summarized into two main reasons:

- Such a scan allows to study the trend of the events within R to cluster at a certain angular scale. The most significant value of $\Phi(\Theta)$ will be the one associated to the scales at which such clustering exists.
- The probability that atmospheric neutrinos "cluster" at a given scale of observation decreases with Θ .

Given these facts, and as a consequence of the adopted PDF of the signal events, the four point sources in the example of Fig. 4.3 generate significant clustering of events at scales $\Theta < 0.5^\circ$, whereas the degree of clustering drops considerably at scales $\Theta > 2^\circ$. Fig. 4.4 shows the significance achieved at each of the scales of observation compared with the one obtained in a binned search (see also Fig. 4.5). This illustrates the advantage of using the second-order properties of a spatial point process in order to detect event patterns produced by relatively weak sources of high energy neutrinos.

4.3 Performance and discovery potential of the MPS

The goal of MPS is to detect, within the same region of the sky, event patterns which are not obvious by the standard search strategies. The previous section showed how to quantify the spatial structure of a given event pattern at different angular scales in terms of the clustering function. The validity of the null hypothesis on the data is checked through the use of hypothesis tests. Such tests define both the significance of the experimental outcome and the sensitivity of the analysis. In MPS, the null hypothesis is represented by the function $\Phi_0(\Theta)$, that holds $\langle \Phi_0(\Theta) \rangle = 1$ for all values of Θ . In order to reject $\Phi_0(\Theta)$ for one or more values of Θ and claim a discovery, the IceCube policy requires that the corresponding values of $\Phi(\Theta)$ in the data must overcome the random fluctuations of $\Phi_0(\Theta)$ at a 5σ significance level; equivalent to assign a probability of 2.5×10^{-7} to the null hypothesis. The minimum signal required to produce such an outcome is defined as discovery potential.

⁴This definition of 3σ corresponds to a one-sided test, as in the case at hand

4.3.1 PDF of the null hypothesis

The PDF describing the spatial distribution of background events in IceCube is usually based on the zenith distribution of the events in the final data sample, which is dominated by the background of atmospheric neutrinos. The PDF of the test statistics under the null hypothesis is commonly estimated from a large number of realizations of the same method from datasets scrambled in azimuth⁵. However, the estimation of the statistics with randomized data samples can become prohibitive, in particular for performance studies. It is then useful to count as well with a statistical model for the null hypothesis in order to study, in a faster way, the performance of MPS.

According to the definition of $\Phi(\Theta)$ from equation 4.6, the PDF of $\Phi_0(\Theta)$ for a fixed value of Θ is determined by the PDF of the number of pairs of events within Θ under the null hypothesis. I will show in this section that, under the assumption of a Poisson model for the spatial distribution of background events in the final data sample, the corresponding number of event pairs, N_p , within a given scale of observation Θ follows a two parameter Gamma distribution $G(k, \beta)$:

$$G(N_p; k, \beta) = \frac{N_p^{k-1}}{(k-1)! \beta^k} e^{-\frac{1}{\beta} N_p} \quad (4.7)$$

This statistical description of the background is proven to be correct for the IC22+AMANDA final dataset, as illustrated in Fig 4.6 and Fig. 4.7. The plots have been produced using a skymap from IC22+AMANDA scrambled in azimuth, which is representative of the atmospheric neutrino background, and the scale of observation has been chosen as $\Theta = 2^\circ$. Fig. 4.6 shows the fluctuations, across the zenith band $140^\circ < \theta < 150^\circ$, in the number of companions per event within bins of area $\pi\Theta^2$. The total number of events per bin is therefore the number of companion events plus one. The right plot shows the variations in the number of close pairs formed per bin of events. These measurements can be interpreted as a single-point and a two-point sampling of the zenith band under study with circular bins of fixed-area $A=\pi\Theta^2$. A single-point sampling is sensitive to the first-order properties of the process which is generating the events in the zenith band $140^\circ < \theta < 150^\circ$. In the scrambled skymap of IC22+AMANDA considered here the intensity of the process shows fluctuations following a Poissonian. The two-point sampling of the same zenith band in the same scrambled dataset, which is sensitive to the second-order properties of the process generating the events, has a variance 3.58 times larger than in an expected Poisson process.

Fig. 4.8 shows the distribution of pairs of events within $\Theta = 2^\circ$ (close pairs) obtained from 10^5 realizations of MPS in a region of $11^\circ \times 7^\circ$ of scrambled skymaps from IC22+AMANDA.

⁵The randomization of the event coordinates is done only in azimuth in order to maintain the zenith dependency of atmospheric neutrinos.

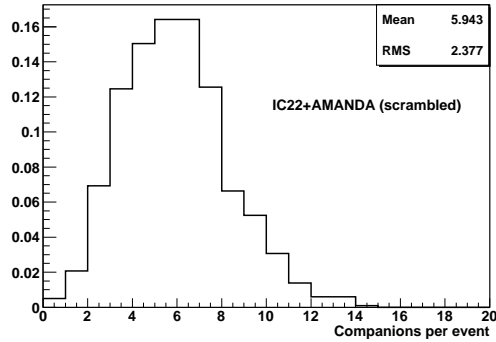


Figure 4.6: *Relative frequencies of the number of companions per event within $\theta = 2^\circ$ in the zenith band $140^\circ - 150^\circ$ from an IC22+AMANDA skymap with randomized azimuth. The number of events per bin area $\pi\Theta^2$ corresponds to the number of companions plus one. Each event has on average 5.9 companion events within 2° . Fluctuations on this number appear across the zenith band according to a Poisson process.*

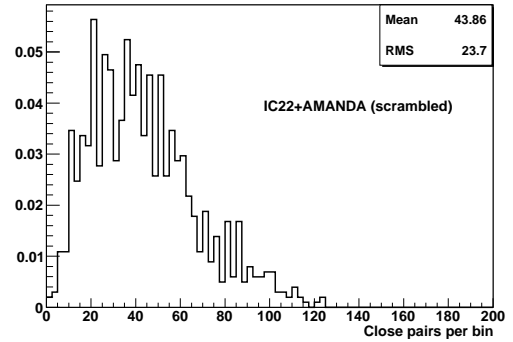


Figure 4.7: *Relative frequency of pairs formed per bin of events with angular separation $\theta \leq 2^\circ$ in the same zenith band. The distribution of close pairs is very sensitive to density fluctuations and has a larger variance than expected in a Poisson process.*

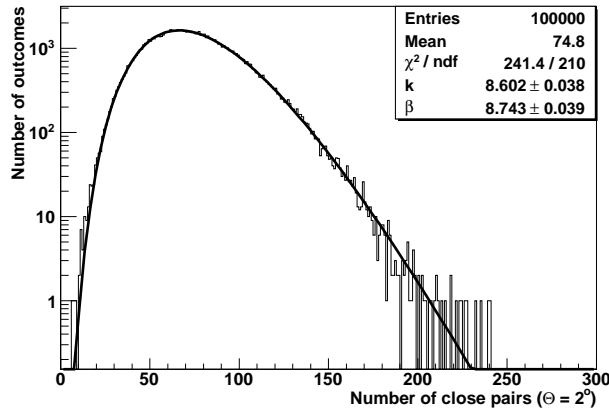


Figure 4.8: *Distribution of close pairs obtained after apply MPS on a region of $11^\circ \times 7^\circ$ over 10^6 scrambled skymaps from IC22+AMANDA and fit to a $\text{Gamma}(k, \beta)$.*

The distribution of close pairs is fitted to a Gamma distribution $G(k, \beta)$ (equation 4.7), showing that this model provides a good approximation to the actual distribution. However, the parameters k, β of the distribution of close pairs (or equivalently the distribution of the clustering function for a fixed value of Θ) do not show a direct dependency on

observables, which may lead to problems in applications of this model. For the purposes considered here, this approach is useful in order to fit the distributions and define 5σ confidence intervals, avoiding the computation of 10^7 random cases. As mentioned above, the discovery potential in IceCube is set at a 5σ threshold and the minimum detectable signal required with MPS to reach a 5σ detection will be presented. However, for studies of the performance of MPS and the comparison with current search methods under different scenarios, it is enough to provide performances at 3σ level, which is accessible from repetitive evaluations of the test.

4.3.2 Comparison with current search methods

In this section the performance of MPS is compared mainly with the binned method, since the unbinned method can only be applied in extended regions in a scan mode. For simplicity in the comparisons, signal events are simulated following a point-like pattern, since this is the case at which standard analysis are more sensitive. Note however that MPS can take advantage of clustered emission of any morphology. For comparisons with the unbinned method, it is important to note that the performance of the unbinned method is strongly energy dependent. As a consequence, for sources with a cutoff in their neutrino spectrum well below 1 PeV, the performance of the unbinned and binned method are comparable. Comparison of the minimum detectable flux of the unbinned with energy term and the MPS will be presented only in the application to the Cygnus region with IC22+AMANDA (section 4.4).

The capabilities of MPS to detect a signal more efficiently than conventional methods are studied in terms of the physical parameters of the problem; that is, the total number of events in the final data sample (N_{total}) and the size of the region under study (R). The PDF of the spatial distribution of background events in a certain patch of the sky is assumed to be that of a Poisson process, which, according to the previous discussion provides an adequate model for the final datasets of IceCube. Hence, a number of N_{total} events are injected randomly in the IceCube sky (restricted to the northern hemisphere in this work) to be representative of the atmospheric neutrino background component. Signal events are injected on top of this background in order to determine the minimum signal required to reject the null hypothesis at a certain confidence level. The PDF of signal events is assumed to follow a gaussian of $\sigma=1$ (median $\sim 0.85^\circ$), which is a good approximation for the error in the event reconstruction of the full IceCube detector.

Fig. 4.9 shows the minimum detectable signal to noise ratio required to achieve a 3σ detection with the MPS compared to the one required applying the binned method as function of the area of the region under study. The $(S/N)_{3\sigma}$ is defined as the excess in the number of events inside R , with respect to the expected number of background events,

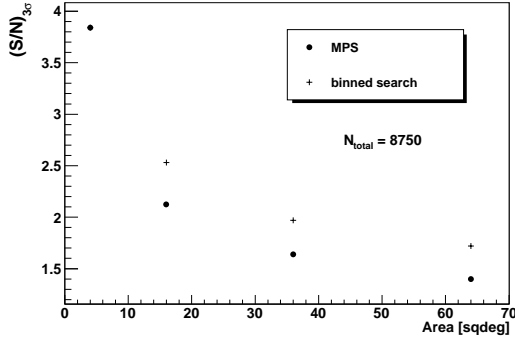


Figure 4.9: *Minimum detectable signal to noise ratio required to reach a 3σ detection with MPS compared with a binned search as function of the area of the region.*

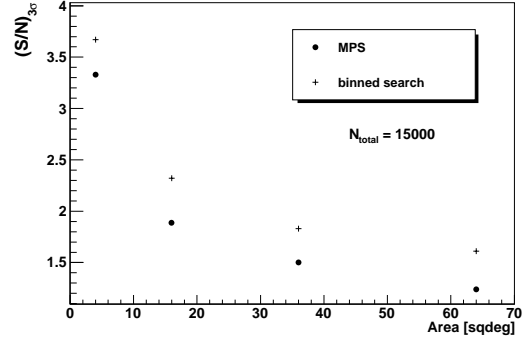


Figure 4.10: *Minimum detectable signal to noise ratio required to reach a 3σ detection with MPS compared with a binned search as function of the area of the region.*

that we must observe in order to reach a 3σ detection. The sensitivity of MPS depends strongly on how the events are distributed inside the region. The wide range of possibilities translates in discovery potential ranging from the most clustered case to a pure diffuse case. The plots report the performance for the most clustered case, which is also more convenient for the comparison with respect to single point source searches. The most clustered case has been constructed assuming that all the emission from the region comes from a single point source, where the events are injected according to the assumed PSF (with median $\sim 0.85^\circ$) centered at random positions inside R.

Due to the type of signal injected (point-like), the results obtained with MPS had always the highest significance for $\Theta < 1^\circ$, a regime in which the trial factors are insignificant.

Larger regions, as well as larger event densities, represent an improvement of the minimum detectable S/N for both MPS and a binned analysis due to the increase in the number of events which form pairs and the increase in the number of events inside the region, respectively, and the subsequently reduction of the random fluctuations in both cases. For small datasets, the improvement of MPS respect a standard binned search is evident at larger R. For larger datasets, even in the point source case (represented as the case in which $R = 2^\circ \times 2^\circ$), MPS represents an improvement with respect to a binned search (see Fig. 4.11), requiring 20% less signal for the event densities expected after one year of performance of IceCube (7). In terms of discovery, the results of Figs. 4.9, 4.11 indicate that, even with high statistics samples (high event densities), in regions of a considerable size (area $> 30^\circ$) the maximum clustered case requires a strong signal which will be detected by the binned analysis in an scan mode (i.e., in the all-sky search). The improvement of MPS with respect to standard searches takes place when the signal events in the region deviate from the single point source case (see section 4.4.1).

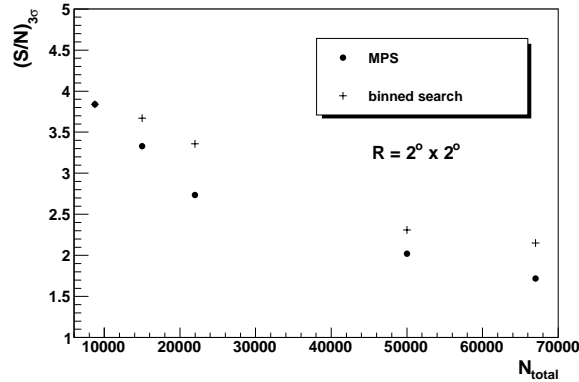


Figure 4.11: *Minimum detectable signal to noise ratio required to reach a 3σ detection with MPS compared with a binned search as function of the total number of events in the data sample*

4.4 Application to the Cygnus region

The development of a method to search for neutrinos from extended regions was motivated by the desire of observing the most active part of our galaxy within the IceCube field of view: the Cygnus star forming region. This area covers the region between galactic coordinates $65^\circ < l < 85^\circ$, $-5^\circ < b < 5^\circ$, and is one of the youngest and more massive star formation sites of the Galaxy (see table 1.3), comprising many astrophysical accelerators and large amounts of molecular material (see Fig. 4.12). The scenario seems promising for neutrino production.

This section presents the preparation for the study of the neutrino event pattern observed in the Cygnus region with the MPS method using data from IC22+AMANDA. The output of MPS consists in the measurement of the clustering function in the Cygnus region. The significance of the observations are computed in this case using a fixed scale of observation $\Theta = 2^\circ$, optimized from the simulations for IC22+AMANDA in order to achieve the minimum detectable signal to noise ratio for different source spectra. The reason to use fixed-area bins to sample the region was purely practical and based on removing as much as possible inter-bin trial factors.

Different patterns for signal cases are considered in the evaluation of the minimum detectable flux, like a diffuse event pattern, or a point source pattern. In the case of simulation of point sources, the influence of the number and strength of the point sources in the performance of the method is evaluated with respect to the existing search methods.

Data Sample

The data sample used for the search for neutrinos from the Cygnus region corresponds to the one collected by IC22+AMANDA. It consists of 8712 neutrino events from the northern hemisphere with energies above 500 GeV (see chapter 3 for details on the data treatment).

Selection of the Region

This analysis uses the central, most active part of the Cygnus complex, covering $72^\circ < l < 83^\circ$, $-3^\circ < b < 4^\circ$. This region of $11^\circ \times 7^\circ$, comprises the two brightest Milagro sources in TeV as well as a considerable part of the diffuse emission observed. Some of the Milagro spots lie outside the selected box; note however that MPS can still take advantage of a possible emission located outside the box that is close to the edge of the region. In what follows, I will refer to the selected region as the Cygnus region.

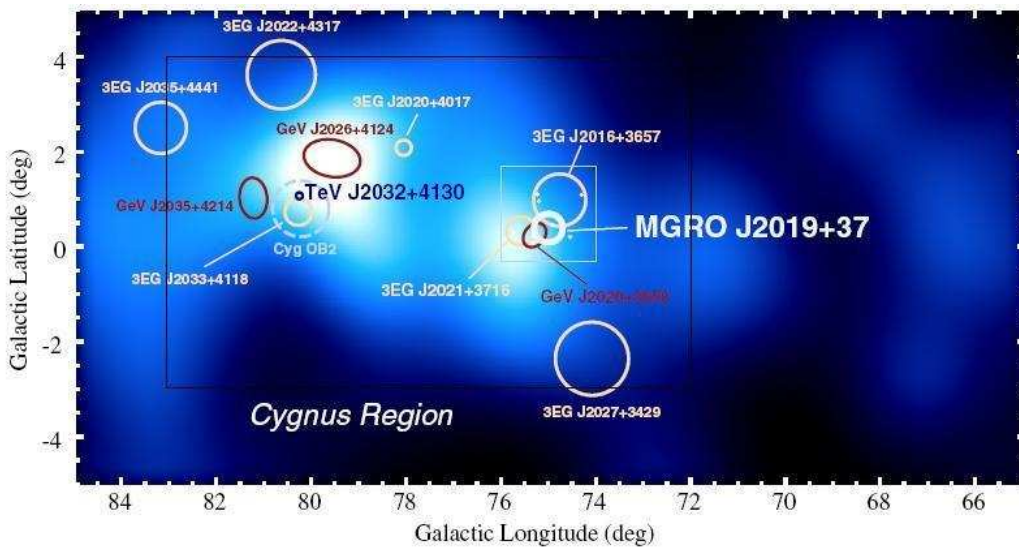


Figure 4.12: *EGRET* diffuse emission and point sources in the Cygnus region. The black square represents the area over which we will apply the MPS analysis. Image taken from (131).

4.4.1 Discovery potential to clustered and diffuse emission

The power of the analysis with MPS relies on the deviations of the angular distribution of events in the sky respect to a distribution of background events. As a consequence, the sensitivity of MPS depends on how the events are distributed inside the region, ranging

from a purely diffuse case to a maximum clustered case. In the worst-case scenario, all the emission is diffuse. In this case, for the event densities expected in IC22+AMANDA, MPS performs as a binned analysis⁶. In case some clustering is present due to the presence of point sources or clusters of point sources MPS presents a better sensitivity than both an unbinned and a binned search.

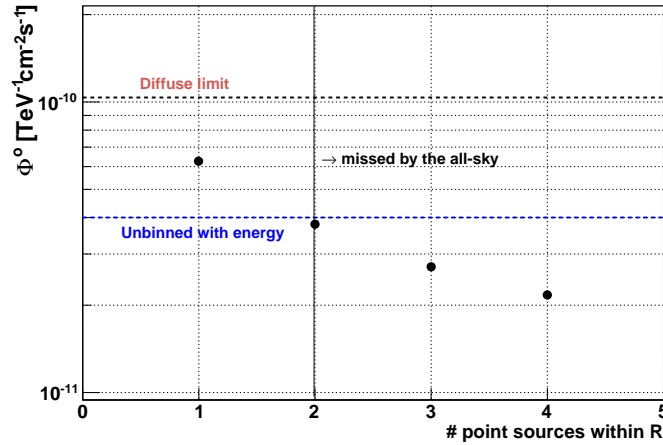


Figure 4.13: IC22+AMANDA minimum detectable flux per point source as function of the number of point sources within the region for an E^{-2} spectrum. Note that the emission does not need to be exclusively from point sources, the MPS can also take advantage of signals of different shapes.

Figures 4.13 and 4.14 show the IC22+AMANDA discovery potential per point source as function of the number of point source within the region. The discovery potential is shown for two simulated source spectra a) an E^{-2} , no energy cutoff and b) a Crab-like spectra: $E^{-2.4}$ and cutoff at 7 TeV, obtained from the gamma-ray spectrum assuming pp interactions (see section 1.2.2). For an E^{-2} spectrum, the plot in Fig. 4.13 shows the discovery potential of the energy-weighted unbinned analysis for single point-sources from (5). The IC22 point source analysis requires a flux of $4 \times 10^{-11} \text{TeV}^{-1} \text{cm}^{-2} \text{s}^{-1}$ from a single point source in order to reach 5σ for a E^{-2} spectra with no cutoff below 1 PeV. The obtained results for IC22+AMANDA indicate that MPS can not improve the current analysis in the case a single point source is present in the region. Improvement with respect to the standard searches starts for more than one point source in the region. In these cases, the required source strength is less than standard point source searches, and they would have been missed by the all-sky analyses. Note also that the minimum required flux from a point source can be lowered by the presence of diffuse events inside the region, which

⁶With larger event densities MPS shows an improvement with respect to a single-point binned analysis also for diffuse emission since in this case even diffuse events are able to form pairs.

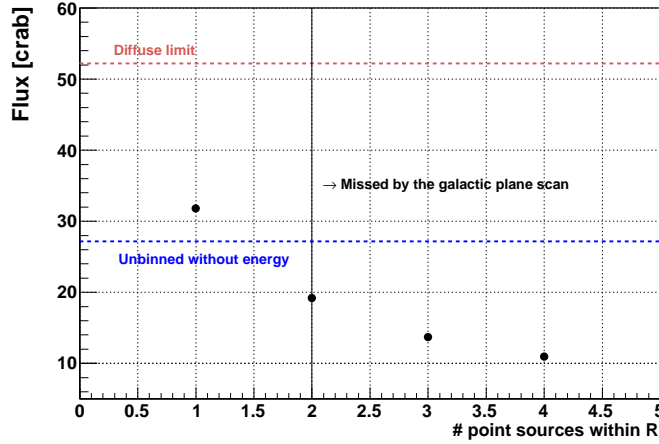


Figure 4.14: *IC22+AMANDA* minimum detectable flux per point source as function of the number of point sources within the region for a Crab-like spectrum (obtained from the gamma-ray spectrum assuming *pp* interactions).

may contribute to the formation of close pairs and therefore, to the increase of the overall emission.

With the coarse angular resolution of IC22+AMANDA, already with two point sources the emission is highly spread across the region. With more than four point sources in the region, signal events appear almost as diffuse, and the performance of MPS approaches that of a binned search. The limit shown in the plot at $1.2 \times 10^{-10} \text{TeV}^{-1} \text{cm}^{-2} \text{s}^{-1}$ corresponds to this diffuse limit, where the significance of MPS equals the significance of a binned analysis.

For sources with softer spectrum and/or energy cutoff below 1 PeV in neutrinos, the best sensitivity is achieved in the analysis presented in this work (see chapter 3). The minimum detectable flux of Fig. 4.14 is therefore compared with the one from the point source analysis with IC22+AMANDA presented in chapter 3, for which an unbinned method without energy term was used. With more than two point sources in the region, the analysis with MPS increases significantly the chances of discovery, reducing the minimum required source strength almost a factor of 2 with three point sources inside the region. The diffuse limit, where MPS performs as a binned search is shown in the plot at 57Crab^7 . This result indicates an improvement in the minimum detectable signal of $\sim 26\%$ - 59% (depending on the event pattern inside the region) with respect to single point source searches. With respect to an integrated binned search over the whole region, the less clustered case shown here (4 point sources in Fig. 4.14) still represents an improvement of $\sim 15\%$.

⁷Crab unit = $3.01 \times 10^{-7} E^{-2.4} \exp(-E/7 \text{TeV}) \text{GeV}^{-1} \text{cm}^{-2} \text{s}^{-1}$

Chapter 5

Results and Conclusions

This chapter presents the results of the analysis of IC22+AMANDA data in the search for neutrinos from our galaxy with energies in the range $100 \text{ GeV} < E < 3 \text{ PeV}$. The highest excess is found in the Cygnus region using the MPS method, with a p-value of 1%. This result is compatible with a background fluctuation at the level of 2.3σ , and no evidence of astrophysical neutrinos can be claimed.

The next sections detail the results of the two searches carried out in this thesis:

- The galactic plane scan searching for single point sources.
- The Cygnus region with MPS.

This chapter also contains a discussion about the future of galactic neutrino astronomy in the frame of the IceCube detector. Particular emphasis is given to the Cygnus region due to its relevance in this topic.

5.1 Galactic Plane Scan

The IC22+AMANDA galactic plane scan is a survey of the Galactic Plane searching for neutrino point-like sources covering the range in longitude accessible from the northern sky, $31.5^\circ < l < 214.5^\circ$, and latitude between $-3^\circ < b < 3^\circ$. The sky positions of this search are set by a grid of $0.25^\circ \times 0.25^\circ$, much smaller than the IC22+AMANDA angular resolution. The analysis of the observed event pattern is performed by making use of the unbinned likelihood method (7) as explained in section 3.4.1

5.1.1 Results and discussion

The results of the galactic plane scan consist in a p-value at each of the nodes of the grid. Figure 5.1 shows the map of the Galactic Plane obtained in this analysis.

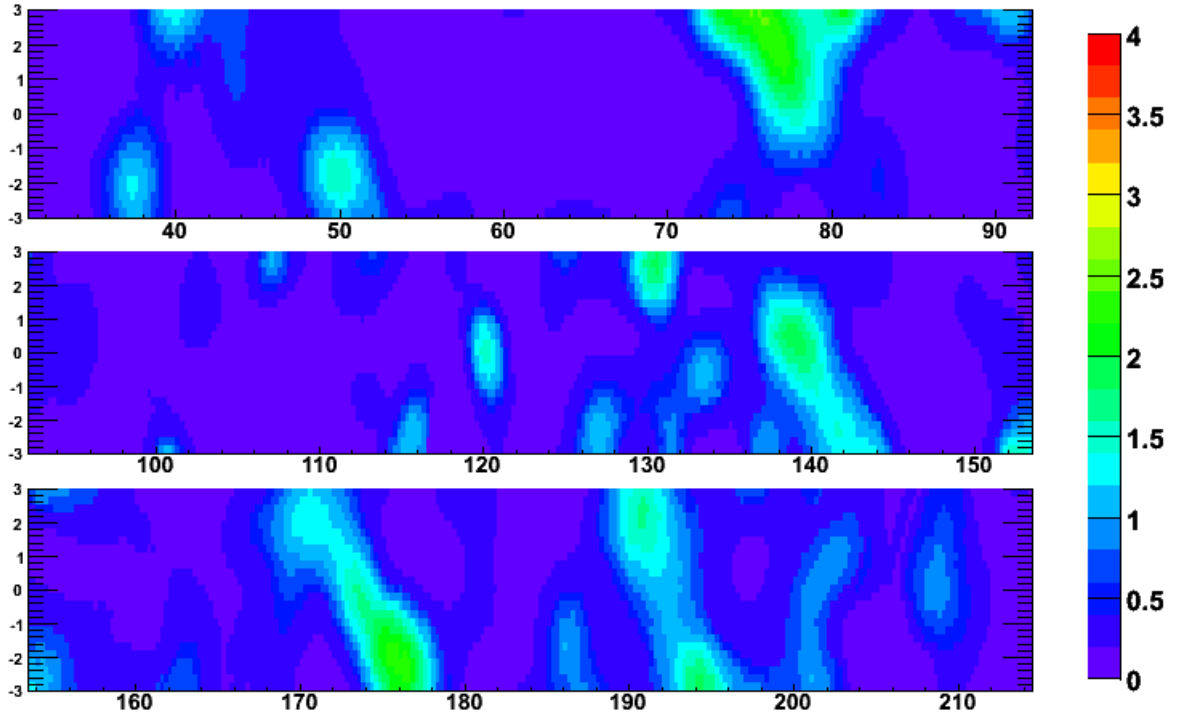


Figure 5.1: *Survey of the galactic plane in the energy range $100 \text{ GeV} < E < 3 \text{ PeV}$. No significant excess is observed, all the excesses found are compatible with random fluctuations of the background. The color scale represents significance in units of standard deviation. Y-axis represents galactic latitude and X-axis represents galactic longitude.*

The highest excess is located in the Cygnus region at $l = 75.87^\circ$, $b = 2.67^\circ$ (galactic coordinates), with a p-value of 0.0037. In 95% of scrambled datasets a greater or equal excess appears at some location in the scanned area. Therefore, the post-trial p-value associated to the highest excess observed is 0.95. No neutrino source has been found; all the excesses are compatible with random fluctuations of the background.

The surveyed region is shown in 5.2 over the CO map of the Galaxy from (26).

5.2 The Cygnus Region in IC22+AMANDA

The analysis of the Cygnus region with data from IC22+AMANDA searches for extraterrestrial neutrinos from a region of $11^\circ \times 7^\circ$ covering the range in galactic coordinates $72^\circ < l < 83^\circ$, $-3^\circ < b < 4^\circ$. The exact limits of the region were selected previously to the unblinding of the data from the galactic plane scan, in order to avoid possible bias. The search makes use of the MPS method (see chapter 4) in order to study the neutrino event

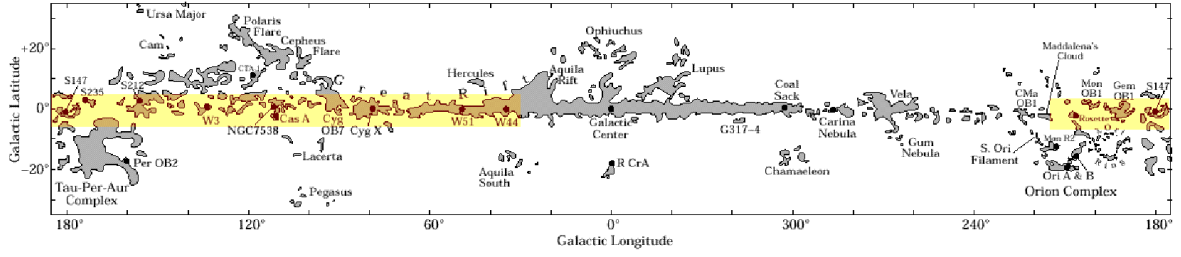


Figure 5.2: *CO map from the galactic disk (26). The surveyed area falls within the yellow-filled area.*

pattern observed by IC22+AMANDA in the region under examination.

5.2.1 Results

The deviations in the observed event pattern inside the Cygnus region with respect to the expected distribution of background events in IC22+AMANDA are quantified in terms of the angular scale of observation using a clustering function, $\Phi(\Theta)$, introduced in section 4.2.

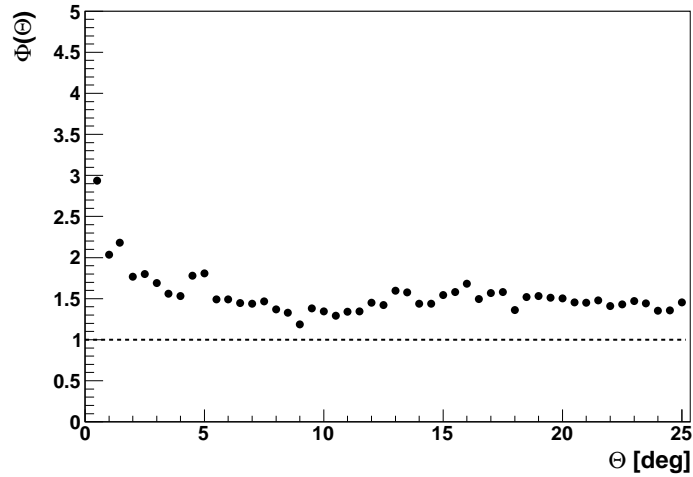


Figure 5.3: *Clustering function measured in the Cygnus region with IC22+AMANDA. The data shows an excess with respect to the average random distribution of events (located at 1) at all angular distances. The significance of the result is computed with the value of $\Phi(\Theta = 2^\circ)$, yielding 2.3σ .*

The measured clustering function in the Cygnus region with IC22+AMANDA is repre-

sented in Fig. 5.3. The data shows an excess over all angular distances. At distances larger than the typical size of the region ($\Theta > 15^\circ$ in order to avoid edge effects), the excess represents clustering of events within the Cygnus region, since all the events within the region contribute globally to the formation of pairs at these scales. Distances smaller than the typical size of the region ($\Theta < 7^\circ$) contain information about the excess of events inside the region as well as information about their spatial distribution, in particular about the small-scale clustering of events. The value of the clustering function at small Θ , representative of the excess in the number of close pairs of events, is therefore more sensitive to a possible neutrino signal. The significance of the observations is calculated from the measured value of the clustering function at $\Theta = 2^\circ$). This value was chosen before unblinding of the data, in order to speed up the calculations and to avoid the "inter-bin" trial factors. The number of pairs of events separated by less than 2° is 146, over a expected background of 75. 1% of randomly scrambled data sets have a greater or equal number of pairs within this separation; thus the observed result is compatible with a background fluctuation at the level of 2.3σ . A total of 40 events are observed in the region, compared to the 27 expected from the background (see Fig. 5.4).

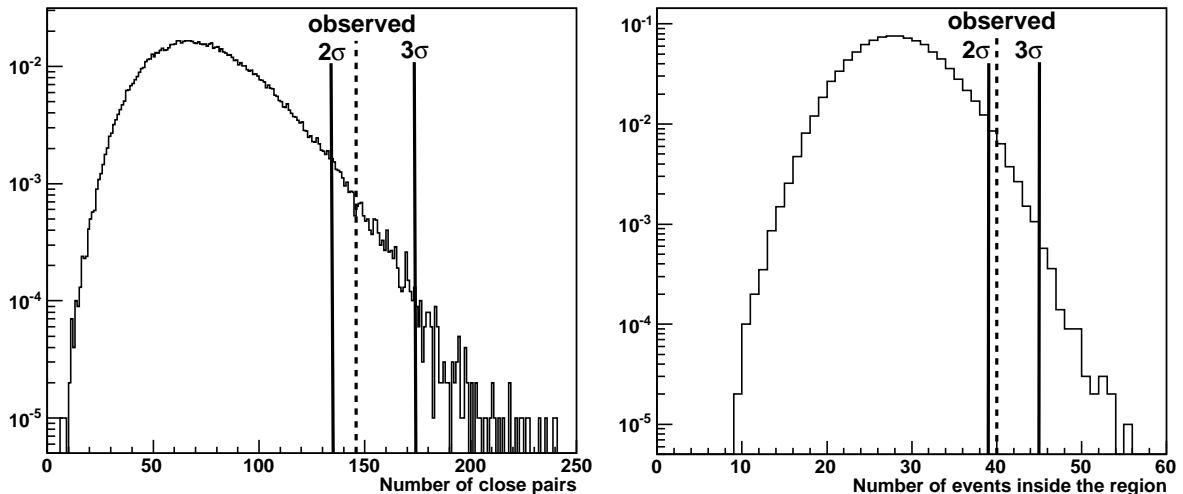


Figure 5.4: *Random fluctuations of the number of close pairs (left) and the number of events inside the region (right). The distributions have been obtained with 10^5 realizations of the MPS over scrambled skymaps from IC22+AMANDA. The observed value is marked with a dashed line in the plots.*

The resulting 2.3σ excess over background expectation is not significant in order to reject the null hypothesis, but it is enough to warrant further scrutiny. In order to study whether the observed excess in the number of close pairs is due to a positive fluctuation in the number of events in the region, or due to a fluctuation in the inter-event distances which characterizes the spatial distribution of background events, I show in Fig. 5.5

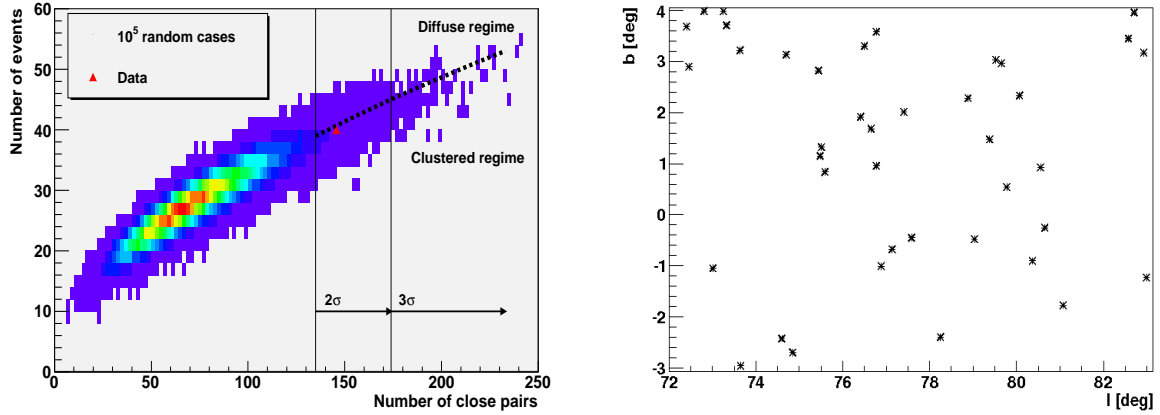


Figure 5.5: **Left** : Two dimensional distribution representing the random fluctuations in the number of close pairs and in the number of events inside the region. The dashed line represents points of equal significance in the two distributions and separates the two possible regimes in the spatial distribution of events that can be studied with this analysis. The measured value is represented as a red dot and it is consistent with a positive fluctuation of the background giving rise to the observed number of close pairs. **Right** : IC22+AMANDA events in the region within Cygnus studied in this analysis.

the two-dimensional histogram constructed with the distributions of Fig. 5.4. The y-axis represents the fluctuations in the number of background events in the region, while the x-axis represents the fluctuations in the number of close pairs. The observed value with IC22+AMANDA is represented as a red triangle in the plot. The black line represents the correlation between the number of events and the number of close pairs that would arise if the events are distributed randomly in the region. This correlation is drawn above 2σ from the average of the distributions. Above 3σ , measurements lying on this line would indicate evidence of an astrophysical signal inside the region which tends to be diffuse. Measurements lying below this line would indicate evidence of astrophysical events showing some clustering at the scales considered. Measurements above the line would indicate that the events are more dispersed than in a random distribution, circumstance that is hard to find in the case at hand. The observed excess in the number of close pairs falls very close to the line associated to events randomly distributed inside the region, and it is interpreted as the result of a positive fluctuation in the number of events in the Cygnus region, no significant spatial structure of events at the angular scales considered is seen. The measured point lies below the regime where the signal hypothesis can be accepted and therefore no evidence of astrophysical neutrinos can be claimed.

5.2.2 Neutrino upper limits

The power of the MPS relies on the angular distribution of events in order to take advantage of the possible clustered structure of the event pattern caused by extraterrestrial events. As discussed in chapter 1, the matter distribution is strongly clustered on scales of star clusters and associations. High energy protons can interact close to their sources of origin resulting in the appearance of clustered neutrino events. They can also escape and diffuse into the medium until they interact. In the latter case, the resulting neutrino events are not associated with any particular cluster and can be considered as diffuse events. The sensitivity of MPS ranges between a maximum clustered case (all the events come from a single point source or a single cluster of point sources) and a pure diffuse case. The most likely situation is probably an intermediate case with some clustered plus diffuse emission¹. However, our current understanding of the neutrino emission in the region is not sufficient to determine which is the real scenario. The TeV sources plus diffuse emission seen by the Milagro collaboration (125), although very bright in gamma-rays, are still too faint for IC22+AMANDA, and no constraints on the hadronic or leptonic nature of these different types of emission can be given at this stage.

In order to give an upper limit which takes into account all the possible scenarios for the distribution of signal events, this work gives the upper limit corresponding to the least sensitive case: a pure diffuse case. This has been constructed by producing random positions in the Cygnus region and then injecting a single event per position according to the PSF of IC22+AMANDA, in order to take into account the uncertainty in the event reconstruction.

Fig. 5.6 shows the flux upper limit at 12 TeV as function of the cutoff in the energy spectrum assuming that the energy distribution of the neutrinos emitted in the Cygnus region follows $\frac{dN_\nu}{dE} \propto E^{-\alpha} \exp(\frac{-E}{E_c})$. A spectral index $\alpha = -2$ has been considered in the computation of the upper limits. The neutrino flux obtained assuming that all the TeV flux measured by Milagro in the region considered (125) is of hadronic origin is drawn for comparison. Note that the upper limit is not very restrictive due to the fact that the region fluctuated positively. There is almost no dependency with the energy cutoff of the spectrum, since the reported upper limits correspond to a maximum flux of diffuse neutrinos within the region, and in this case the exact shape of the PSF used to inject the events is not relevant. The physical result of this analysis consists therefore in the most restrictive neutrino upper limit from the Cygnus region of the Galaxy.

¹This interpretation is supported by gamma-ray observations in the Cygnus region

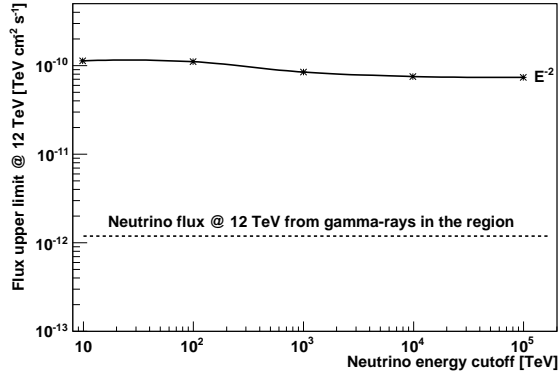


Figure 5.6: *Flux upper limit at 12 TeV obtained with MPS assuming that all the signal events from the Cygnus region is distributed as diffuse. The flux is plotted as function of the energy cutoff in the neutrino spectrum, which is assumed to follow E^{-2} . The neutrino flux at 12 TeV from the Milagro measurements in the region assuming that all the emission comes from pp interactions is shown for comparison.*

5.3 Summary and conclusions

The main topic of this thesis has been the search for potential sources of high-energy neutrinos in the Galaxy. To that end, I predicted the neutrino spectra of relevant galactic objects in order to compare with the IceCube expectations, presented an analysis scheme which optimized the analysis of the IceCube neutrino telescope for detection of neutrino emission in the energy range above 100 GeV, designed a method which studies the neutrino event pattern in extended regions, and applied it to the search of neutrinos from the Cygnus star forming region of the Galaxy.

In chapter 1 I have introduced the sources of high energy emission in our Galaxy, revisiting the predictions of neutrino emission from a number of different scenarios. I investigated the clustering of potential neutrino sources in young, very massive star clusters, and I proposed a strategy of observation which would take advantage of this clustering in order to improve the discovery potential.

The fundamentals of the IceCube detector, its components, data acquisition, and low-level data analysis processing, including the basic concepts about event reconstructions have been addressed in chapter 2.

In chapter 3 I presented the analysis of the data sample obtained with the IC22+AMANDA combined detector during the 2007-2008 season. By applying a series of optimal cuts based on the parameters of the reconstructed event track, I got from the raw sample of events to the neutrino level. The data was divided into two data streams, a combined stream,

representative of lower energetic events, and an IceCube only stream. The use of the additional information from the AMANDA detector in the reconstruction of combined events, allowed to keep many low energy events up to the final level, whereas those events would have been rejected in the IceCube only analysis. The obtained sample represents the largest neutrino sample collected by the IceCube detector in its 22 strings configuration. Then I used the final sample of neutrino events to perform an analysis of the galactic plane by defining a grid of coordinates that I used as the centroids for an unbinned search for point-sources. The IC22+AMANDA analysis reached the best sensitivity to point sources with a spectra steeper than E^{-2} and/or an energy cutoff below 1 PeV. The low-energy-optimized approach followed in this analysis has been the design driver of the DeepCore project.

The strategy of observation proposed in chapter 1 takes form in chapter 4, where I developed an analysis which is able to detect signals of various types in extended regions, the Multi Point Source analysis. The MPS method is a 2-point analysis based on the formalism of the 2-point correlation function which considers every event within the region under study as an individual point source. It takes advantage of the clustering of events inside the region to improve the discovery potential of the analysis with respect to methods aimed to the detection of individual point sources such as the binned or unbinned analysis. With the high statistics datasets expected in one year of operation of the IceCube detector, the MPS method can cover the scenarios presented in chapter 1, ranging its scale of observation from the smallest scales corresponding to the most compact clusters, to agglomeration of sources at scales of several degrees. In particular, for the IC22+AMANDA analysis, I proved that the MPS can reduce the minimum detectable flux per point source a factor $\sim 26\%$ - 59% , depending on the number of sources inside the region and on their morphology.

In chapter 5 I present the results of the analysis of galactic sources with IceCube22+AMANDA. The MPS has been applied to the Cygnus region, one of the most promising regions on the sky from the point of view of the neutrino astronomy. The result of the study of the event pattern in this region yields a significance of 2.3σ .

Future analysis with the IceCube detector will be able to confirm or refute the existence of high energy neutrino sources in the Cygnus region. The enhanced detection capabilities at low energies with the combined IceCube 80 strings plus DeepCore will open a wide range of opportunities for the future of galactic neutrino astronomy.

Acknowledgements

I would like to thank to all those people who contributed to this thesis in some way.

First of all, I would like to thank Elisa Resconi, my thesis supervisor, for giving me the opportunity to do this PhD thesis; but also for all the time she spent on thinking about me and my thesis at the same time she gave me all the freedom to develop my interests and my ideas, for her help in both scientific and non-scientific matters, for always encourage me to express myself, for listening, and because she always understands.

Andreas Gross, the postdoc of our group when I started my PhD, deserves big acknowledgement. He has not only provided valuable input to my work, explained me thousands of things about IceCube and data analysis, replied to each of my emails even when he was far away, but also took care of the analysis very nicely while I was on leave and also afterwards, working together in the scripts at the same time we tried to entertain little Silvia.

I would like to thank Olaf Schulz for being such a nice group partner since the beginning, and because he has been always willing to help in all sorts of matters.

Cecile Portello-Roucelle, Markus Voge, Sirin Odrowski and Claudine Colnard helped me at some point during this thesis. I would like to thank to all of them for the nice atmosphere in the office and in the group.

I want to thank also to all those people in IceCube who gave me fruitful comments about my work. Aday Robaina and Eric Bell also contributed to this thesis by giving me numerous suggestions on particular matters.

From the personal point of view, I would like to thank my mother, Lydia, for being always there, for her support, and because without her help I could not have done it on time. I want to thank also to Virginia and Jose, for being always the same no matter what happens, and because they have been always there when I needed them.

My husband, Aday Robaina Rapisarda, played an important role in my thesis, and I would like to give particular acknowledgment to him for the multiple and nice discussions about many physics topics that somehow contributed to the development of my work, and because we complement each other in such a wonderful way, that we have been able to enjoy our little family at the same time we both finished our thesis.

To my daughter, Silvia, because she always has a smile that makes all the tiredness go away. For teaching me to lie down quietly in the pleasant slices of life and get strength from them.

Bibliography

- [1] Sekido, Y. & Elliot, H., 1985, *Early history of cosmic ray studies*, Dordrecht, D. Reidel Publishing Co.
- [2] Linsley, J. 1963, *Physical Review Letters*, 10, 146
- [3] Nagano, M. 1998, *Workshop on Observing Giant Cosmic Ray Air Showers From $> 10^{20}$ eV Particles From Space*, 433, 76
- [4] Abbasi, R., et al. 2009, *Phys. Rev. D*, 79, 102005
- [5] Abbasi, R., et al. 2009, *ApJ*, 701, L47
- [6] Abbasi, R., et al. 2009, *Phys. Rev. D*, 79, 062001
- [7] Braun, J., Dumm, J., de Palma, F., Finley, C., Karle, A., & Montaruli, T. 2008, *Astroparticle Physics*, 29, 299
- [8] Aharonian, F., et al. 2007, *A&A*, 464, 235
- [9] Aharonian, F., et al. 2006, *A&A*, 457, 899
- [10] Albert, J., et al. 2007, *A&A*, 474, 937
- [11] Weekes, T. C., & the VERITAS Collaboration 2010, arXiv:1001.5305
- [12] MAGIC Collaboration 2008, *Nuclear Physics B Proceedings Supplements*, 175, 395
- [13] Hinton, J. A. 2004, *New Astronomy Review*, 48, 331

-
- [14] MILAGRO Collaboration 2006, Nuclear Physics B Proceedings Supplements, 151, 101
- [15] Aharonian, F., et al. 2006, ApJ, 636, 777
- [16] Hoppe, S. 2008, International Cosmic Ray Conference, 2, 579
- [17] Chaves, R. C. G., de Oña Wilhemi, E., & Hoppe, S. 2008, American Institute of Physics Conference Series, 1085, 219
- [18] Abdo, A. A., et al. 2007, ApJ, 664, L91
- [19] Abdo, A. A., et al. 2008, ApJ, 688, 1078
- [20] Longair, M. S., *High Energy Astrophysics*, Cambridge University Press (1994).
- [21] Blumenthal, G. R., & Gould, R. J. 1970, Reviews of Modern Physics, 42, 237
- [22] Jauch, J. M., & Rohrlich, F., 1995, *The Theory of Photons and Electrons*. Addison-Wesley Publ. Co., Inc., Reading, Mass.
- [23] Kelner, S. R., Aharonian, F. A., & Bugayov, V. V. 2006, Phys. Rev. D, 74, 034018
- [24] Kelner, S. R., & Aharonian, F. A. 2008, Phys. Rev. D, 78, 034013
- [25] Gould, R. J., & Schröder, G. P. 1967, Physical Review , 155, 1404
- [26] Dame, T. M., Hartmann, D., & Thaddeus, P. 2001, ApJ, 547, 792
- [27] Englmaier, P., Pohl, M., & Bissantz, N. 2008, arXiv:0812.3491
- [28] Strong, A. W., Moskalenko, I. V., Porter, T. A., Jóhannesson, G., Orlando, E., & Digel, S. W. 2009, arXiv:0907.0559
- [29] Taylor, A. M., Gabici, S., White, R. J., Casanova, S., & Aharonian, F. A. 2009, Nuclear Instruments and Methods in Physics Research A, 602, 113
- [30] Leitherer, C., et al. 1999, ApJS, 123, 3
- [31] Veilleux, S., Cecil, G., & Bland-Hawthorn, J. 2005, ARA&A, 43, 769
- [32] Messineo, M., Figer, D. F., Davies, B., Rich, R. M., Valenti, E., & Kudritzki, R. P. 2008, ApJ, 683, L155
- [33] Weidner, C., Kroupa, P., & Bonnell, I. A. D. 2010, MNRAS, 401, 275
- [34] Bergin, E. A., & Tafalla, M. 2007, ARA&A, 45, 339

- [35] Motte, F., Bontemps, S., Schilke, P., Schneider, N., Menten, K. M., & Brogière, D. 2007, *A&A*, 476, 1243
- [36] Ward-Thompson, D., Andre, P., & Motte, F. 1998, *Star Formation with the Infrared Space Observatory*, 132, 195
- [37] Lada, C. J. 2009, arXiv:0911.0779
- [38] Lada, C. J., & Lada, E. A. 2003, *ARA&A*, 41, 57
- [39] de Zeeuw, P. T., Hoogerwerf, R., de Bruijne, J. H. J., Brown, A. G. A., & Blaauw, A. 1999, *AJ*, 117, 354
- [40] Mirabel, I. F., Rodrigues, I., & Liu, Q. Z. 2004, *A&A*, 422, L29
- [41] Mauerhan, J., Van Dyk, S., & Morris, P. 2009, *American Astronomical Society Meeting Abstracts*, 214, #605.09
- [42] Tetzlaff, N., Neuhäuser, R., Hohle, M. M., & Maciejewski, G. 2010, *MNRAS*, 66
- [43] Mirabel, I. F., Mignani, R., Rodrigues, I., Combi, J. A., Rodríguez, L. F., & Guglielmetti, F. 2002, *A&A*, 395, 595
- [44] Higdon, J. C., Lingenfelter, R. E., & Ramaty, R. 1998, *ApJ*, 509, L33
- [45] Higdon, J. C., & Lingenfelter, R. E. 2005, *ApJ*, 628, 738
- [46] Klepach, E. G., Ptuskin, V. S., & Zirakashvili, V. N. 2000, *Astroparticle Physics*, 13, 161
- [47] Chen, W., & White, R. L. 1992, *NASA Conference Publication*, 3137, 417
- [48] Eichler, D., & Usov, V. 1993, *ApJ*, 402, 271
- [49] Bykov, A. M., & Fleishman, G. D. 1993, *A&A*, 280, L27
- [50] Webb, G. M., Axford, W. I., & Forman, M. A. 1985, *ApJ*, 298, 684
- [51] Reimer, A., Pohl, M., & Reimer, O. 2006, *ApJ*, 644, 1118
- [52] Engelmann, J. J., Ferrando, P., Soutoul, A., Goret, P., & Juliusson, E. 1990, *A&A*, 233, 96
- [53] Rauch, B. F., et al. 2009, *ApJ*, 697, 2083
- [54] Wiedenbeck, M. E., et al. 2007, *Space Science Reviews*, 130, 415
- [55] Binns, W. R., et al. 2005, *ApJ*, 634, 351

- [56] Ave, M., Boyle, P. J., Gahbauer, F., Höppner, C., Hörandel, J. R., Ichimura, M., Müller, D., & Romero-Wolf, A. 2008, *ApJ*, 678, 262
- [57] Horns, D., Hoffmann, A. I. D., Hoppe, S., & et al. 2008, International Cosmic Ray Conference, 2, 723
- [58] Aharonian, F., et al. 2007, *A&A*, 467, 1075
- [59] Ohm, S., et al. 2009, arXiv:0906.2637
- [60] Marcowith, A., Komin, N., Gallant, Y. A., & et al. 2008, International Cosmic Ray Conference, 2, 787
- [61] Benjamin, R. A., et al. 2003, *PASP*, 115, 953
- [62] Churchwell, E., et al. 2004, *ApJS*, 154, 322
- [63] Leisawitz, D., Bash, F. N., & Thaddeus, P. 1989, *ApJS*, 70, 731
- [64] Messineo, M., Davies, B., Ivanov, V. D., Figer, D. F., Schuller, F., Habing, H. J., Menten, K. M., & Petr-Gotzens, M. G. 2009, *ApJ*, 697, 701
- [65] de La Fuente Marcos, R., & de La Fuente Marcos, C. 2009, *New Astronomy*, 14, 180
- [66] Avedisova, V. S. 1996, *Astronomy Letters*, 22, 443
- [67] Avedisova, V. S. 2002, *VizieR Online Data Catalog*, 5112, 0
- [68] Chieffi, A., & Limongi, M. 2002, *New Astronomy Review*, 46, 459
- [69] Plüschke, S., et al. 2001, *Exploring the Gamma-Ray Universe*, 459, 55
- [70] Diehl, R. 2006, *New Astronomy Review*, 50, 534
- [71] Renaud, M., Vink, J., Decourchelle, A., Lebrun, F., Terrier, R., & Ballet, J. 2006, *New Astronomy Review*, 50, 540
- [72] Plüschke, S., et al. 2001, *Exploring the Gamma-Ray Universe*, 459, 87
- [73] Aharonian, F., et al. 2004, *ApJ*, 614, 897
- [74] Böttcher, M., & Dermer, C. D. 2005, *ApJ*, 634, L81
- [75] Dubus, G. 2006, *A&A*, 451, 9
- [76] Mirabel, I. F. 2006, *Science*, 312, 1759
- [77] Paredes, J. M., Marti, J., Ribó, M., & Massi, M. 2001, *Exploring the Gamma-Ray Universe*, 459, 433

-
- [78] Martí, J., Paredes, J. M., & Peracaula, M. 2000, *ApJ*, 545, 93
- [79] Mirabel, I. F., & Rodríguez, L. F. 1998, *Nature*, 392, 673
- [80] Gallo, E., Fender, R. P., & Pooley, G. G. 2003, *MNRAS*, 344, 60
- [81] Migliari, S., & Fender, R. P. 2006, *MNRAS*, 366, 79
- [82] Heinz, S., & Sunyaev, R. 2002, *A&A*, 390, 751
- [83] Bosch-Ramon, V. 2007, *Ap&SS*, 309, 321
- [84] Liu, Q. Z., van Paradijs, J., & van den Heuvel, E. P. J. 2006, *A&A*, 455, 1165
- [85] Winkler, C. 2008, *A Population Explosion: The Nature & Evolution of X-ray Binaries in Diverse Environments*, 1010, 272
- [86] Anchordoqui, L. A., Torres, D. F., McCauley, T. P., Romero, G. E., & Aharonian, F. A. 2003, *ApJ*, 589, 481
- [87] Dubus, G. 2006, *A&A*, 456, 801
- [88] Aharonian, F., et al. 2005, *A&A*, 442, 1
- [89] Aharonian, F., et al. 2006, *A&A*, 460, 743
- [90] Jogler, T., et al. 2008, *Journal of Physics Conference Series*, 120, 062019
- [91] Sierpowska-Bartosik, A., & Torres, D. F. 2009, *ApJ*, 693, 1462
- [92] Albert, J., et al. 2007, *ApJ*, 665, L51
- [93] Fermi LAT Collaboration, et al. 2009, *Science*, 326, 1512
- [94] Orellana, M., & Romero, G. E. 2007, *Ap&SS*, 309, 333
- [95] Romero, G. E., Torres, D. F., Kaufman Bernadó, M. M., & Mirabel, I. F. 2003, *A&A*, 410, L1
- [96] Chernyakova, M., Neronov, A., & Walter, R. 2006, *MNRAS*, 372, 1585
- [97] Bosch-Ramon, V., Romero, G. E., & Paredes, J. M. 2006, *A&A*, 447, 263
- [98] Jogler, T., et al. 2009, *arXiv:0907.0992*
- [99] Christiansen, H. R., Orellana, M., & Romero, G. E. 2006, *Phys. Rev. D*, 73, 063012
- [100] Bednarek, W. 2005, *ApJ*, 631, 466

-
- [101] Torres, D. F., Romero, G. E., & Mirabel, F. 2005, Chinese Journal of Astronomy and Astrophysics Supplement, 5, 183
- [102] Chernyakova, M., Neronov, A., & Ribordy, M. 2009, arXiv:0912.3821
- [103] Bednarek, W. 2006, MNRAS, 371, 1737
- [104] Grieder, P. K. F. 1995, Nuclear Physics B Proceedings Supplements, 43, 45
- [105] Barwick, S. W., & et al. 1991, International Cosmic Ray Conference, 4, 658
- [106] Wilkes, R. J. 1996, Particle Physics, Astrophysics and Cosmology, 301
- [107] AMANDA Collaboration 1997, International Cosmic Ray Conference, 7, 5
- [108] Belolaptikov, I. A., et al. 1994, Nuclear Physics B Proceedings Supplements, 35, 290
- [109] Thompson, L. F. 2001, Nuclear Physics B Proceedings Supplements, 91, 431
- [110] Particle Data Group, et al. 2008, Physics Letters B, 667, 1
- [111] Learned, J. G., & Pakvasa, S. 1995, Astroparticle Physics, 3, 267
- [112] Ackermann, M., et al. 2006, Journal of Geophysical Research (Atmospheres), 111, 13203
- [113] The Icecube Collaboration, et al. 2009, Nuclear Instruments and Methods in Physics Research A, 601, 294
- [114] Abbasi, R., et al. 2009, Physical Review Letters, 103, 221102
- [115] Ahrens, J., et al. 2004, Nuclear Instruments and Methods in Physics Research A, 524, 169
- [116] Grullon, S., Boersma, D. J., Hill, G., & et al. 2008, International Cosmic Ray Conference, 5, 1457
- [117] van Eijndhoven, N., Fadiran, O., & Japaridze, G. 2007, Astroparticle Physics, 28, 456
- [118] Lundberg, J., Mioćinović, P., Woschnagg, K., Burgess, T., Adams, J., Hundertmark, S., Desiati, P., & Niessen, P. 2007, Nuclear Instruments and Methods in Physics Research A, 581, 619
- [119] Neunhöffer, T. 2006, Astroparticle Physics, 25, 220

-
- [120] Heck, D., Knapp, J., Capdevielle, J. N., Schatz, G., & Thouw, T. 1998, CORSIKA: a Monte Carlo code to simulate extensive air showers., by Heck, D.; Knapp, J.; Capdevielle, J. N.; Schatz, G.; Thouw, T.. Forschungszentrum Karlsruhe GmbH, Karlsruhe (Germany)., Feb 1998, V + 90 p., TIB Hannover, D-30167 Hannover (Germany).,
- [121] J. Hörandel, APh, 19, 193 (2003).
- [122] Gazizov, A., & Kowalski, M. 2005, Computer Physics Communications, 172, 203
- [123] Chirkin, D., & Rhode, W. 2004, arXiv:hep-ph/0407075
- [124] Gross, A., Ha, C., Rott, C., & et al. 2008, International Cosmic Ray Conference, 3, 1253
- [125] Abdo, A. A., et al. 2007, ApJ, 658, L33
- [126] De Domenico, M., Scuderi, M., & Insolia, A. 2010, arXiv:1001.1666
- [127] J. Peebles, "*The Large Scale Structure of the Universe*", Princeton University Press (1980).
- [128] Maddox, S. J., Efstathiou, G., & Sutherland, W. J. 1996, MNRAS, 283, 1227
- [129] The High Resolution Fly's Eye (HIRES) Collaboration 2004, Nuclear Physics B Proceedings Supplements, 136, 46
- [130] Finley, C. B., & Westerhoff, S. 2004, Astroparticle Physics, 21, 359
- [131] Beacom, J. F., & Kistler, M. D. 2007, Phys. Rev. D, 75, 083001